Two Examples of Modeling Practices in Solar System Dynamics and Plasma Physics

by

Daniel D. Sega

M.St., University of Oxford, 2018

M.Sc., University of Colorado Boulder, 2020

A thesis submitted to the

Faculty of the Graduate School of the

University of Colorado in partial fulfillment

of the requirements for the degree of

Doctor of Philosophy

Department of Astrophysical and Planetary Sciences

2024

Committee Members:

Robert E. Ergun

Glen. R. Stewart

Heather Demarest

Ann-Marie Madigan

Zachory K. Berta-Thompson

Sega, Daniel D. (Ph.D., Astrophysical and Planetary Sciences)

Two Examples of Modeling Practices in Solar System Dynamics and Plasma Physics

Thesis directed by Prof. Robert E. Ergun and Dr. Glen. R. Stewart

Models are an essential part of the scientific practice. However, they often fail to be one-to-one representations of the physical system studied; they present idealizations and abstractions. By taking two models developed by me and collaborators as examples—bending waves in Saturn's rings and acceleration ions in the Earth's reconnecting magnetotail—I will argue that approximations and abstractions are not introduced in models for computational convenience alone but to highlight the explanatory relevant parts of the physical system in question.

Dedication

To the ones who know the road of trials overcame: my wife Karina and mother Maria Isabel.

Acknowledgements

At many moments in this journey I felt I had set myself too ambitious of a goal, if I was to achieve this goal by myself. Fortunately that was not the case, and I received much help along the way. The most candid help is the one one receives unexpectedly, from an unlikely and uninvolved party. That is the type of help and guidance I received from Robert Ergun and my friend Girish Duvvuri. Thank you Bob for showing your support when my PhD candidacy was at risk, when I thought I would be more useful working elsewhere, doing something else. Offering not kind words, but a concrete thesis path in Plasma Physics (when I didn't have any experience on the subject), kept me advancing towards for my academic goals. Thanks for your vote of confidence. Girish, you were surprisingly tolerant roommate during the PhD, but most importantly a teacher in its own right, and an intellectual guide in the most somber moments. Gracias.

Marcos Rodriguez, you are a terrific professor and thanks to you all the fundamental concepts of classical physics, everpresent in this thesis, were drilled into my brain; thanks to you I didn't just saw them as a dull step towards the more interesting and vanguardist topics in Physics. Almost all of my Philosophy teachers and professors left a mark, not only on my academic but on my personal life as well—as philosophers often do—and I appreciate their commitment to the examined life. I want to thank specifically Heather Demarest for allowing me to have those philosophic conversations I so missed when I changed to Astrophysics, and for coming to my aid and showing a surprising commitment to this project. I also want to thank my fried Caspar Jacobs for the fruitful and interesting conversations and comments.

Finally I thank my father for always reminding me of what I am capable of, and that anxiety and preoccupation are unnecessary to achieve the goal at hand. I know you would be proud, but not surprised, of what I have managed.

Contents

Chapter

Tables

Table

Figures

Figure

Chapter 1

Introduction

Scientists aim to describe the world as it is. They do this by constructing models that represent certain aspects of the world. If a model makes successful predictions, then it seems reasonable to assume that each part of that model corresponds to a real aspect of the world.

In this thesis, I will argue that this is not always the case. By using test cases of scientific models developed during my doctoral studies, I will show that scientific modeling does not only concern itself with one-to-one representations. There are many other things that the practice of science attempts to do, and these different applications of science condition the types of scientific models that are produced. Specifically, I will emphasize that, for the purpose of being explanatory, the accuracy of a model can impair—instead of enhance—the model's effectiveness. Hence, I will argue that models with certain distortions (idealizations or abstractions) are necessary for good scientific practice. As a result, distortions are there not only for computational convenience but also to highlight explanatorily relevant factors.

The study of representations in science aims to make salient the conditions that a model must satisfy in order to properly represent the target system. What is the nature of the relation that holds between the model and the target? What makes a good scientific representation? How mathematical equations, and models in general, manage to represent the real world will be analyzed from the perspective of a theory of representation in general. I hence start by asking how representations are achieved in the general case (scientific or otherwise).

We'll analyze an often-mentioned candidate for the key relation between the model and the real world: similarity or resemblance—representation is possible by virtue of two things being similar. With the

aid of van Fraassen's *Scientific Representation* we'll argue that the key feature of scientific representation is not similarity, but rather the relation that exists between the scientist doing the representing, and the model. Models are used by scientists to represent part of the world with a specific purpose in mind: maybe reproducing a set of data to some defined accuracy, making a prediction or providing an explanation, or allowing for technology building. We'll conclude that the ability to fulfill the purpose set by the scientist is the key to a good representation. Similarity can be relevant for fulfilling this purpose, but only in service of the purpose.

Then, we will explore the distinction between the explanatory and descriptive functions that scientific models may have, as suggested by Nancy Cartwright. We will then ask two questions about our models. Q.1: *What purpose does our model fulfill and how does it justify the distortions introduced?* and Q.2: *How do these models fulfill the explanatory or the descriptive functions of scientific modeling?* In this introduction (Chapter 1) I present the historical development of these questions in the philosophy of science literature. Then I will present the models in detail: a model of vertical waves in Saturn's A ring (Chapter 2) and a model of the motion of ions in the Earth's magnetotail (Chapter 3). Finally, we will conclude by answering the question we formulated in the first chapter (Chapter 4).

1.1 Representation and Scientific Representation.

Science provides us with representations that we use to study and predict the behavior of real systems. Representation is then, at a first attempt to describe it, a relation between at least two objects: the one that represents, and the one that is represented. I'll refer to the former as the medium, and the latter as the target. Models are, in our framework, a type of medium.

One way of looking at the models of science, and their relation to the targeted system, is to think of them as pictures (extended over time) of a part of the universe. Pictures (and representations more generally) are about something. This property of being about something is usually called intentionality, and we'll explore it to draw some conclusions about representation in general.

The intentional aspect of pictures comes from what Edmond Husserl called intentional content. That is when something is intended, it is always intended as being in such and such a way. The attributes that we

add or subtract from the object itself when partaking in the intentional act (the representation) constitute its intentional content. With intentionality then, also comes the possibility of *distorting* the object represented. Husserl writes:

> We must distinguish (...) between *the object as intended*, and the object (period) which is intended. In each act [representation] an object is presented as determined in this or that manner, [...and there may be further] objective properties to the same presented object, properties not in the scope of the intention in question (Husserl, 1913)

In other words, representation of something, an object, say, consists in that object being represented as being a certain way, which is distinct from the object actually having (or lacking) said properties. This as/of distinction, as van Fraassen calls it, becomes crucial to him when attempting to explain what makes a representation accurate and how a medium may fail to represent a target. Distortion and accuracy are often framed under the *possibility of misrepresentation*, which is a constraint on a representation theory to admit bad representations as representations nevertheless.

At first glance, it may occur to us that the relation between the medium and object represented is one of *similarity*: for a medium to represent its target it ought to be similar in some respects. A question arises: in which respects and to what degrees is the similarity required for the medium to count as a representation of the target? Do dissimilarities always make for misrepresentations? Many authors have argued that at least for the case of scientific representation this doesn't seem right: distortions are, in many cases, as important as similarities when best representing a system.

For the models examined in this dissertation, important distortions are present. On one hand, we have our model of self-gravity wakes, which are temporary clumps that, in numerical N-body simulations, come apart and reform in about one orbit around Saturn (Karjalainen & Salo, 2004). However, we model them as rigid bodies orbiting Saturn's rings and reacting to the different torques by changing their orientation with respect to the radial vector. These aggregates are not, strictly speaking, rigid, and yet the model manages to explain the thus-far-unexplained observations it sets to explain. On the other hand, we build the model of the plasma in the reconnection region, which is taken to not be self-consistent, by which we mean that it does not strictly obey Ampere's Law (one of Maxwell's Equations). This is a big distortion between the

medium and the target! Nevertheless, both models do something right, and we'll argue that their ability to properly represent the target comes, not in spite of these distortions, but because of them. This will be in part due to the intended use of a representation. Van Franssen argues:

> If we just focus on resemblance in some respect as the core notion in representation, then it is at best puzzling that distortion might be needed for effective representation. But if the resemblance is just a means to an end there is no puzzle. The sculptor wants the object he makes to have a certain use, and he chooses the way in which the proportions of the object are related to those of the original—the way in which they are like and the ways they are unlike—so as to make that use possible. (Van Fraassen, 2008)

To evaluate the effectiveness (or goodness) of representation of our models we should focus on what we are attempting to accomplish with them. One of the purposes of our models is, of course, to reproduce the phenomena, that is, the value of measurements of physical quantities. Specifically, we want to reproduce the data measured by Cassini for the Rings model, and the data measured by the Magnetic Multiscale mission (MMS) for the case of the Earth's magnetotail plasma model. In more philosophical terms, the models aim for empirical adequacy. That much they manage to attain. If we want an additional criterion for a representation to be good that goes beyond just reproducing the data, we must think of what other purposes our models may have.

A possible answer is that, beyond fitting the data, the models also aim to explain the data. What precisely counts as an explanation is a philosophical debate of its own, and there are many ways in which an explanation can be said to explain. For our argument, however, and for our concrete cases of the two models to be studied, we can rest on the intuitive notion that an explanation involves showing how the phenomenon in question "comes about." That is, showing how an initial state of a model—which has already been explained and lies in agreement with the known properties of the target— evolves into a state that reproduces the measured quantities that are to be explained. The view that any scientific explanation ultimately amounts to telling this causal story has been dubbed by philosophers "the causal-mechanistic account of explanation." (Salmon, 1984; Peters & Babee, 2020). Giving this causal story is something our specific models are attempting to do, in the hopes of explaining the data, which is the purpose of our models.

With the purpose of explanation in mind, we can now ask what the relevant similarities between the

target and the model are given the purpose of our representation. The best model for the job may actually be one that includes some distortions. Certainly, an attempt to represent every single detail of the targets in question may be counterproductive when considering what the purpose of our representation is. Jorge Luis Borges, in his micro story *Del Rigor en la Ciencia* (On The Rigors of Science), exemplifies the importance of distortion. The story is short enough to be cited in its entirety (translation in English by the author):

> In that Empire, the art of Cartography managed such Perfection that the map of a single province would occupy an entire City, and the map of the Empire, an entire Province. With time, these Excessive Maps did not satisfy and the College of Cartographers built a Map of the Empire that had the same size of the Empire coincided with it point by point.
>
> Lesser Addicts of the Study of Cartography, the Next Generations understood that said detailed Map was Useless and not without Impiety they delivered it to the Relentlessness of the Sun and the Winters. In the deserts to the West there are still shredded Ruins of the Map, inhabited by Animals, and by Beggars; in the whole Country no other relic of the Geographic Disciplines is left. (Borges, 2018)

This story warns us of the perils of neglecting the purpose of models while focusing on their accuracy. In an effort to eliminate all the distortions between a map and the region it represents, they made the map useless.

Are these maps misrepresentations? If accuracy were the only important characteristic they are the best representations possible since they even forgo the usual distortions of scaling and 2D-projecting. They are getting something right about the world, even if we cannot use them to navigate due to their unpractical size. Van Fraassen, on the other hand, would say these are misrepresentations since they don't have the relevant distortions for the purpose at hand, namely (presumably) navigation. When evaluating a representation, we are urged to consider the purpose of the representation in question; without this context, we cannot properly evaluate a model.

Borges' story highlights the importance of use in identifying which are the relevant similarities and distortions, and to what degrees the medium must be similar to the target in order to be useful. Our final goal, and van Fraassen's, is not to write a representation theory but to describe how scientific representation does its job, and van Fraassen, Borges, and I agree that detailed similarity doesn't necessarily make a scientific model better. Use, van Fraassen claims, is also what will ultimately determine what is being represented by

the medium, and as what. That is, the aboutness of the representation is not given by the medium itself but by the agent using the medium; this shouldn't surprise us since for something to be intentional, for it to be about something, requires an agent.

"There is no representation except in the sense that some things are used, made, or taken to represent something as thus and so" van Fraassen claims (*ibid.* 23). The word 'use' is now being employed in a broad sense; to account for how the agent A may use a medium M (to represent a target T as being F) vs. how the same agent may use the representation itself for purpose P. Here's an example used by van Fraassen (Van Fraassen, 2008):

Sculptures placed on high ground (say, on the altar of a temple of Athena) are distorted to compensate for the change in the proportion of the bodies caused by the perspective of the viewers. Because the statue will be placed on a pedestal, these distortions are relevant for the purpose of the representation. But at the same time, the sculpture is also 'using' the marble to make the sculpture. We may then say that the sculptor (A) is using a marble statue (M) to represent Athena (T) as being beautiful (F) on the high altar of a temple (P). The purpose doesn't only give us the relevance of the similarities, we can also use it to determine the style of the representation. This final distinction is important for scientific models.

I claim that the most salient and defining characteristic of scientific representation, as opposed to representation in general, is that it allows for an inference to be made about the behavior of the targeted system, from premises related to the model. That is, we can use the model to make predictions and formulate explanations. A question we can ask of our models is:

> Q.1: What purpose does our model fulfill and how does it justify the distortions introduced?

We will see in the conclusion that the answer will be:

> A.1: Our main objectives are first attempts at reproducing and explaining the phenomena.

While I have stated that the models analyzed in this work have distortions, I still haven't argued why these distortions help—rather than detract from—the model's ability to represent. One easy answer for this is that of computational convenience: we use approximations to make the models tractable either analytically

or computationally. But computability aside, are there other reasons to use distortions, idealizations, or abstractions? How can distortions be a good thing in science? Don't we want to represent the system just as it is, as precisely as we can? The example of the Athena statue may be good in showing how distortions can be positive features for representation in general, but we still need to show it applies to scientific representation.

The answer is ultimately related to the explanatory role that models have in actual scientific practice. As van Frasseen reminds us, the distortions can also serve to highlight the model's intended purpose. In the case of science, we will see in the next section that as in Borges' story, when one emphasizes the usefulness of the model in hand, more precise models tend to be worse than the approximate ones for fulfilling the model's purpose.

1.2 Descriptive and Explanatory Models

The claim that scientists must aim for their models to be as precise as they can conveniently make them has been disputed by philosophers writing on the use of scientific models. A central purpose of our models, necessary to evaluate their goodness of representation, is that of explaining phenomena. Uncovering facts about the target and explaining certain phenomena that obtain in the target are two different tasks that a scientist must do. The distinction between each task is highlighted in Cartwright's seminal paper: "The Truth Doesn't Explain Much". She starts her essay as follows:

> Scientific theories must tell us both what is true in nature, and how we are to explain it. I shall argue these are entirely different functions and must be kept distinct. Usually, the two are conflated. The second is commonly seen as a by-product of the first. Scientific theories are thought to explain by dint of the description they give to reality. Once the job of describing is done, science can shut down. (...) That is a mistake. (Cartwright, 1980)

She then argues, by using real examples from published work, that the act of explaining (1) involves distortions from the theoretically best possible description of the target and (2) highlights the "explanatory relevant" parts of the description. These make explanatory models, according to her, full of strictly false statements. Nevertheless, they are useful for the purpose of explaining. Therefore, for the case of explanation, more strictly speaking "incorrect" models do a better job than the theoretical perfect description of the

target. Specifically, she argues that highly idealized models, which may even introduce idealization that is, strictly speaking, known to be false, is more explanatory than the de-idealized version.

This argument resonates strongly with the previously discussed idea that distortions may make a representation better, depending on the purpose of the representation in question. In the case of Borges' story, the use-cases of maps made the perfectly descriptive map useless. There are many uses for a model to do, not just description. We want it to explain, as Cartwright argues, and we want to be able to compute with it and make reliable predictions easily.

We emphasized earlier that the purpose of a model is crucial for evaluating how well it represents the target. However, if Cartwright is right, scientific models can perform two functions that may pull in opposite directions. This tension can be illustrated in modern scientific discussions around the topic of N-body simulations:

In theory, in a classical complex system of particles, one could write every particle and the $1/r^2$ force this particle experiences, together with the field this particle generates. Computational precision limits and non-linear dynamics aside, this modeling technique should be able to solve every classical problem regarding the motion of particles or collection of particles in space, assuming we have enough computational power. Nevertheless, even if these models reproduce the phenomena we want to explain, they do not give us any insight into the phenomena, beyond the reconfirmation that the phenomena in question are in accord with the fundamental particle-per-particle laws of dynamics. As models get more complex, detailed similarity to the target phenomena comes at the cost of providing insight into what's actually happening.

Consider the scientific questions: Why is there the Cassini gap in the rings of Saturn? One may answer: because the particles in the solar system obey Newton's laws (or more precisely, they obey Quantum Mechanics and General Relativity). That is technically true, but that such macroscopically emerging phenomenon as gaps in rings is consistent with the fundamental laws of our current best theories is something we already know to be true. On the other hand, if a model with many approximations still manages to reproduce the gap, much insight can be gained.

Scientific authors that appeal to overly complex simulations tend to still give separate explanations about what the model "is actually doing," even after laying out a complete description of the simulation in

question. What is usually done, and we will see it is done in the plasma model presented in this work, is that certain parameters of the model are set to zero, or certain effects in the simulation are "turned off," to establish by means of counterfactual dependence[1] , a causal relationship between the emerging features in the simulation. Idealizing N-body computer simulations can therefore be used to highlight the explanatory relevant aspects of these simulations.

This practice is commonplace nowadays. In Chapter 2 we will offer a simplified model that captures the results of N-body numerical simulations done by Michikoshi et al. (2015). Likewise, in Chapter 3 we will see how we will remove parameters from our plasma model in order to expose the causal structure of the reconnection region plasma. The concept of Idealization is traditionally used in philosophy to mean a real-world-to-model distortion. But more recently, like in our case, we have been seeing a model-to-model distortion, where a more simplified model is derived based on another model.

This process of simplifying a model by systematically removing certain parameters goes opposite to the modeling practice of De-idealization. Morrison and Morgan describe De-idealization as carefully "adding back" effects that at first were idealized away until the desired phenomena can be reproduced. For example, bringing back higher-order terms that were originally dropped from a Taylor series expansion in a De-idealization in this sense. By contrast, I will use the term re-idealization for the methodic "taking away" of parameters from an all-encompassing computer model to allow for an insightful conclusion.

The practice of re-idealizing shows that analytic or pseudo-analytic treatments, while often even more distorted than their computational counterparts, can provide more insight at the cost of losing similarity with the target. This notion of 'insight' lies very closely with the philosophic notion of 'understanding' and both are tied to what Cartwright calls the 'explanatory function' of models in science.

A conclusion we can draw from Cartwright's argument is that, given that the two functions of science can at odds with one another, we need to produce at least two models for each target. One that highlights the explanatory relevant part, and another that is merely descriptive. The practice of removing parameters

[1] A counterfactual is a supposition that entertains things that are counter to the facts; that is, situations that don't actually obtain. Imagine evolving the Solar System with all the right parameters for its planets and star, except we don't include Saturn. This model's target is no real system at all, it is a counterfactual. Modelers remove certain causal powers in their simulation, which are in fact there, to investigate how the behavior of the system depends on such causal powers. Many philosophers believe that counterfactuals are a key in analyzing and better understanding causation (Peters & Babee, 2020), some going as far as stating that counterfactual dependence is all that causation is, even arguing against the temporal asymmetry of causation. (Lewis, 1973).

from N-body simulation to reveal the explanatory relevant parameters in a model is in accord with this idea.

In scientific practice we often see approximations and idealizations introduced uniquely as tools of computational expediency. Their introductions are commonly framed around making problems solvable analytically, or making simulations run faster, while their representational role is obscured or deemphasized. For van Fraassen's notion of representation *simpliciter*, however, a distorted model *highlights* certain aspects of the model through the distortions. These highlights are necessary for a representation to be good (if the purpose is to explain), as they highlight the pieces of the model that are doing the explanatory work. In this sense, van Fraassen and Cartwright agree that the distortions and the highlights go together. The distortions aid in explaining the phenomena in question.

We want to contrast this positive view of distortions against the commonly held notion that distortions are there only for computational convenience—an unfortunate necessity stemming from the limited powers of our computers. However, the common practice of removing parameters to find the explanatory relevant entity in a complex model shows that regardless of the scientist's take on distortion (commonly believed to be a negative thing), the practice of distorting as highlighting is common. But this needs to be brought forth in the way the models are presented: distortions can, and should, also be used to highlight the relevant aspects of the target that provide explanatory insight. Therefore, distortions should not be thought of uniquely for computational convenience alone. The Saturn article in this paper exemplifies this practice.

Another question we will ask of our models is:

> Q.2: How do these models fulfill the explanatory or the descriptive functions of scientific modeling?

We will see in the conclusion that the answer will be:

> A.2: Both models aim to be more explanatory than descriptive, and they do so by providing a causal story of how the relevant phenomenon comes about.

Before fully presenting the models we will be evaluating as scientific representation, we will briefly introduce their subject of study, namely their targets, and describe the phenomena we are attempting to explain. The targets are the dynamically perturbed A Ring of Saturn and the ions in the turbulent reconnection region of Earth's magnetotail.

1.3 The A Ring of Saturn

Saturn has 7 main rings, all of them comprised primarily of icy particles ranging from millimeters to tens of meters, and classified by their observational properties. By order of their proximity to Saturn, these rings are D, C, B, A, F, G, and E (see Figure 1.1). The A ring sits in the middle of this list and lies at the outer edge of the large, luminous rings. It starts at 122000 km and ends at 137000 km from Saturn's center. The A-ring is dense and optically thicker than all rings but the B ring. A light source emitting normally to the ring will see that less than half of its emitted photons make it through the ring (the transmission of light is smaller than 50%). Its density, and moderate distance from Saturn's center, propitiates particles to clump temporarily into elongated structures called self-gravity wakes. There are clear observational signatures that suggest that self-gravity wakes are ubiquitous in the A ring. Self-gravity wakes have been modeled extensively via n-body simulations (Salo, 1992; Karjalainen & Salo, 2004; Michikoshi et al., 2015).

The radial position of the A-ring makes many of its orbital frequencies resonant with satellite orbital frequencies, and hence it is dynamically perturbed by satellites. One of their resonances occurs when the vertical motion of an inclined satellite (a satellite whose orbit significantly deviates from the equator of the planet) resonates with a ring particle at some distance r. This causes the material to be lifted vertically and, due to the gravity that the ring particles exert on each other, this perturbation propagates through the ring forming a bending wave (BW). The theory of bending waves has been developed for a ring of uniform density: the motion of self-gravity wakes within a waving ring is a complicated problem that has not been solved. We attempt a solution by treating self-gravity wakes as rigid and then compare our model to the data collected for the Mimas 5:3 bending wave. For our specific wave, Mimas is the perturbing satellite and the ratio of the ring to satellite orbital period is 5 to 3 (see Figure 1.2).

There is no unique source that contains all the bits and pieces of the theory of linear bending waves in a deductive fashion, so we present such an exposition in Appendix C for the reader interested in learning the theory rigorously. Likewise, we haven't published a standalone presentation of the rigid self-gravity wake model for the simpler case of the flat ring (no bending wave), so we include this presentation in Appendix D. Our model will attempt to combine both models to solve the problem of bending waves in a clumpy medium

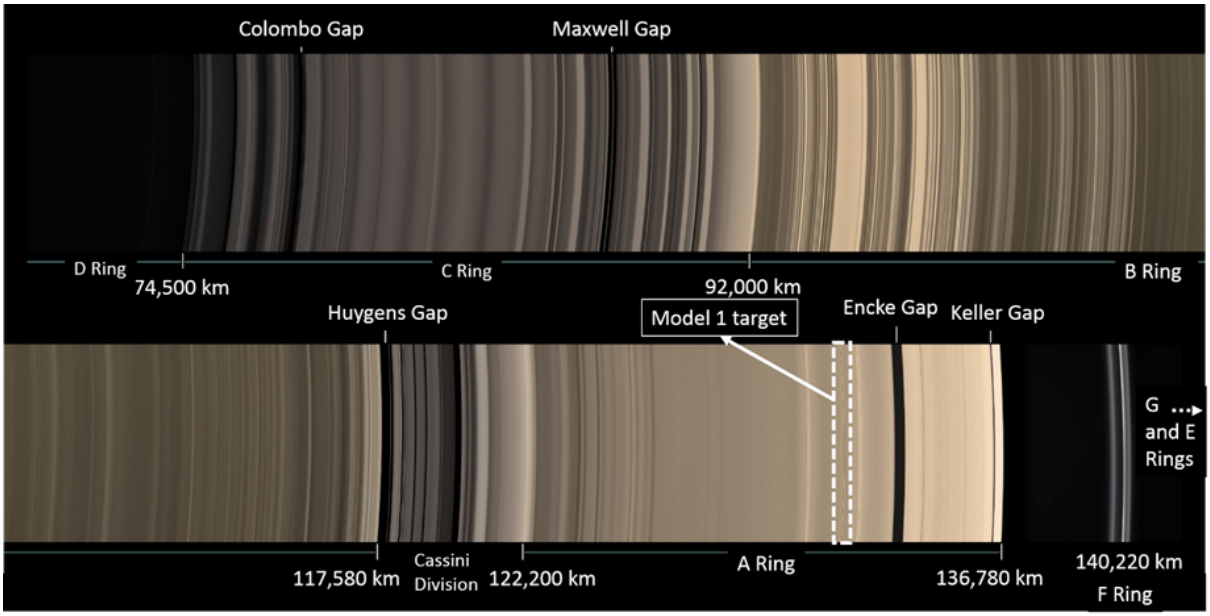

Figure 1.1: Mosaic of the rings of Saturn. The dashed white square encircles the area of the ring which we will model—which lies in the A ring. A bending wave caused by the satellite Mimas is present in this ringlet which extends 200 km in the radial direction. Pictures taken by the Imaging Science Subsystem - Narrow Angle camera. Image credit: NASA/JPL/Space Science Institute

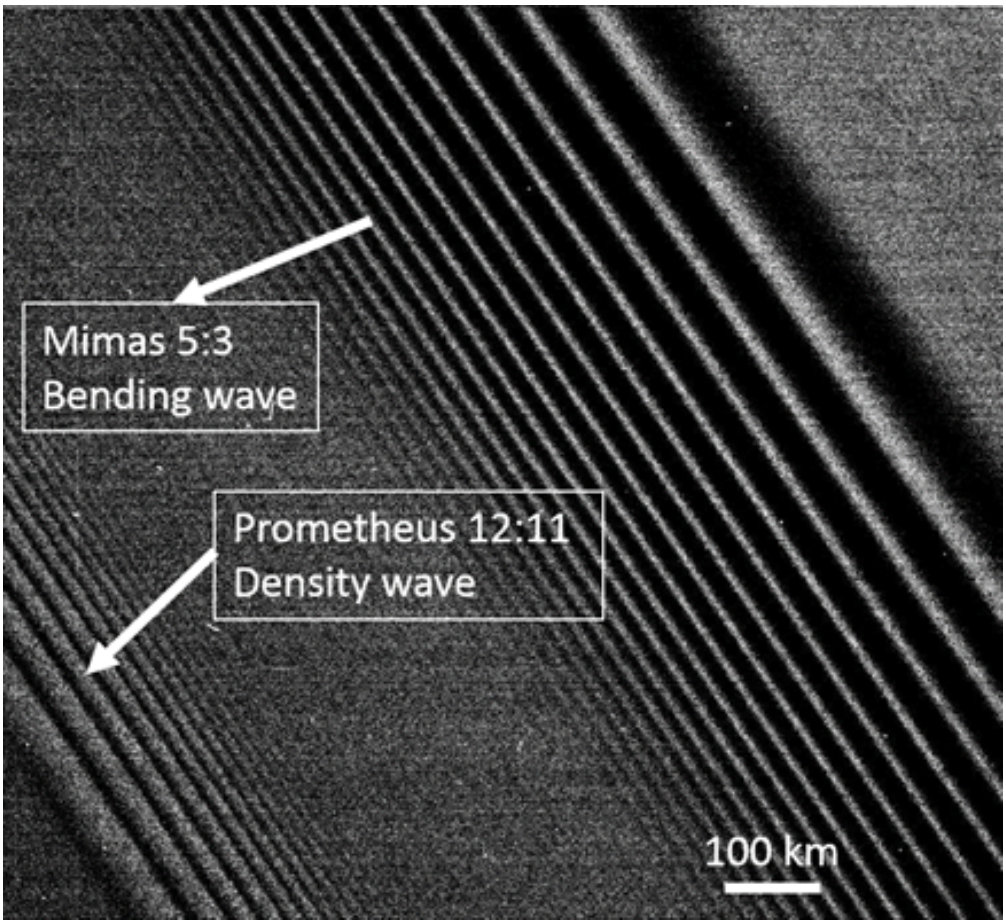

Figure 1.2: Close-up picture taken by the Cassini visual camera for the Mimas 5:3 bending wave (the target of our model) and the neighboring Prometheus 12:11 density wave. The A-ring of Saturn is home to many such waves produced by the gravitational perturbation of satellites that orbit outside of the rings. Image credit: NASA/JPL/Space Science Institute

(where the clumps are self-gravity wakes). We will show that adding self-gravity wakes in this manner explains striking observational features measured by the Cassini spacecraft. Moreover, the approximate nature of our model serves to provide more insight into the phenomena; specifically, it highlights the importance of the dynamics of self-gravity wakes within the BW in the explanation.

1.4 The Ions in a Reconnecting Region of Earth's Magnetotail

Magnetic reconnection occurs when opposite-facing magnetic field lines, which are moving through space, meet at a point and add up to a net zero (or close to zero) magnetic field. This canceling out of the magnetic field is the reason the phenomenon is also dubbed magnetic annihilation. When this annihilation occurs, charged particles that are traveling with such magnetic field lines in helicoidal orbits tend to get energized as the magnetic energy is transferred into the kinetic energy of electrons or ions.

The Earth's magnetotail is an ideal spot to study reconnection. Earth naturally has a dipole-like magnetic field (Figure 1.3, left). Nevertheless, due to interactions with the Solar wind, this magnetic field gets distorted. The result is that, on the dusk side of Earth (the anti-sunward side), the magnetic field lines in the Northern hemisphere (roughly, due to the tilt of the Earth) are facing towards the Earth, while the lines in the Southern side are facing away from the Earth (Figure 1.3, right). At the equatorial region (roughly the equatorial region, because of the tilt of the Earth) these opposite-facing lines meet, and magnetic reconnection occurs there continually. This reconnection causes the flow of the plasma coming from the Sun to be non-laminar, and turbulence emerges in the region. Multiple Spacecrafts in this region have measured turbulent fields: Geotail (Angelopoulos et al., 1994), ISEE-2 (Borovsky et al., 1997), Cluster (Artemyev et al., 2010), and, most recently, MMS (Ergun et al., 2018). They have also measured highly energized ions (moving nearly at $0.02c$ where c is the speed of light). The average speed of ions in the region is: $\approx 0.0001c$. Nevertheless, it is unclear how the ions get accelerated to such high speeds.

The model we use to explain the acceleration of the ions consists of investigating how test-ions react to the fields measured by the MMS spacecraft in that specific region of the Earth's magnetotail. These measured fields present a turbulence pattern, that is, locally the magnetotail fields no longer have the ordered laminar structure seen in Figure 1.3 (right) but present a range of directions, and magnitudes that

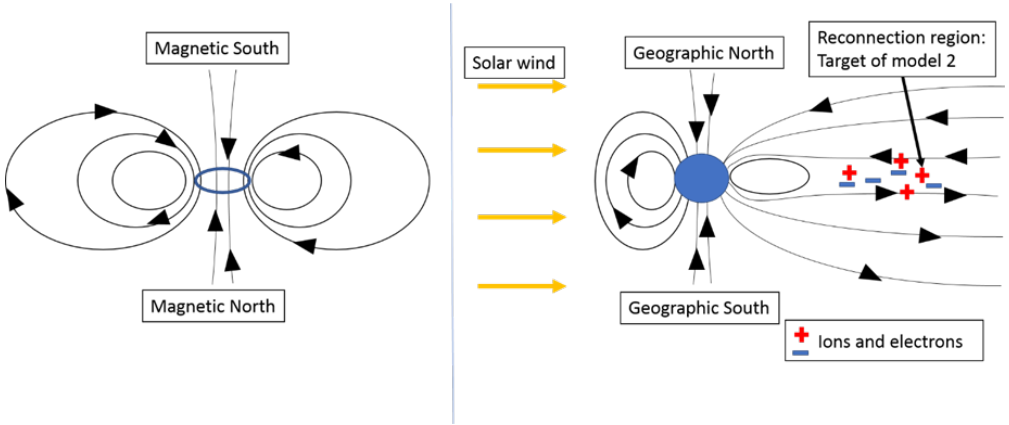

Figure 1.3: (Left) Diagram of a magnetic dipole. (Right) the Earth's magnetosphere. Reconnection occurs when the opposite phasing magnetic field lines meet at the reconnection region; also called the current sheet region due to the presence of a plasma current in the region due to the electric displacement field that arises there.

significantly exceed the background values of the laminar case. We are interested in knowing if test-ions under these conditions would reach the energies we measure. Test-ions are hypothetical ions that produce no electromagnetic fields. Such ions do not actually exist. If the turbulent fields are big enough so that the fields of the ions are small in comparison, we can say that the ions possess a test-charge and treat them as test-ion. This type of model is common in introductory physics textbooks.

Unfortunately, the ion-generated fields magnetic fields are not small in comparison to those present in the Earth's magnetotail. Nevertheless, our model still investigates how an ion population reacts to the measured fields, and if they get accelerated and how they get accelerated, without including the potentially important magnetic fields generated by this population. It is possible that the measured fields already "contain" these ion-generated fields, but that is not known with certainty. Even so, it is not how we justify the distortion of our model. We will argue, after presenting the model, that understanding how a population of test-ions behaves under the MMS-measured fields is important for understanding how real ions get accelerated. This is true regardless of whether the field of the ions is being accounted for by the applied fields or not. This is because while our model does not capture all the details of the target, it captures the relevant details for the purpose of the model. We know that it captures the relevant details because it reproduces the energies seen in the data. Hence, the behavior of test-ions is a meaningful first step in the overarching project of solving ion acceleration in the Earth's magnetotail.

Thus, idealizations and abstractions—like ignoring Ampere's law for the dynamics of ions, or taking self-gravity wakes to be rigid in the case of Saturn's A-ring— greatly aids our ability to explain the phenomena in question. This is the main claim of this work. In the next two chapters we will present with scrutinous scientific detail the two models in question, and their agreement with the data. After this, we will be in a position to further argue for this claim by pointing at the specific features of our models that do the explaining and the describing, respectively; thereby answering the questions we have raised in this introduction.

Chapter 2

The Dynamics of Self-gravity Wakes in the Mimas 5:3 Bending Wave: Modifying the Linear Theory

2.1 Preface

This chapter was submitted as a research article to *Icarus* in December 2022. Since, it has been through three rounds of suggestions by two anonymous reviewers—the last one consisting mostly of minor revisions. The conceptualization of the problem was done jointly between Josh Colwell and myself, based on the puzzles presented in Gresh et al. (1986). The problem-solving strategy was done mostly by myself, with inputs from coauthors (Glen Stewart, Girish Duvvuri, Richard Jerousek, Josh Colwell, and Larry Esposito). The majority of the data analysis portion was conducted by myself; Richard Jerousek helped with organizing the dataset and providing the coordinates for Mimas. The work was funded by the NASA FINESST award No 80NSSC20K1379.

2.2 Introduction

A bending wave (BW) is a warping of a disk (a circular and thin mass plane) caused by perturbations normal to the disk that propagates due to self-gravity. Warped disks and their propagation are only understood to a limited extent since the models do not match observations in various aspects (for instance, see Nelson & Tremaine 1995 for an overview in the context of galaxies). Warped disks are seen in many fields within astrophysics and can be found around young stars (Epstein-Martin et al., 2022), black holes (Thomas et al., 2021), and around planets (Shu et al., 1983), for which we have a vast amount of observations available. In the case of the rings of Saturn, the out-of-the-plane force is produced when satellites

with inclined orbits perturb the ring particles at a frequency that coincides with a rational multiple of these particles' vertical motion at some radial distance from Saturn. Many of these resonances occur in the A ring of Saturn, where we focus on the 5:3 vertical resonance due to the moon Mimas at $131902\,\mathrm{km}$ from Saturn's center. A radial cut through an idealized bending wave is shown on the top panel of Figure 2.1.

Shu et al. (1983) (henceforth SCL) were the first to confirm the presence of bending waves in the rings by adapting the theory of warped galaxies developed by Bertin & Mark (1980) and analyzing images from Voyager I. While there was general agreement with the SCL theory for weak bending waves, the Mimas 5:3 BW proved difficult to fit to the SCL theory. Later, Lissauer et al. (1984) focused on this specific wave and obtained a value for the viscosity by using similar methods. A general study of waves using occultations from Voyager's photopolarimeter was then done by Esposito et al. (1983), while Gresh et al. (1986) did an extensive study focusing on bending waves using low opening angle radio occultations. Neither managed to explain the shape of the Mimas 5:3 bending wave, and Gresh et al. (1986) suggested that the damping mechanism from the Mimas 5:3 bending wave needed to be revised. On the theoretical side, Chakrabarti considered radial shear of particles as a damping mechanism for the Mimas 5:3 BW but it yielded an inconsistent result for the viscosity (Chakrabarti, 1988, 1989). All of these efforts were based on the Voyager observations; however, Cassini data has yet to be used to improve the theory of bending waves.

Figure 2.1 shows how stellar occultations (which are photometric measurements of a star as it is occulted by the rings) can inform us of the local shape of the rings. From looking at Cassini occultations (Figures 2.2 and 2.3), and by comparing to Gresh et al. (1986), we have identified 3 ways in which the SCL model fails:

(1) Wave profile.

The poor prediction of the wave's morphology can be observed in Figure 2.2, where we show a plot of the optical depth of an occultation of the star γ-Pegasus measured by UVIS compared to SCL theory. The effective opening angle of an occultation is defined as $B_{\mathrm{eff}} = \tan^{-1}(\tan B/\cos\phi)$ where B is the angle between the mean ring plane and the incident light rays, and ϕ the angle between the radial direction and the light rays, projected onto the plane (see Gresh et al. 1986); the lower B_{eff} is, the higher the variations in the optical depth. The peaks and troughs of this optical depth are created by the inclination, or the slope, of

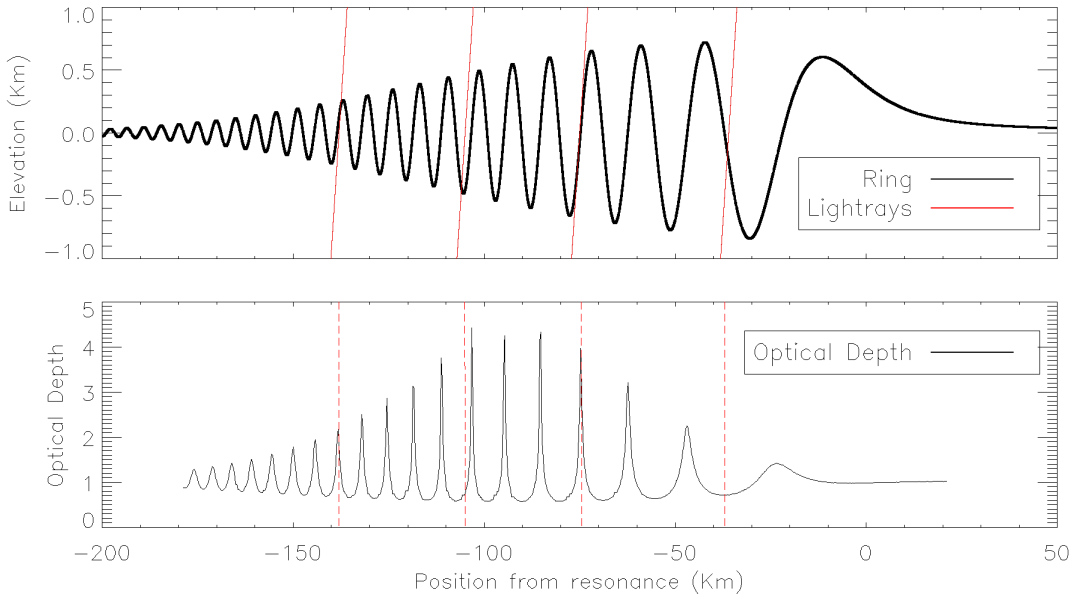

Figure 2.1: Radial cut of the Mimas 5:3 bending wave according to Shu et al. (1983) (top panel) and its predicted optical depth profile (bottom panel). The red rays in the top panel represent light rays that are being transmitted through the ring, and the corresponding optical depth probed for each light ray is marked by the red dashed lines in the bottom panel. Because the coordinates don't have the same scale, the rays look vertical, but the angle between the mean ring plane and the incident light rays is $B = 26°$, and the angle between the radial direction and the lightrays, projected onto the plane, is $\phi = 0°$. We can see how the lightrays go through more material when the lightray aligns with a slope (which corresponds to a peak in optical depth), and through less material when the lightray travels perpendicular to the slope (which corresponds to a trough in optical depth).

the ring relative to the line-of-sight to the star, and the observed discrepancies suggest that the SCL theory overpredicts this inclination. The increase of the optical depth relative to the background in the troughs of the occultation profile further indicates that there is extra material attenuating the light in the regions where the theory predicts a higher photon count.

SCL theory also predicts that all variation of the optical depth of the disk relative to the flat ring is caused only by the inclination of the ring; therefore, in occultations where the line-of-sight is normal to the rings, no variation of optical depth is expected. In the left panel of Figure 2.3, however, the data shows otherwise. An approximately normal (to the rings) occultation still shows a symmetric variation of the optical depth, centered about $80\,\mathrm{km}$ inside the point of the perturbation (the location of the resonance), which suggests an extra layer of material being generated by this perturbation that may be caused by the fragmentation of particles in the ring (Gresh et al., 1986). The position of the peak and the overall shape of this optical depth enhancement is correlated with the theoretical prediction for the maximum *slope* of the wave instead of the maximum elevation, which further suggests that this fragmentation is higher where the slope of the ring is steeper (Figure 2.3). In this work we suggest a plausible physical mechanism, derived from first principles, that explains this extra layer of particles.

This suggested extra layer of particles could be described as a haze, as a comparison between the Visible and Infrared Mapping Spectrometer (VIMS) and UVIS data (see Table 2.1) show the presence of a small amount of sub-mm size particles which diffract the infrared light out of the detector increasing the infrared optical depth (Jerousek et al., 2016). This is an uncommon sight in the A-ring as sub-mm particles normally are rapidly accreted into bigger particles (Bodrova et al., 2012; Harbison et al., 2013), further motivating a modification of SCL theory that accounts for the disruption of material in the BW region.

	$\lambda\,[\mathrm{nm}]$	$\frac{\bar{\tau}_{\mathrm{wave}}}{\bar{\tau}_{\mathrm{bg}}}\,[-]$
VIMS	$2886 - 2977$	$1.520 + 0.026\,/\,-0.025$
UVIS	$110 - 190$	$1.352 + 0.028\,/\,-0.027$

Table 2.1: Simultaneous Infrared and Ultraviolet occultations of α-Scorpius taken by the VIMS and UVIS instruments, respectively. VIMS optical depth is larger by 13% compared to UVIS. For τ_{bg} we averaged from kilometers $r = 131862$ to $r = 131762$ (in the flat ring region). For τ_{wave} we averaged from kilometers 131600 to 131700.

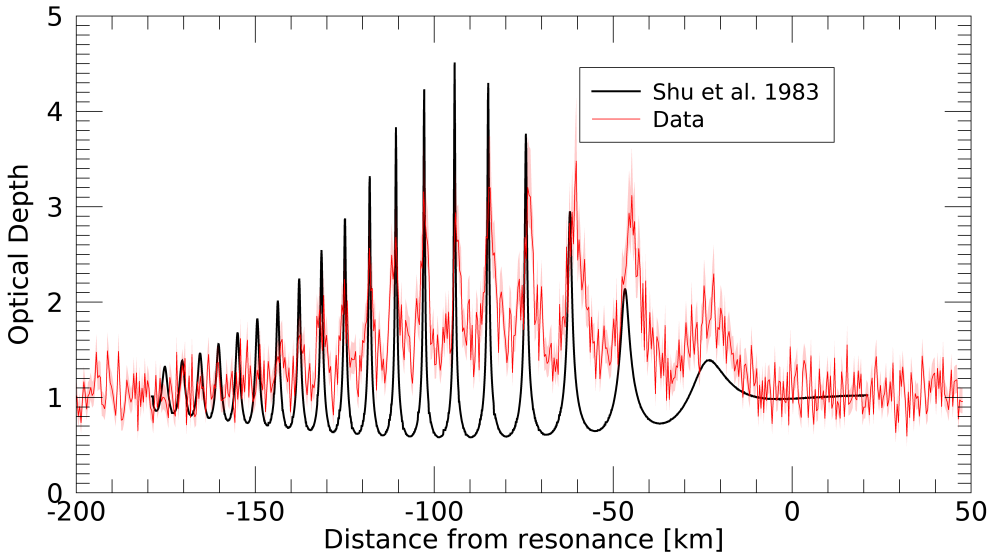

Figure 2.2: We compare an occultation of γ-Pegasus (rev 32I, $B = 20.3°$, $B_{\rm eff} = 26°$) seen by Cassini (red) to the standard bending wave theory (black). The resonance occurs at a radius of $131902\,\mathrm{km}$ and the wave propagates towards Saturn (left of the plot). We see three major discrepancies: (1) The SCL theory overpredicts the peaks of the optical depth and underpredicts the troughs. (2) The wavelengths do not match for the first three cycles. (3) The theory underpredicts how fast the wave damps, as peaks are still predicted to appear around $-150\,\mathrm{km}$, but the observed wave gets buried in the noise before that point. Using the viscosity of $\nu = 260\,\mathrm{cm}^2/\mathrm{s}$ from Lissauer et al. (1984)'s analysis of this wave and Tiscareno et al. (2007)'s analysis of the Prometheus 11:12 density wave.

(2) Wavelength near resonance.

Figure 2.2 indicates that, while the theoretical wavelength works fairly well at later wave crests (this wave propagates to the left in the plot), it differs from observed values near resonance, a result seen in Gresh et al. (1986). These discrepancies in the first cycles suggest an oversimplification in the calculation of the self-gravity force of a warped disk or that the surface mass density is not uniform across the wave.

(3) Viscosity.

The ring's viscosity controls the shape and amplitude of the peaks of the optical depth profile seen in Figure 2.2. Viscous interactions reduce the vertical displacement of ring particles; which, in turn, changes the maximum extinction at the point where the ring's slope and the line-of-sight coincide. In other words, the peak amplitude of the optical depth pattern depends on the viscosity. In Figure 2.2 the SCL model (black line) predicts a highly peaked optical depth profile and a wave that propagates beyond the observed variations seen in the data (red line). This suggests that the viscous fluid description of the damping is inadequate, and/or the values suggested by previous Mimas 5:3 BW studies (Lissauer et al., 1984; Gresh et al., 1986), and Cassini density waves studies (Tiscareno et al., 2007), are too low to describe this wave. Regardless, the observed peaks of the optical depth and how fast the wave damps indicate that the current theory underpredicts the amount of energy and momentum diffusion that occurs in the rings.

All three issues can be explored in depth using Cassini ring occultation data. Cassini observed the Mimas 5:3 bending wave in 217 occultations with the UVIS High Speed Photometer (HSP) (Esposito et al., 2004) out of which 130 have a signal-to-noise high enough to detect the variations in the data due to the bending wave. Moreover, using Cassini data, Colwell et al. (2006) confirmed the existence of *self-gravity wakes*, which are elongated clumps of particles that periodically disaggregate, and are 10 to 100 times bigger than a typical A ring particle ($\sim 1\,\mathrm{m}$). The consequences of adding self-gravity wakes to the SCL theory are derived in section §2.3 via the assumption that they react to the relevant torques as rigid bodies; here we derive, from first principles, a plausible mechanism that explains the extra optical depth signal seen in normal occultations. In section §2.4 we describe the transmission model, our selection criteria for the 60 UVIS occultations used, and how the data were reduced. In section §2.5 we describe the ray-tracing code. In section §2.6 we compare our bending wave model to the data followed by a discussion in section §2.7, where

we consider how our model addresses the above problems. In section §2.8 we summarize our conclusions.

2.3 Self-gravity wakes and the Bending wave

Self-gravity wakes are clumps of particles with an elongated structure at an angle θ_w from the azimuthal direction (see Figure 2.4), which are held together by self-gravity against the Keplerian shear, and whose constituent particles present a resistance to changing their relative distances, $\Delta r_{ij} \approx 0$ (Daisaka & Ida, 1999; Lu et al., 2018). In other words, they tend to behave like a rigid body, keeping a consistent shape and orientation over an orbital period. Self-gravity wakes were first hypothesized in the galactic context (Toomre, 1964) as non-axisymmetric disturbances generated by the interplay of the self-gravity of a Keplerian disk and its shear. They were first proposed to exist in the rings by Colombo et al. (1976), and Dones & Porco (1989) and Dunn et al. (2004) modeled and corroborated their effects on Voyager images and Very Large Array observations, respectively. They were first numerically modeled for planetary rings by Salo (1992), and were detected in Saturn's rings in Colwell et al. (2006) as an azimuthal asymmetry in the optical depth of UVIS occultations.

The SCL linear bending wave theory takes the rings to be smooth and of uniform density, so the presence of these structures was not accounted for in the dynamics. To study the effects of self-gravity wakes we assume that they remain rigid at least during the time it takes the wave to advance one wavelength in the frame co-rotating with the wake, which is about one orbital period (see Eqn. 2.2 below). Self-gravity wakes are expected to remain together for at least that long (Karjalainen & Salo, 2004): some simulations even showing lifetimes of many orbital periods (Michikoshi et al., 2015).

Within the BW the wakes are subjected to different torques that affect their orientation as they oscillate vertically with the wave, these are computed in section §2.3.1. The equations that couple the orientation ($\theta_{q'}$, see Figure 2.5) of the wakes with the elevation of the particle (z) are integrated in section §2.3.2. As the wakes change their orientation, the regolith at some distance from their center will gain a difference in vertical speed with respect to the surrounding ring particles (which are assumed to follow the expected SCL vertical motion), resulting in collisions on the order of $1\,\mathrm{cm/s}$ relative velocities which release material residing on the wake's surface. The predicted properties of the resultant 'haze' are described in section

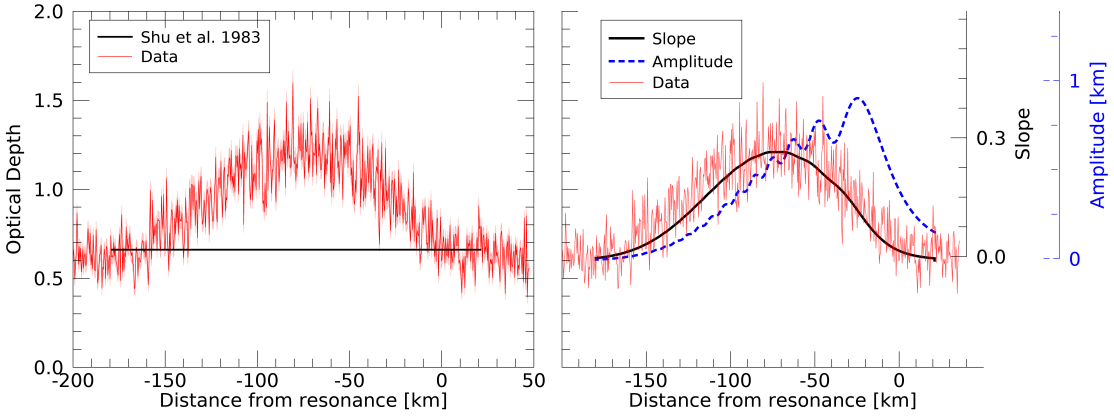

Figure 2.3: Left panel: we compare an occultation of β-Centauri (rev85I, $B = 66.7°$, $B_{\rm eff} = 87°$) (solid red), to the SCL model (solid back). The error bars are shown by a light red filled curved in the background of the plot. The SCL theory predicts a uniform optical depth; however, the data shows a symmetric rise in the optical depth centered at $-80\,\mathrm{km}$ from resonance. Right panel: The same optical depth profile of β-Centauri (solid red) is now compared to the theoretical (SCL theory) maximum slope of the wave (solid black) and the amplitude of the wave (dashed blue) for a viscosity of $566\,\mathrm{cm}^2/\mathrm{s}$ and a ring surface density of $\sigma = 36.3\,\mathrm{g}/\mathrm{cm}^2$; these values are the best-fit wave parameters of the model presented in this paper.

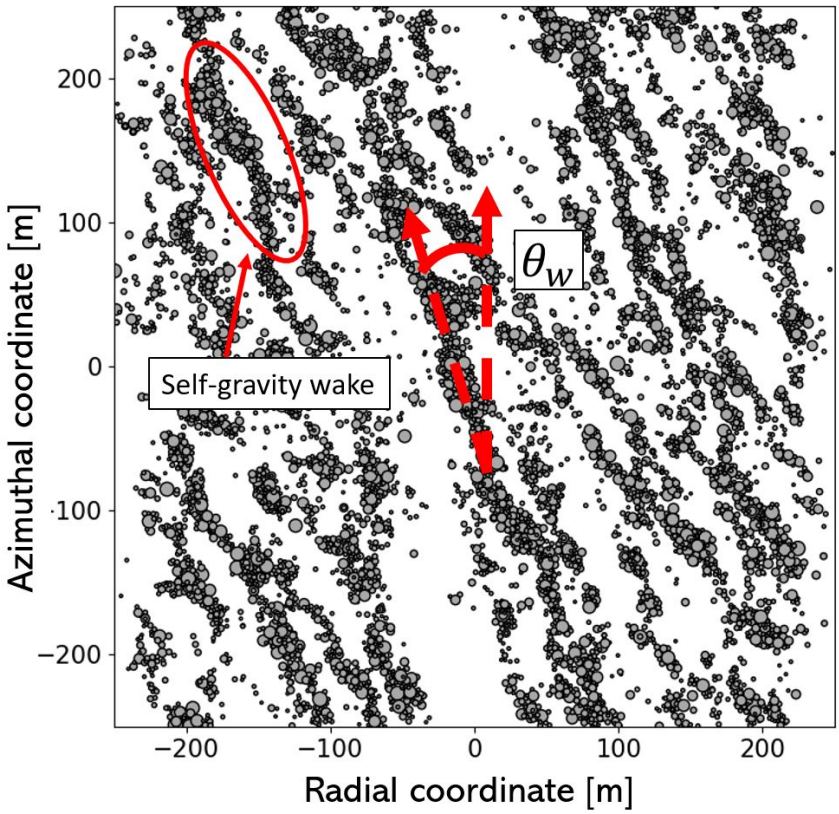

Figure 2.4: Snapshot of self-gravity wakes in a shear-box simulation produced with the shear-sheet `REBOUND` example (Rein & Liu, 2012), for visualization purposes only. Circled in red we can see an oriented self-gravity wake; we can also see they tend to point at an angle θ_w with the azimuthal.

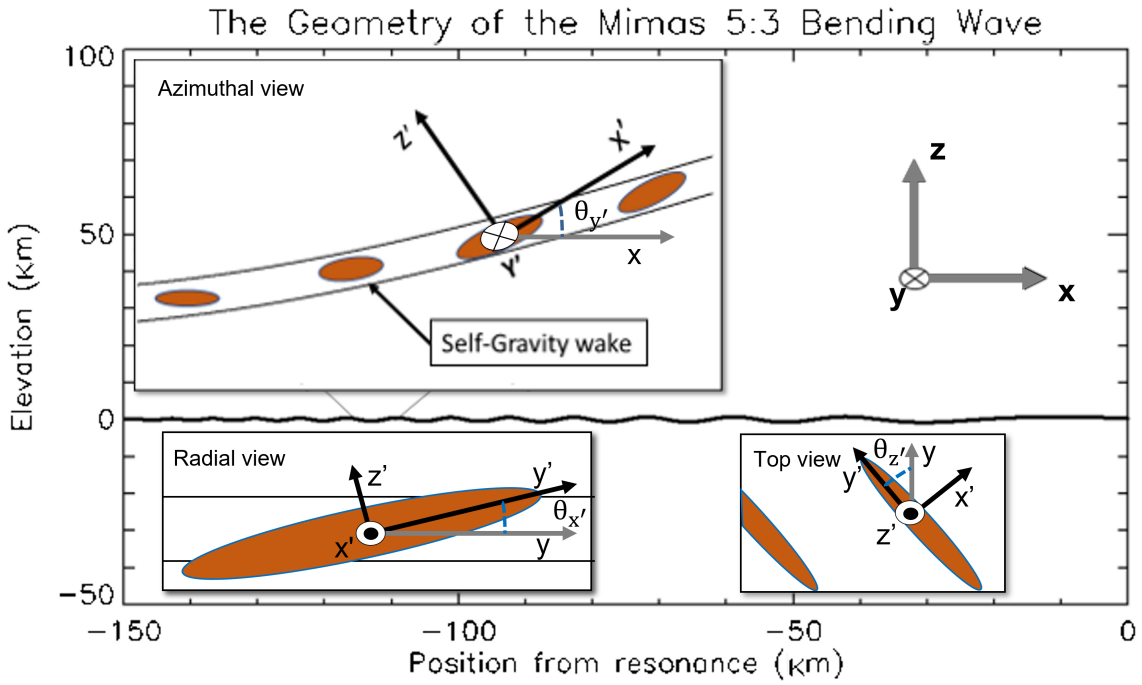

Figure 2.5: Bending wave (to scale) and the two frames of reference used in this work. The frame on the right is centered at resonance ($r = 0$ at resonance), co-rotating and defined by the unprimed axis $(\hat{x}, \hat{y}, \hat{z})$ while the Eulerian frame on the wakes (top left) is centered on the center of mass of a self-gravity wake at a distance r from resonance and it is defined by the primed coordinates $(\hat{x'}, \hat{y'}, \hat{z'})$. We also represent here the angles $\theta_{q'} = \int \omega_{q'} dt$ where $\omega_{q'}$ is the angular velocity of a rotation about the q'-axis where q' can be x', y', or z' (the principal axes of the wake). We set the initial angles to be 0 when prime and unprimed axis are aligned.

§2.3.3.

2.3.1 The Coupling Equations

To derive these equations we set the reference frame in the center of mass (CM) of a wake a distance r from Saturn (see Figure 2.5), and take the time dependence of the vertical coordinate, z, of the CM to act harmonically in time with a frequency Doppler-shifted by the orbit of the wake:

$$\omega' = m(\Omega_M - \Omega) + \mu_M \tag{2.1}$$

where Ω is the Keplerian frequency of the wake's CM, and Ω_M and μ_M are the Keplerian and vertical frequencies of Mimas, and m is the azimuthal wave number ($m = 4$ for our case). This is in accord with the SCL linear BW theory translated to a co-rotating frame represented by the unprimed frame (x, y, z) in Figure 2.5, where x and y are the local radial and azimuthal coordinates respectively. We also introduce angle coordinates which represent rotations about the principal axis of rotation (x', y', z') of the wake and for concreteness consider the wake to be a parallelopiped (or a 'granola bar') with sides $(W, L, H) = (18\,\mathrm{m}, 232\,\mathrm{m}, 4\,\mathrm{m})$ accordingly. We extract these dimensions from transmission models of the A ring (Hedman et al., 2007; Jerousek et al., 2016), and numerical simulations (Salo et al., 2018) where $H/W \sim 0.2$, $L \sim 4\lambda_T$ and $W \sim \lambda_T/3$; $\lambda_T \equiv 4\pi^2 G\sigma/\Omega^2 \sim 58\,\mathrm{m}$ is Toomre critical wavelength (Toomre, 1964), where σ is the surface mass density and Ω the Keplerian frequency.

The motion of a regolith particle at a point (x', y', z') with respect to the unprimed co-rotating frame will then be given by adding the CM velocity (whose motion is governed by the SCL theory) to the velocity due to the wake's rotation, derived below. The equation for the z-coordinate for the CM of a wake a distance x_V from resonance as a function of time t is given by:

$$z(x_V, t) = \mathrm{Re}\big[h(x_V)e^{i(\omega' t)}\big] \tag{2.2}$$

where $h(x_V)$ contains a complex Fresnel integral, the wave amplitude, and the damping term $e^{-(\frac{x_V}{\chi_D})^{-3}}$ — where χ_D is the damping length which depends on the viscosity ν — and where ω' is the Doppler-

shifted forcing frequency. While for $kx_V >> 1$, the wave profile $h(x_V)$ takes a WKBJ form $h(x_V) \sim A(r)e^{\int ikdx_V}$, we will use the exact expressions for the amplitude ($\sqrt{hh^*}$) and slope's magnitude ($\sqrt{\frac{dh}{dr}(\frac{dh}{dr})^*}$). In Appendix C, Eqn. (2.2) is derived from first principles.

Note that we have eliminated z's usual explicit dependence on azimuthal position, Θ, by using the Doppler-shifted frequency ω', which amounts to making the substitution $\Theta = \Omega t$ in Eqn. 26 of SCL. In other words, we are moving from an Eulerian to a co-rotating Lagrangian description of the rings. Thus, the Lagrangian derivative used in SCL, $D/Dt = \partial/\partial t + \Omega\partial/\partial\Theta$, becomes the time derivative $\partial/\partial t$ in the co-rotating frame.

Knowing the motion of the CM of a wake at a distance x_V from resonance, we proceed to compute the relevant torques on the wake to find its rotational motion. These torques are: the tidal torque due to Saturn ($\tau_{\rm tidal}$, §2.3.1.1), the torque due to the Keplerian shear ($\tau_{\rm Kep}$, §2.3.1.2), the acceleration torque due to the BW ($\tau_{\rm BWacc}$, §2.3.1.3), the torque due to the vertical shear of the BW ($\tau_{\rm BWsh}$, §2.3.1.4), and the torque due to the wake to wake gravitational interaction ($\tau_{\rm wake}$, §2.3.1.6). All of these torques will be taken with respect to the principal axes of the wake.

2.3.1.1 Tidal torque

We begin by deriving the torques about the z'-axis, which are also present outside the BW region. We assume that the wake's inclination outside the ring's mean plane remains small, so that $\theta_{x'}, \theta_{y'} < 15^\circ$ and $\theta_{z'}$ represents the pitch-angle of the self-gravity wake (in Appendix A we show the general expression for an arbitrary wake orientation). The torques about the z'-axis are the the tidal torque—which tends to align the wake's long-axis with the radial direction—and the Keplerian shear torque that aligns the wake with the azimuthal. Later, we will see how the BW torques change this picture.

We start with the tidal force in polar form (Murray & Dermott, 2000)

$$F_{\rm tidal} = 3\frac{GM_S}{a^3}y' * \sin\theta_{z'}\cos\theta_{z'}dm$$

where a is the distance from Saturn's center, G the gravitational constant, M_s the mass of Saturn and y' the coordinate along the long-axis of the wake. Using $dm = HW\rho_w dy'$ for the differential mass of the wake

(where ρ_w is the wake's density) and integrating with respect to y' we arrive at the tidal torque:

$$\tau_{\text{tidal};z'} = 2\frac{GM_S}{a^3}\sin\theta_{z'}\cos\theta_{z'}\left(\frac{L}{2}\right)^3 * \rho_{\text{Roche}}HW \tag{2.3}$$

For the density of the wake (ρ_w) we will use ρ_{Roche}, defined as the bulk-density of an object that fills its Hill sphere (Tiscareno et al., 2013). Aggregates within the rings, such as moonlets, have been shown to have this density within a 20% margin (Porco et al., 2007), and numerical simulations have shown similar results for self-gravity wakes (Salo et al., 2018). Notice that this torque is positive when $0 < \theta_{z'} < 90°$ and becomes negative when $\theta_{z'} > 90°$, causing the pitch-angle to orient radially.

2.3.1.2 Keplerian shear torque: explaining the pitch-angle

To compute the torque due to the collisions of the Keplerian shear we have to consider the 3-Body Hill's problem. As done in Morishima & Salo (2004) and Yasui et al. (2014) for the case of embedded moonlets, we integrate the Hill equations in 3D to find the colliding trajectories of the ring particles:

$$\begin{aligned}\ddot{x} - 2\dot{y} &= \frac{\partial U_H}{\partial x}\\ \ddot{y} + 2\dot{x} &= \frac{\partial U_H}{\partial x}\\ \ddot{z} &= \frac{\partial U_H}{\partial z}\end{aligned} \tag{2.4}$$

The Hill potential (U_H) consists of the tidal potential ($\frac{3}{2}x^2$) plus the potential of a line of mass of finite size, modified to allow for arbitrary wake orientations. The zero-velocity curves for this potential are shown in Figure 2.6; once the collisions change the orientation of the wake, the trajectories are recalculated with the updated potential. The particles that are radially inward orbit faster than the CM of the wake, and hence they will tend to align the wake with the azimuthal direction; the radially outward particles have the same effect. To find the colliding trajectories we integrate the Hill equations to then compute the rate of momentum transfer into the self-gravity wake:

$$\boldsymbol{\tau}_{\text{Kep};z'} = 2(1+\epsilon)(x'\times y')\int y'\frac{dp_\perp}{dt} = 2(1+\epsilon)(x'\times y')\int_{z_{\min}}^{z_{\max}}\int_0^{\frac{L}{2}}\rho_s(z)|v_\perp|v_\perp y' dy' dz' \tag{2.5}$$

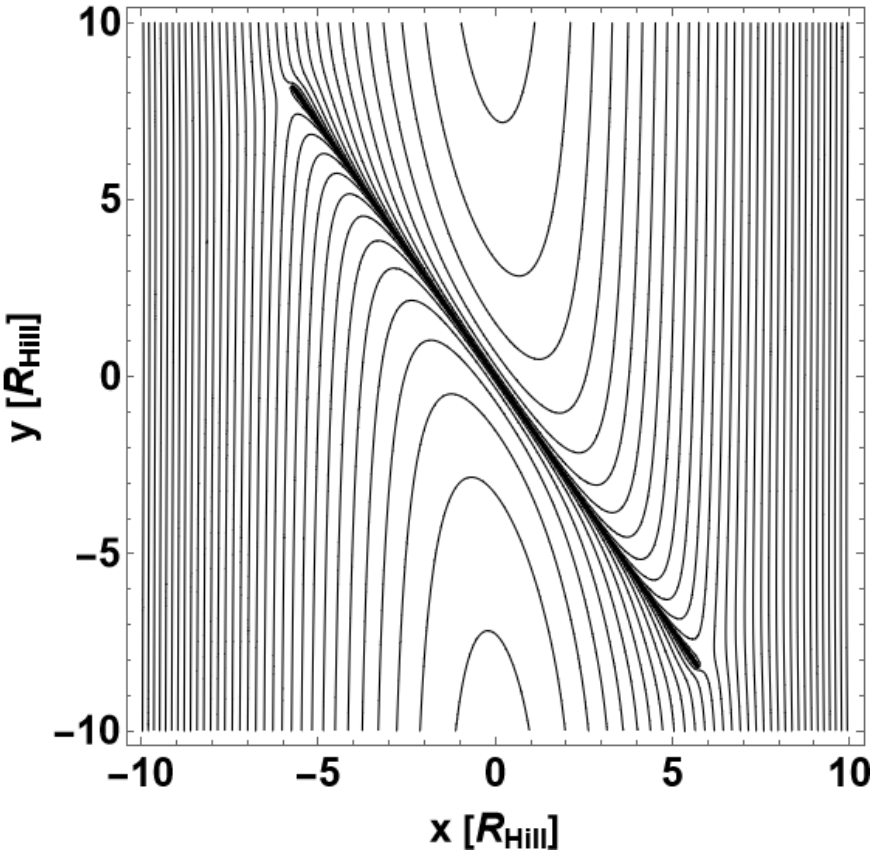

Figure 2.6: Zero-velocity curves of the Hill potential of a line of mass oriented 45° from the azimuthal. The self-gravity wake's potential is modeled as a uniform line of mass of length L.

where ρ_s is the space density of the colliding particles and $p_\perp$ and $v_\perp$ are the momentum and velocity perpendicular to the long axis of the wake, ϵ is the coefficient of restitution. To numerically compute this integral we create a grid of particles for the incoming impact parameter b and the vertical coordinate z, where $\Delta b = \Delta z = 0.01 r_H$ where r_H is the Hill radius that was taken to be $\frac{W}{2} = 9\,\mathrm{m}$ (which is consistent with our value for ρ_{Roche}). The highest and lowest initial z values of particles that collide with the wake are $z_{\max}$ and $z_{\min}$ respectively. We use the vertical density profile $\rho_s(z) = e^{-(\frac{z}{z_0})^2}$ where z_0 is the rings half thickness which was taken to be $5\,\mathrm{m}$ and a temporal resolution of $dt = 0.01T$ where T is the orbital period at resonance.

We proceed to study the angle at which the torques equilibrate in the case of a single self-gravity wake as a way to test our framework. The total torque in the z-axis can be written as:

$$\tau_{z'} = \tau_{\mathrm{tidal}}(\theta_{z'}) + \tau_{\mathrm{Kep};z'}(\theta_{z'}, \rho_s, \epsilon) \tag{2.6}$$

We find that these torques equilibrate stably at $\theta_{z'} = 25^\circ$ when $\rho_s \approx 425,\ 500\,\mathrm{kg/m^3}$ for $\epsilon = 1,\ 0.5$, respectively. This equilibrium angle is a boundary condition for our problem and any pair (ϵ, ρ_s) that achieves it yields the same wake motion inside the wave region. Figure 2.7 show how the pitch-angle derived by equilibrating the torques matches the one suggested by UVIS occultations (Colwell et al., 2006; Jerousek et al., 2016), and aligns with the pitch-angles apparent in shear-box simulations conducted with different shear rates (Michikoshi et al., 2015; Salo et al., 2018). As a reference for these space density (ρ_s) values, consider that a preliminary multiwavelength analysis suggests an average space density of $85\,\mathrm{kg/m^3}$ in between wakes (Jerousek, 2018); with this density the torques equilibrates at $\theta_{z'} = 50^\circ$ for $\epsilon = 1$. The higher value of $425\,\mathrm{kg/m^3}$ required by the 25° pitch-angle suggests that the material interacting with the wakes is more abundant than in the middle of the gaps between wakes. This is consistent with Tiscareno et al. (2010), which states that the density in the gap is better described by a bimodal distribution. Note that ρ_s is overestimated by our parallelepiped model for the wake: the lesser inertia of a more realistic ellipsoidal wake would increase the angular acceleration due to collisions while not affecting the tidal angular acceleration. This decreases the required ρ_s by the ratio of the inertia coefficients between the two models, $3/5$.

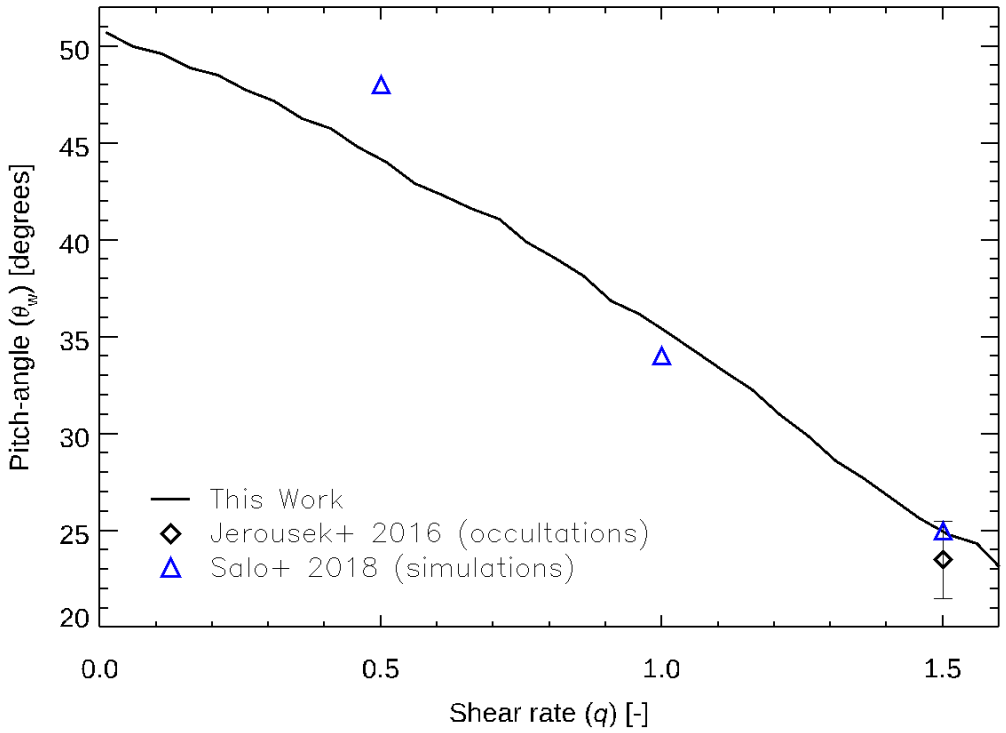

Figure 2.7: Relationship between the pitch-angle θ_w (see Figure 2.4) and the shear rate $q = -\frac{d \ln x\Omega}{d \ln x}$ where Ω is the Keplerian frequency and x the radial coordinate from Saturn. We calibrate our model to equilibrate at $\theta_w = 25°$ for $q = 1.5$ which is the case for the Mimas 5:3 BW. The blue triangles corresponds to equilibrium configuration extracted from a shear-box simulation presented in Figure 16.23 of Salo et al. (2018). The black square represents the values reported in Jerousek et al. (2016) at the region near the Mimas 5:3 BW (at a Saturncentric distance of 13.2 Mm) with the error bars representing the range of the values presented in Figure 7 of that work; the upper error bar given by the pitch-angle derived from UVIS occultations. Our rigid-body model matches the shear-box simulations' equilibrium angle within $4°$.

The computationally intensive nature of integrating the Hill equations self-consistently forces us to resort to a two-body approximation of the three-body problem. Specifically, a gravitational focusing approximation common in planet formation (Greenberg et al., 1991; Rafikov, 2004; Armitage, 2020), where the incoming speed of the scattering event can either be the dispersion velocity or the Keplerian velocity depending on which one dominates in the wave region. Cuzzi et al. (1979) already argued that the dispersion velocity dominates over the extent of a particle, but we find that both velocities are similar over the extent of the Hill radius of a wake. Thus, the safest approach for our case is to include 3-body corrections in our two-body approximation. From Greenberg et al. (1991) and Armitage (2020) we can get an approximate collision rate for our regime:

$$\frac{dM}{dt}(b) = q\Omega * b * \sigma * f * db \tag{2.7}$$

where f is the fraction of particles that enter the Hill sphere and collide, q is the shear rate $q = -d\ln x\Omega/dx$, Ω is the Keplerian frequency of the particle, b is the impact parameter and σ is the surface mass density of the disk. To get a torque we use two-body dynamics to find the speed and angle of incidence for the incoming particles at the moment of impact.

$$\tau_{\mathrm{Kep};z'} = 2(1+\epsilon)\int_{b_{\min}}^{b_{\max}} \frac{dM}{dt} v_\theta(b,\theta_{z'}) r_{2B}(b,\theta_{z'})$$

where $v_\theta(b) = b^2 * q\Omega/r_{2B}$ and

$$r_{2B}(b,\theta_{z'}) = \frac{\frac{(b^2 q\Omega)^2}{G\rho_{\mathrm{Roche}}WLH}}{1+e\cos(\theta_{z'}-\varpi)}$$

is the two-body orbit equation, where ϖ is the argument of periapsis taken from the azimuthal direction. We have set the true anomaly to the angular position at which the wake is oriented, which is the point in the orbit where the collision takes place (valid for the case of small $\theta_{x'}$ and $\theta_{y'}$). Here we are taking the angular momentum to be conserved about the CM of the wake, so that for a given impact parameter b we can determine a collisional speed v_θ at a distance r_{2B} from the CM. Under this approximation the trajectories of the colliding particles are hyperbolas and the three-body effects are accounted for by using Hill's equations to determine the limit of the integral $b_{\min}$. This and the length of the long axis (L) relative to the Hill radius,

which guarantees that particles entering the Hill sphere collide with the wake, allow us to do the following simplification of the Greenberg et al. (1991) formulation:

- f, the fraction of particles that collide after entering the Hill Sphere, is 1.
- Tadpole and horseshoe orbits are excluded from the colliding particles by using the three-body code to determine $b_{\min}$. We find that $b_{\min}$ varies from $35\,\mathrm{m}$ to $43\,\mathrm{m}$ with the different orientations of the wake (from radially aligned to the azimuthally aligned), with a mean value of $b_{\min} = 38\,\mathrm{m}$, which we use as a constant $b_{\min}$ for the two-body simulation.
- We define $b_{\max}$ as the solution of $r_{2B}(b_{\max}, \theta_{z'}) = \frac{L}{2}$

The collisional torque then becomes:

$$\tau_{\mathrm{Kep};z'} = -2(1+\epsilon)\int_{b_{\min}}^{b_{\max}} |v_\theta + \omega_{z'} r_{2B}|\,(v_\theta + \omega_{z'} r_{2B}) r_{2B} \int_{-\frac{H}{2}}^{\frac{H}{2}} \rho_s(z)\,dz\,db \tag{2.8}$$

where we have replaced the incoming speed in Eqn. (D.2) ($q\Omega b$) with $|v_\theta|$, used $\int_{-H/2}^{H/2}\rho_s(z)dz$ for σ. Additionally, by adding $\omega_{z'} r_{2B}$, we allow for the rotation of the wake to affect the incoming relative speed of the particles. This integral is solved numerically since we have to determine $b_{\max}$ every time the pitch angle $\theta_{z'}$ changes. For a Keplerian shear rate, we find that this formulation equilibrates stably with the tidal force (Eqn. D.1) at $\theta_{z'} = 25^\circ$ for $\rho_s = 500\,\mathrm{kg/m^3}$ and $\epsilon = 1$. Therefore Eqn. (2.6), with the Keplerean shear torque given by Eqn. (D.7), meets the boundary condition for the orientation of the wake outside of the wave. We proceed to explore the torques and the motion of the wake's inside the BW region.

2.3.1.3 BW acceleration torque

The main torque that causes the wakes' rotation in the BW region stems from the difference between the acceleration of the CM and that of a wake particle a radial distance Δx from the CM; we write this as $\ddot{z}_{\mathrm{CM}} - \ddot{z}(x)$. Given that all the torques are derived in the frame of the CM of the wake, differences in acceleration will appear as a force. To compute this force we take two time derivatives of Eqn. (2.2), which denotes the vertical position of a ring particle as governed by the interactions in SCL theory; namely,

the self-gravity of the bent ring, the gravitational force of Saturn, and a viscous force. Note that the time dependence of Eqn. (2.2) lies entirely in the exponential factor $e^{i\omega' t}$, and, given the $\sim 10\,\mathrm{km}$ wavelength and the tighyly-wound nature of the wave, the change of $z(x,\Theta)$ over a wake can be approximated linearly on Δx. The difference in vertical acceleration can then be expressed as:

$$\ddot{z}_{\mathrm{CM}} - \ddot{z} = -\omega'^2(z_{\mathrm{CM}} - z) \approx -\omega'^2 \left.\frac{dz}{dx}\right|_{\mathrm{CM}} \Delta x \tag{2.9}$$

Let's consider the rotation about the long axis (the y' axis). We need to find the directional derivative of $\ddot{z}(x)$ in the directions perpendicular to y'. Given the flattened nature of self-gravity wakes (Colwell et al., 2006; Hedman et al., 2007; Jerousek et al., 2016), variation of forces across the vertical axis, H, will be ignored and only variations along x' and y' will be considered. Then for the torque about y' we only need the variation of $\ddot{z}$ along the x' axis. The force then becomes:

$$F_z(x') = -\omega'^2 \left.\frac{dz}{dx}\right|_{\mathrm{CM}} (\hat{x}\cdot\hat{x'})x' dm \tag{2.10}$$

where dm is a differential mass a distance x' from the CM. Projecting it onto $\hat{z}'$ and crossing it with the lever arm we get:

$$\boldsymbol{\tau}_{\mathrm{BWacc},y'} = \boldsymbol{x'} \times \boldsymbol{F_{z'}} = -2\omega'^2 \left.\frac{\partial z}{\partial x'}\right|_{CM} (\hat{z}\cdot\hat{z}')(\hat{x}'\times\hat{z}') \int_0^{\frac{W}{2}} \rho_{\mathrm{Roche}} H L x'^2 dx' \tag{2.11}$$

where we substituted $dm = \rho_{\mathrm{Roche}} H * L * dx'$ and the directional derivative along x' defined as

$$\left.\frac{dz}{dx}\right|_{\mathrm{CM}} (\hat{x}\cdot\hat{x}') \equiv \left.\frac{\partial z}{\partial x'}\right|_{CM}$$

.

2.3.1.4 BW shear torque

The wake's CM vertical speed will differ from that of the neighboring particles and hence there will be a collision which will generate a torque. This is similar to the Keplerian torque and for the general case (see Appendix A) the vertical and horizontal speeds are added to compute a total collisional torque. If $\theta_{x'}$ and $\theta_{y'}$ are small however, this two torques are independent. To model the BW shear torque we consider the

shear $\frac{d\dot{z}}{dr}$ and note that the particles a distance y' along the long axis will have a relative vertical velocity of $\frac{d\dot{z}}{dr}(\hat{x}\cdot\hat{y'})$ with respect to the CM. If these particles have a space density ρ_s then the amount of mass colliding with the wake at a distance y' in a time dt will be:

$$M(r) = \rho_s \left| \frac{\partial \dot{z}}{\partial y'}\Big|_{CM} y' dt \right| W dy'$$

Which causes a momentum transfer of:

$$dp_{z'}(y') = [M] * [\Delta v_{z'}] = [\rho_s \left| \frac{\partial \dot{z}}{\partial y'}\Big|_{CM} y' \right| dt W dy'] * [(1+\epsilon)\frac{\partial \dot{z}}{\partial y'}\Big|_{CM} y']$$

This momentum transfer corresponds to a force of:

$$F_{\mathrm{BWsh};x'} = \frac{dp_{z'}}{dt} = (1+\epsilon)\rho_s \left| \left(\frac{\partial \dot{z}}{\partial y'}\Big|_{CM} - \omega_{x'} \right) y' \right| \left(\frac{\partial \dot{z}}{\partial y'}\Big|_{CM} - \omega_{x'} \right) W y' dy' \tag{2.12}$$

where we have included $\omega_{x'}$, the angular velocity about the x'-axis, to account for the change in the relative incoming speed that occurs when the wake rotates. The torque associated with this momentum transfer is:

$$\tau_{\mathrm{BWsh};x'} = 2\int_0^{\frac{L}{2}} y' \frac{dp_{z'}}{dt} = \frac{1+\epsilon}{2}\rho_s W \left| \frac{\partial \dot{z}}{\partial y'}\Big|_{CM} - \omega_{x'} \right| \left(\frac{\partial \dot{z}}{\partial y'}\Big|_{CM} - \omega_{x'} \right) \left(\frac{L}{2} \right)^4 \tag{2.13}$$

where we have taken the wake to be much more massive than the incoming ring particles so that the CM of the collision is the CM of the wake. Doing the same computation for $\tau_{\mathrm{vert};y'}$, we can arrive at the *total* torques about the x' and y' axis, now written as a function the angle $\theta_{z'}$ and radial distance x. For small angles $\theta_{x'}$ and $\theta_{y'}$ we have:

$$\tau_{x'} \approx -\frac{2}{3}\rho_{\mathrm{Roche}} H W \frac{d\ddot{z}}{dx}\Big|_{CM} \sin\theta_{z'} \left(\frac{L}{2} \right)^3 + \rho_s W \frac{1+\epsilon}{2} \left| \frac{d\dot{z}}{dx}\Big|_{CM} \sin\theta_{z'} - \omega_{x'} \right| \left(\frac{d\dot{z}}{dx}\Big|_{CM} \sin\theta_{z'} - \omega_{x'} \right) \left(\frac{L}{2} \right)^4 \tag{2.14}$$

$$\tau_{y'} \approx \frac{2}{3}\rho_{\mathrm{Roche}} H L \frac{d\ddot{z}}{dx}\Big|_{CM} \cos\theta_{z'} \left(\frac{W}{2} \right)^3 + \rho_s L \frac{1+\epsilon}{2} \left| \frac{d\dot{z}}{dx}\Big|_{CM} \cos\theta_{z'} + \omega_{y'} \right| \left(\frac{d\dot{z}}{dx}\Big|_{CM} \cos\theta_{z'} + \omega_{y'} \right) \left(\frac{W}{2} \right)^4 \tag{2.15}$$

where, in this approximation, $\theta_{z'}$ is the angle between the y and y' axes.

2.3.1.5 Motion of an isolated self-gravity wake

Inside the BW the wakes are continously perturbed via out-of-the-plane torques; thus, there is no torque equilibrium. We must integrate the equations of rigid motion:

$$\dot{\omega}_{x'} = \frac{\tau_{x'}}{I_{x'}} + \frac{I_{y'} - I_{z'}}{I_{x'}}\omega_{y'}\omega_{z'} \tag{2.16}$$

$$\dot{\omega}_{y'} = \frac{\tau_{y'}}{I_{y'}} + \frac{I_{z'} - I_{x'}}{I_{y'}}\omega_{z'}\omega_{x'} \tag{2.17}$$

$$\dot{\omega}_{z'} = \frac{\tau_{z'}}{I_{z'}} + \frac{I_{x'} - I_{y'}}{I_{z'}}\omega_{x'}\omega_{y'} \tag{2.18}$$

where $I_{q'}$ is the moment of inertia about the principal axis q'. These equations of motion are numerically integrated with a midpoint method (Press et al., 2007) (note that differential rotation is commutative, so the order of rotation doesn't affect the integration). Note that the inertial terms

$$\tau_{\mathrm{inertia}_k} = (I_i - I_j)\omega_i\omega_j \tag{2.19}$$

(where $i \neq j \neq k$ and $i, j, k = x', y', z'$), are important to understand the wake's rotation since they couple the rotations about the different axis ($\omega_{x'}, \omega_{y'}, \omega_{z'}$).

In Figure 2.8 we describe the rotation of the wakes in the BW, for a maximum slope of $14°$. The top panel shows the change in the wake's ortientation, the middle panel shows the magnitude of the torques, and the bottom panel shows that vertical impact speeds. We see in the bottom panel that the rotation of the wakes generate $>1\mathrm{cm/s}$ vertical impact speeds in the wave region. To calculate Figure 2.8 we relaxed the approximation that $\theta_{x'}$ and $\theta_{y'}$ are small, which amounts to computing all 4 torques symmetrically for the 3 axes. The full form of the torques is in Appendix A.

In order to describe the orientation of the wake in inertial space, we have introduced the angles $(\theta_x, \theta_y, \theta_z)$ (upper panel), which correspond to the wakes' 'pitch', 'roll', and 'yaw', respectively. $\theta_x = \cos^{-1}(\hat{x}' \cdot \hat{z})$ and $\theta_y = \cos^{-1}(\hat{y}' \cdot \hat{z})$ increase as the x' and y' axes, respectively, point towards the vertical direction. $\theta_z = \tan^{-1}(-\hat{y}' \cdot \hat{x}/\hat{y}' \cdot \hat{y})$ is 0 when the y'-axis, projected onto the ring's plane, points at the

azimuthal and it increases counterclockwise. In the specific configurations of the wakes in Figure 2.5, these angles are equivalent to their corresponding primed counterparts. Moreover, if $\theta_{x'}$ and $\theta_{y'}$ are small, then $\theta_{z'} \approx \theta_z$.

In the top panel of Figure 2.8 we show the motion of a wake when the slope of the wave is constant and zero (black line). We find that the wake equilibrates stably at an angle $\theta_z = 25^\circ$. However, when the slope is changing, the orientation of the wake becomes significantly more complex (colored lines in the top panel). The sole difference causing this divergence in behavior is the introduction of a slope via the BW acceleration and shear torques—even if this slope is relatively small ($|dz/dx|_{\max} = \tan 14^\circ$). The dependence on the small slope and the forcing frequency (ω') makes the BW torques (on average) two orders of magnitude smaller than the Keplerian and the tidal torques (middle panel), but the inclinations they cause provoke a non-linear behavior in the angular variables ($\theta_{x'}$,$\theta_{y'}$, $\theta_{z'}$) which are strongly coupled. The coupling mainly comes from the inertial term.

Since the BW torques are small, the inclination of the wake comes from the action of this inertial term, but the inertial term is non-zero only due to the prescence of the BW torques. Therefore, the smallest torques in magnitude, namely the ones introduced by the bending wave, have the biggest effect on the dynamics. The wakes no longer stay on the plane of the ring simply oscillating about an equilibrium orientation; rather, they spin full circles and reach inclination of 80° from the equatorial plane for the case of a maximum slope of 14° (top panel, vertical dashed line).

The bottom panel of Figure 2.8 shows the relative vertical speed between the wake and the ring particles. These are computed as

$$v_{\mathrm{rel};z'} = [\frac{L}{2}(-\omega_{x'} + \frac{dz}{dx}) + \frac{W}{2} * (\omega_{y'} + \frac{dz}{dx})](\hat{z'} \cdot \hat{z}) + \frac{L}{2}\omega_{x'}(\hat{x'} \cdot \hat{z}) \tag{2.20}$$

where the dominant terms are the projections of the rotational speeds onto the z-axis. These speeds occur in the > 1 cm/s; thus, the resuting collisions can potentialy lift ejecta vertically. Nevertheless, we are still to account for the gravitational interactions between self-gravity wakes, which, as we will see, can have a stabilizing effect on the pitch-angle of the wakes.

The relative vertical velocities within the wake and the ring particles associated with this motion are in the cm/s range.

2.3.1.6 Torque due to self-gravity wakes

For the gravitational force that self-gravity wakes exert on each other we consider the case of a wake with variable orientation embedded on a field self-gravity wakes oriented at a constant $\theta_{z'} = \theta_w$. Taking this field as a set of density plane waves, we can use Pringle and Lyden-Bell equations for the torque of a spiral arm on a galaxy (Lynden-Bell & Pringle, 1974), which have been applied to self-gravity wakes in proto-lunar disks in Takeda & Ida (2001). The potential of the spiral arms is given in Binney & Tremaine (2008) in terms of Saturncentric distance r and longitude Θ as:

$$\Phi' = \frac{2\pi G}{|k|}\sigma_w Re[e^{i(m_w\Theta + k_r r)}] \tag{2.21}$$

Where $k = \frac{2\pi}{\lambda_T}$ and m_w and k_r are the azimuthal and radial wavenumbers, and σ_w is the wake surface density minus the mean surface density of the ring. Following the appendix in Takeda & Ida (2001) we relate the wavenumbers by $m_w = kr\sin\theta_w$ and $k_r = k\cos\theta_w$, where $\theta_w = 25°$ is the pitch-angle. To compute σ_w we'll approximate the wake surface density to be $\rho_{\text{Roche}}\int_{-\infty}^{\infty} e^{-(\frac{z}{H/2})^2}dz\rho_{\text{Roche}}\frac{\sqrt{\pi}}{2}H$, noting that the mean surface density σ for the A ring region is about $400\,\text{kg/m}^2$ (Tiscareno et al., 2007) and has a negligible effect on σ_w. We will now expand the potential (Eqn. 2.21) about the center of a wake located at $(r_0, \Theta_0 = y_0/r_0)$ where $y_0 = 0$, similar to what is done in Cook & Franklin (1964). The potential then becomes:

$$\Phi' = \frac{2\pi G}{|k|}(\rho_{\text{Roche}}\frac{\sqrt{\pi}}{2}H)(1 - k^2(\cos\theta_w(r - r_0) + \sin\theta_w y)^2) \tag{2.22}$$

To write the potential in terms of the orientation of the wake $\theta_{z'}$ (in the approximation where $\theta_{x'}$ and $\theta_{y'}$ are small), we consider the distance about the long axis, y', and write $r - r_0 = -y'\sin(\theta_{z'})$ and $y = y'\cos(\theta_{z'})$

This yields the potential

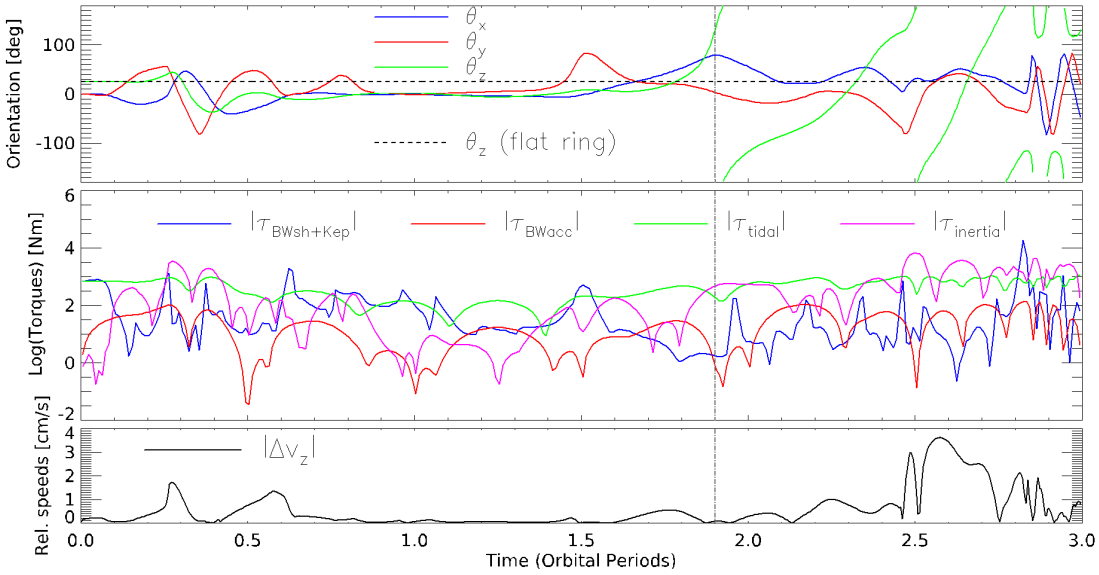

Figure 2.8: Angular motion (top), torques (middle), and speed relative to the ring (bottom) of a uniform density self-gravity wake satellite evolved integrating the equations of rigid motion (equations 2.16, 2.17 and 2.18) and the 3D Hill equations (2.4).$\theta_z = 0$ when the long axis (y'), projected onto the plane, points to the azimuthal, while $\theta_x = 0$ and $\theta_y = 0$ when the x' and y' axes are in the rings' plane and $90°$ when they point in the vertical direction. The wake has uniform density and dimensions $W = 18\,\mathrm{m}$, $L = 232\,\mathrm{m}$ and $H = 4\,\mathrm{m}$, and the coefficient of restitution ϵ of the collisions and the space density ρ_s of the ring particles are set to balance the torques outside of the wave at a pitch-angle is $25°$ (see Figure 2.4 and related discussion). The maximum slope is set to $14°$ and the slope is 0 at $t = 0$, and varies harmonically with the forcing frequency ω' (see Eqn. 2.1). For comparison, we also show the time evolution of the orientation of a wake on a flat ring (black dashed line). (Top) The wake inclines back and forth as the wave passes through, and that its long axis spins around in the plane until it reaches a steady state where the wake oscillates about the azimuthal direction. Marked with a dashed gray line is the point where the motion becomes too extreme, given that $\theta_x = 80°$, and given that the wake points completely in the radial direction. (Middle) The torques associated with the displayed motion. The inertial torque becomes very important, and the BW torque is on average the smallest one by two orders of magnitude. (Bottom) z-component of the relative velocities between the wake and a particle colliding with the edge of the wake.

$$\Phi' = \frac{2\pi G}{|k|}(\rho_{\rm Roche}\frac{\sqrt{\pi}}{2}H)[1 - k^2 y'^2 \cos^2(\theta_{z'} - \theta_w)]$$

We now apply the $-\frac{1}{y'}\frac{\partial}{\partial\theta_{z'}}$ operator to the potential and multiply by the differential mass times the lever arm ($dm * y' = \rho_{\rm Roche} HW dy' * y'$) to get the torque at distance y' from the center of the wake; we then proceed to integrate over y' and get:

$$\tau_{{\rm wake};z'} = \frac{4\pi^2}{\lambda_T} G\rho_{\rm Roche}\frac{\sqrt{\pi}}{2}H^2 W\frac{L^3}{24} * \sin 2(\theta_w - \theta_{z'}) \tag{2.23}$$

Which changes the equation of the torque about the z-axis to:

$$\tau_{z'} = \tau_{{\rm tidal};z'}(\theta_{z'}) + \tau_{{\rm Kep};z'}(\theta_{z'}, \rho_s) + \tau_{{\rm wake};z}(\theta_{z'}) \tag{2.24}$$

The torques in the z-axis now equilibrate at an angle of $\theta_{z'} = 25^\circ$ for $\rho_s = 390\,{\rm kg/m^3}$ for the full Hill equations computation and $\epsilon = 1$. The equilibrium orientation of the wake is now less sensitive to the surrounding space density since the wake potential creates a minimum when wakes align, and may explain why the pitch-angle of the wakes is nearly uniform ($\sim 25^\circ$) over the rings (Jerousek et al., 2016) even if the density and the shear rate vary between the A and the B rings. We are assuming the coherent structure of $\theta_w = 25^\circ$ is kept within the wave, but the wakes may not have a coherent orientation or well-defined wavenumbers, which is suggested by the reduction of the number of coherent gap structure in UVIS occultations to 25% the outside value (Rehnberg et al., 2017) and by our equations of motion which predict that the wakes can spin up or oscillate about the azimuthal; in which case Eqn. (2.23) would be modified by the wakes that are not part of the plane-wave field. While we lack an expression for the case of neighboring wakes with multiple orientations, we will heuristically extend the case of a single misaligned wake embedded in a wake field with orientation θ_w, to the case of a misaligned wake in a the BW region embedded in the oriented wake field of the A-ring. The total wake potential acting on a wake is then given by Eqn. (2.21).

2.3.2 Motion of an embeded self-gravity wake

The relative velocity and orientation of a self-gravity wake embedded on a field of self-gravity wakes with fixed orientation θ_w, evolved under equations (2.16), (2.17), (2.18), is plotted in Figure 2.9.

We see a similar non-linear behavior as the isolated wake (Figure 2.8) resulting in $\mathrm{cm/s}$ collisional speeds (Figure 2.9), but the values of θ_z are more conservative—oscilating about $\theta_z = 0$ and staying below 90° for most of the motion. The restoring force to the equilibrium angle has now increased, and this makes the vertical collisional speeds — which are coupled to $\theta_{z'}$ by the inertial term (Eqn. 2.19) — increase as the wake swings back into position.

The extreme values for the orientation angles, particularly θ_z which at times has the long axis pointing in the radial direction, make us skeptical that the rigidity assumption holds throughout all of the motion. To remedy this we also computed the motion of a wake with long axis $L = 77\,\mathrm{m}$, a third of the usual length. Note that we are not suggesting that self-gravity wakes will shed two thirds of their mass (that would create a much bigger haze signal than the one observed), rather we are verifying that even if a wake were to shed the regolith near its edges while rotating, it will still maintain collisional speeds in the $\mathrm{cm/s}$ range. Hence, the process is not self-limiting, nor does it necessitate a wake of long axis $L = 232\,\mathrm{m}$. The extreme values of the orientation angles also makes us consider the possibility of the release of material due to the rotation itself (e.i rotational disruption). Note that in this scenario, the launched regolith itself will exit the wave at $\mathrm{cm/s}$ speeds, hence contributing to the haze. In the next section we will show that both, the rotational disruption and collisional ejecta scenarios, create a haze with the same observable features.

2.3.3 Haze predicted properties

The relative velocity curves in Figures 2.8 and 2.9 are of the order of $1\,\mathrm{cm/s}$. Microgravity experiments have shown that at $\mathrm{cm/s}$ velocities we begin to see ejecta in particle collisions with simulant regolith aggregates (Brisset et al., 2018). The $\mathrm{cm/s}$ range is also important because the characteristic vertical speeds of the Mimas 5:3 BW are in the $\mathrm{cm/s}$ range: a $\mathrm{cm/s}$ change in velocity is necessary to have particles reset their motion into trajectories that are no longer in phase with the wave.

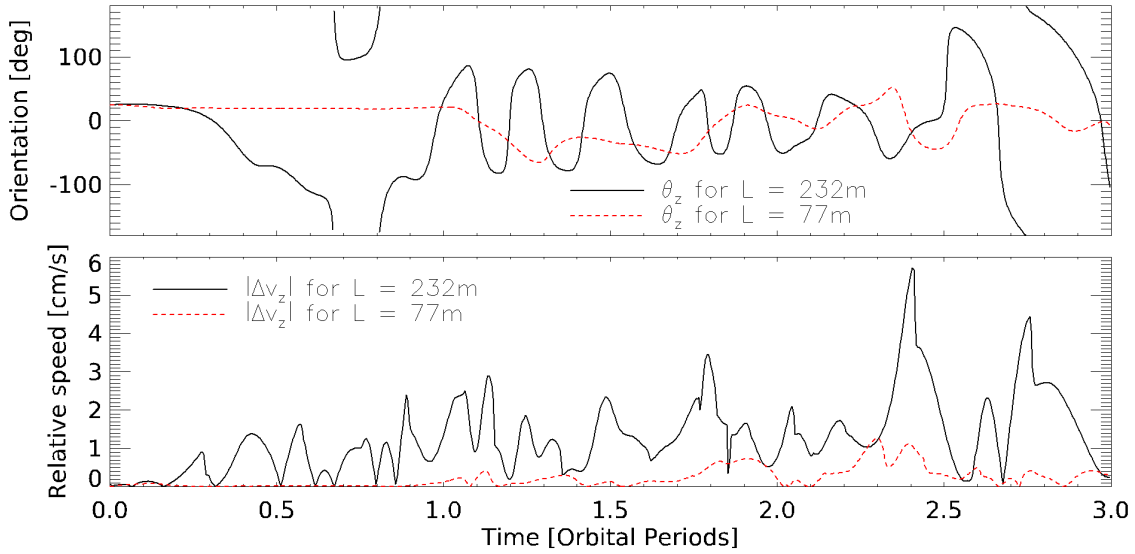

Figure 2.9: Time evolution of the average velocities of particle collisions with self-gravity wakes within the bending wave; motion evolved as in Figure 2.8 with the addition of the wake potential. The maximum slope is set to 14° and $t = 0$ when the slope is 0; the slope varies harmonically with the vertical frequency. Adding the wake potential increases the maximum relative velocity between the wakes and ring particles. For the case of $L = 232\,\mathrm{m}$ we see vertical velocities well within the $\mathrm{cm/s}$ range, while the $L = 77\,\mathrm{m}$ case peaks at about $1\,\mathrm{cm/s}$.

If these collisional speeds increase with slope amplitude, the amount of released material would change with radial position. Figure 2.10 shows precisely this: the peaks of the relative speed over a period have a monotonically increasing trend with the amplitude of the slope of the wave. To determine how the amount of material changes due to this increase in the velocities, we apply a square-root regression to Figure 2.10 and find that:

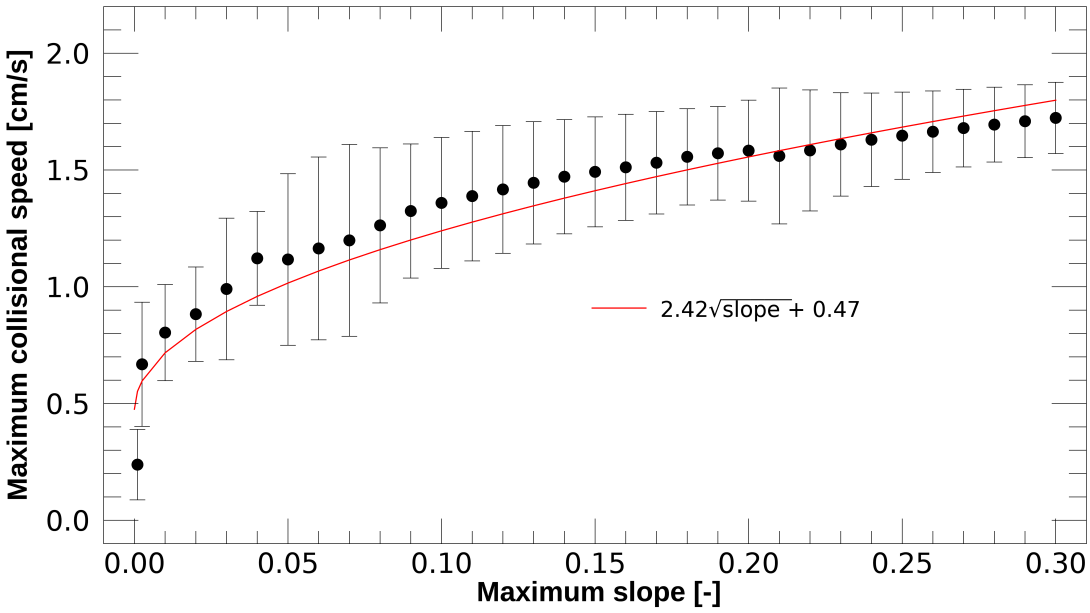

Figure 2.10: Average maximum relative speed of self-gravity wakes for different slopes. The average is taken over a range of initial conditions to show that the increase of collisional speed with the slope is robust to initial conditions. At each value of the slope considered, we start the out-of-phase (at an angle with the ring) by 0, ± 10, ± 20, and ± 30 degrees, at 15 equidistant points in the wave's vertical motion, and run the simulation for 1 period. Therefore, each point is an ensemble average of 105 runs, where the error bars represent the 1σ of the distributions. We see a clear trend: the bigger the slope amplitude of the bending wave the bigger the velocity of the collisions between the wakes and the ring particles. We model this increase with a square-root law.

$$v_{\mathrm{rel};z} = a\sqrt{\left|\frac{dz}{dx}\right|_{\max}} + f \tag{2.25}$$

where $a = 2.42\,\mathrm{cm/s}$ and $f = 0.47\,\mathrm{cm/s}$.

Microgravity experiments show the existence of a speed threshold before which the collisions don't

lift ejecta (Brisset et al., 2018). Once this minimum threshold has been passed, numerical simulation of collisions in free space (Stewart & Leinhardt, 2009) and drop tower experiments (Colwell et al., 2008) suggest that the amount of ejected regolith increases linearly with the specific inelastic energy of the impactor; we represent this by the equation:

$$N_{\rm haze} \propto \mathcal{H}(v_{\rm impact} - g) \cdot (v_{\rm impact} - g)^2 \tag{2.26}$$

where $N_{\rm haze}$ is the number of haze particles liberated per wake, g is the impact speed threshold, and $\mathcal{H}$ is the Heaviside function whose value is 0 if the argument is negative, 1 otherwise.

We don't know where this threshold is for the case of wakes in the rings, but it must be higher than the dispersion velocity ($\sim \Omega z_0 = 0.13\,{\rm cm/s}$), since this doesn't generate sub-mm ejecta outside of the BW (Table 2.1). From now on we heuristically assume that $g = f$ so that the N is proportional to the slope amplitude. Misestimating the value for g by a factor of 2 would change the quantity of haze produced at low slopes (<0.03) by a factor of ~ 4; however, more than 90% of the wave lies in the high-speed regime where the square-root trend works well. Given this value of g, and assuming a set number of wakes per area, the amount of haze particles per area (Σ) has the proportionality of:

$$\Sigma_{\rm haze} \propto \left|\frac{dz}{dx}\right|_{\rm max} \tag{2.27}$$

Note that the number density of the haze $n_{\rm haze}(r)$ is given by $\frac{\Sigma_{\rm haze}(r)}{D(r)}$ where $D(r)$ is the vertical thickness of the haze. Combining equations (2.25) and (2.27) and the equation for the differential optical depth $d\tau_{\rm haze}(r) = n_{\rm haze}\bar{\sigma}_{\rm haze}dl$, where $\bar{\sigma}_{\rm haze}$ is the typical cross-section of particles in the haze and dl is a differential path-length through the haze, we arrive at the relation:

$$d\tau_{\rm haze}(r) = \frac{\beta}{D}\left|\frac{dz}{dx}\right|_{\rm max} dl \tag{2.28}$$

where $\beta = \Sigma_0\bar{\sigma}_{\rm haze}$ is the normal optical depth of the haze when the slope is unity, and a free parameter in our model; Σ_0 is the surface density generated by a slope of unity.

For the case of rotational disruption, we take the number of released haze particles per wake to be

proportional to the centrifugal force due to the rotation: $N_{\rm haze} \propto \omega_{x'}^2 r_p$ where $\omega_{x'}$ is the angular speed and r_p is the radial distance from the CM. Note that the angular speed and $v_{{\rm rel};z}$ are related by $\omega_{x'} \approx v_{{\rm rel};z}/r_p$; combining this with equation (2.25), we again arrive at equation (2.28). Therefore, given our rigid model for self-gravity wakes, we predict that in the BW region the extra optical depth must be proportional to the maximum slope of the wave. Note that β is a dimensionless absorption per slope coefficient related to the ejecta-generating efficiency of rotation or collisions.

To construct the geometry of the haze we consider the trajectories of the particles after the collision with the self-gravity wake. Given that in Figure 2.9 $>1\,{\rm cm/s}$ collisional speeds are achieved at many points during a period, we consider that the collisions with the self-gravity wakes are equally likely to occur at any point in the vertical motion of the particles, and that the imparted velocity is in equal proportions, radial and vertical, with a magnitude of $a\sqrt{|\frac{dz}{dx}|_{\rm max}} + f$ where a and f are defined in Eqn. (2.25). The subsequent trajectories can be easily computed by taking the CM of the collision to be the center of the self-gravity wake. Let $V_{\rm CM}$ be the velocity of the CM, then the outgoing speed will be given by

$$v_0 = V_{\rm CM}(1+\epsilon) \pm \epsilon(a\sqrt{\left|\frac{dz}{dx}\right|_{\rm max}} + f) \tag{2.29}$$

the case of $\epsilon = 1$ representing the outgoing speed for the rotational disruption scenario. Relative to a particle in the wave the ejected particles move vertically with a Doppler shifted frequency of $\mu_v \pm k_b v_{0_x}$, where μ_v is the vertical frequency of the particle and k_b is the wavenumber of the BW. The subsequent trajectories are shown in the left panel of Figure 2.11. In the right panel of Figure 2.11 we show the envelope these trajectories form over the radial extent of the wave; note that the thickness of the haze varies radially and is greater at the peaks and troughs than at the equatorial plane. Moreover, the the haze's thickness varies with ϵ, and we find it to range from $90 - 190\,{\rm m}$ for $\epsilon = 0.1 - 1$.

While there's still some phase dependence in the displayed geometry, the dynamics predict the same number of particles at any given phase for a given radial location r. Hence the change in the optical depth profile of a normal occultation can only come from the change of scattered particles in the collisions, which is related to the change in the slope amplitude with r. We then predict that the phase should not appear

in the haze signal, which is a desired feature of the model, given that the observed signal of $B_{\text{eff}} \cong 90°$ occultations show no correlation with the phase of the wave.

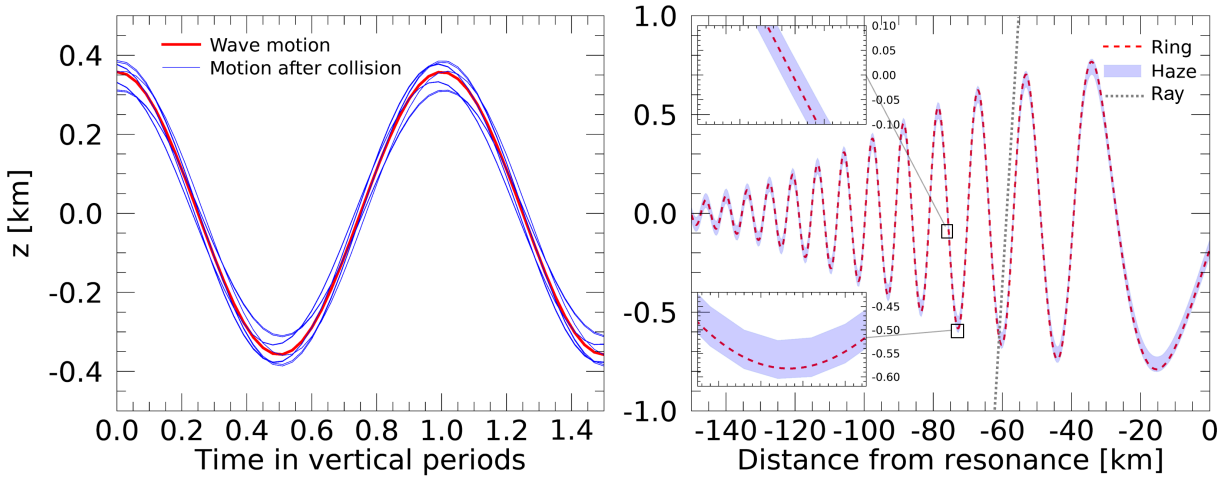

Figure 2.11: Left panel: trajectories in time of the vertical position of haze particles (blue) and the oscillating ring (red) at $-100\,\text{km}$ from resonance. Here the trajectories of haze particles start every phase interval of $\frac{\pi}{3}$ during the up-and-down motion (so we are modeling 6 collisions per period). The ring has a continuous envelope of particles during the period. Right panel: The envelope created in space by the trajectories of particles post-collision using $\epsilon = 0.5$. By looking at the lower left insert panel one can see the slight variation of in the the vertical thickness present in the haze profile; the thickness of the haze changes from 113 to 134 m in the overall plot, and the variations in the zoom-in panel are only of $4\,\text{m}$ (less than a thick mark). A light-ray has been plotted in dashed gray to visualize the geometry of the occultations.

2.4 Transmission Model and Data Reduction

The transmission of light through the rings is modeled by the radiative transfer equation simplified by the fact that the opacity κ of the ring particles is insensitive to wavelength. Moreover, we are working exclusively in the $110 - 190\,\text{nm}$ spectral bandpass of the High Speed Photometer (HSP) within UVIS and, given the lower limit in the $100\,\mu\text{m}$ range for the particle size in the A-ring (Harbison et al., 2013), there is no scattering. Thus, we are firmly within the geometrical optics limit. As a consequence of this the intensity I measured by UVIS is simply:

$$I(r) = I_0 e^{-\frac{\tau_n}{\mu}} + b \tag{2.30}$$

where I_0 is the unocculted star signal, b is background light entering the detector that does not come from

the star, τ_n is the normal optical depth, and $\mu = \sin(B)$ where B is the angle between the ring plane and the light ray. Or, in terms of the transparency T

$$T = \frac{I - b}{I_0} \tag{2.31}$$

We will extract the observed optical depth by using:

$$\ln \frac{I(r) - b}{I_0} = -\frac{\tau_n}{\mu} \tag{2.32}$$

In order to isolate the star signal we determine the background signal (b) and the unocculted star signal (I_0) following the methods of Colwell et al. (2010). It is known that the detector becomes more sensitive over time when the optical depth is close to 0 (Colwell et al., 2010), which introduces a systematic uncertainty on our measurements of I_0 that we are not considering here. Since I_0 refers to the star, in order to eliminate this reference and focus on the properties of the rings themselves, we work with the transparency (T) and the optical depth (τ).

To the 217 occultations of the bending wave region we apply a signal-to-noise filter, or conversely a $\tau_{\max}$ filter (Colwell et al., 2010) of $\tau_{\max} > 1.5$ so that the variations in τ due to the bending wave are distinguishable; this reduces the set of occultations to 130 (see Appendix A for the complete list). From this we select 60 occultations with the following criteria:

First, we maximize the range of geometries probed by our study without oversampling any particular geometry. For this purpose six subsets are created where B can be low angle, 0° to 30°, intermediate angle, 30° to 60°, or normal, 60° to 90°. On the other hand, ϕ can be radial ($|\cos\phi| > \frac{1}{2}$) or azimuthal ($|\cos\phi| < \frac{1}{2}$). We use $|\cos\phi|$ to partition the data because it is the physically relevant quantity that appears in all the models that will be tested. The smallest subset, being the low B radial set, has a total of 10 occultations in the entire dataset, so all other subsets must also contain 10 occultations to not oversample any geometry, yielding 60 occultations in total.

Secondly, in the subsets with more than 10 occultations we select the highest $\tau_{\max}$ occultation for each star, and if there are fewer than 10 unique stars we select the next highest $\tau_{\max}$ for each star until 10

are reached. The final dataset is shown in Table 2.2.

Additional critical geometric parameters consist of the longitude of the occultation in the rings relative to the moon Mimas, the vertical position of Mimas, and the vertical velocity of Mimas. These parameters were determined using the Navigation and Ancillary Information Facility (NAIF) SPICE toolkit (Acton, 1996; Acton et al., 2018). These parameters generally depend on the precise determination of Saturn's pole, the ring plane radius being the most uncertain parameter with errors of $< 10\,\mathrm{km}$ for every occultation. Errors in B and ϕ are generally less than 1°. Knowing the position and velocity of Mimas enables us to compute the phase of the wave using equation 47a in SCL:

$$\Phi_{\mathrm{theory}} = (4\Omega_M + \mu_M)t - 4\Theta - \frac{\pi}{4} \tag{2.33}$$

where Ω_M and μ_M are the Keplerian and vertical frequencies of Mimas and Θ is the azimuthal position of the occultation ($t = 0$ at the ascending node of Mimas). The gravitational moments used to determine the frequencies were taken from Iess et al. (2019), while the other physical parameters of Saturn and Mimas (mass, semi-major axis of Mimas, and inclination of Mimas) were taken from Jet Propulsion Laboratory Horizons database (Jacobson, 2010); these are presented in table 2.3. We find a theoretical value for the 5:3 vertical resonance location of $r_v = 131902\,\mathrm{km}$ and a wave amplitude of $A_v = \frac{472\mathrm{m}}{\sqrt{\sigma_{100}}}$ where σ_{100} is the surface mass density in $100\,\mathrm{g/cm^2}$.

An alternative way of computing the phase is through observations. From the position of the optical depth peaks and troughs in the data a phase can be determined by fixing Gresh et al. (1986)'s best-fit parameters of the SCL model—surface density σ and viscosity ν—while letting the phase vary and applying a χ^2 minimization scheme. This data-driven value for the phase is reported in Table 2.2 as Φ_{obs}.

2.5 Ray-tracing model

The relationship between the slope of the wave and the extinction of starlight in a UV occultation is non-linear, both in the SCL model and in our model. In SCL the shape of the wave enters into the optical depth by determining the limits of the optical depth path integral.

Occultation	B [deg]	ϕ [deg]	$B_{\rm eff}$ [deg]	Lon. [deg]	Z	sign($\dot{Z}$)	$\Phi_{\rm theory}$[deg]	$\Phi_{\rm obs}$[deg]	b	I_0	$\tau_{\rm max}$
$B > 60^\circ$ and $\lvert\cos\phi\rvert > \frac{1}{2}$						Complete subset size = 10 occultations					
AlpCru(100)I	68.2	154.5	70.1	213.6	-5016.5	1	100	-	0.50	434.18	6.0
AlpCru(92)I	68.2	169.6	68.5	114.7	-4232.1	1	160	-	0.50	518.56	6.3
EpsCas(104)I	-70	187.8	70.1	152.8	-2034.7	-1	87	-	0.04	4.59	3.8
BetCru(98)I	65.2	192.7	65.7	319	3954.6	-1	248	-	0.23	274.05	7.1
BetCen(104)I	66.7	209.3	69.4	321	-1126.9	-1	303	-	0.31	357.50	6.7
BetCen(105)I	66.7	212.9	70.1	83.1	5023	1	62	-	0.15	313.44	5.2
BetCen(78)E	66.7	45.9	73.3	206.5	-5087.4	-1	295	-	0.38	564.08	7.0
BetCen(77)E	66.7	47.5	73.8	12.6	4961	1	161	-	0.34	593.24	7.4
BetCen(92)E	66.7	55	76.2	75.5	4143.3	-1	318	-	0.23	452.62	6.2
EpsCas(104)E	-70	122.3	79	123.6	-4468.4	1	299	-	0.04	4.56	3.6
$B > 60^\circ$ and $\lvert\cos\phi\rvert < \frac{1}{2}$						Complete subset size = 17 occultation					
BetCen(77)I	66.7	270.4	89.8	257.3	-1823.4	1	164	-	0.25	587.23	7.7
BetCen(85)I	66.7	277.5	86.8	41.8	-4526.9	-1	210	-	0.71	1066.32	7.6
BetCen(89)I	66.7	278	86.6	322.8	-572.3	1	277	-	0.33	498.23	7.7
AlpCru(100)E	68.2	93.9	88.5	188.8	807.8	1	288	-	0.50	428.76	5.8
BetCen(102)I	66.7	249.1	81.3	0.9	4984.3	-1	53	-	0.33	370.17	7.3
BetCen(104)E	66.7	105.5	83.5	299.7	-3402.1	1	154	-	0.29	342.97	8.6
BetCru(262)I	65.2	257.3	84.2	18	5014.2	-1	343	-	0.19	109.53	6.4
BetCru(253)I	65.2	255.6	83.4	187.3	-4002.7	-1	157	-	0.20	106.17	6.5
GamCas(100)E	-66.3	72.5	82.5	93.5	-3408.3	1	259	-	0.09	54.16	6.1
GamAra(37)I	61	248.7	78.6	62.1	4684.1	1	133	-	0.12	53.50	4.2
$60^\circ > B > 30^\circ$ and $\lvert\cos\phi\rvert > \frac{1}{2}$						Complete subset size = 35 occultations					
EpsCen(65)I	59.6	226.6	68.1	343.1	-1573.5	-1	220	143	0.26	259.43	6.6
ZetCen(60)I	53.6	228.1	63.8	258.7	-4185.7	-1	235	119	0.23	214.36	6.6
DelCen(98)I	55.6	211.3	59.6	54.8	402.3	1	100	16	0.09	34.47	5.8
EpsLup(36)E	51	44.9	60.2	135.3	2840.1	-1	99	125	0.14	65.34	5.7
GamLup(32)E	47.4	33.8	52.6	158.4	5097.4	1	310	333	0.15	145.17	5.4
LamSco(29)E	41.7	148.3	46.3	222.1	-4753.7	-1	35	9	0.32	567.90	4.6
ZetPup(171)I	38.6	202.1	40.8	120.2	2022.7	-1	350	23	0.12	49.51	4.3
EtaLup(34)E	44.5	357.1	44.5	90	-3167.9	-1	353	44	0.17	93.96	4.2
TheAra(40)E	53.9	28.6	57.3	197.2	-2036.3	-1	269	218	0.09	24.98	4.1
KapCen(42)I	48.5	168.5	49.1	237.3	228.4	1	88	62	0.24	82.26	4.1
$60^\circ > B > 30^\circ$ and $\lvert\cos\phi\rvert < \frac{1}{2}$						Complete subset size = 37 occultations					
ZetCen(112)I	53.6	239.7	69.6	112.5	4393.8	-1	345	216	0.03	37.31	6.4
AlpAra(32)I	54.4	277.9	84.4	258.6	3837.8	-1	311	311	0.15	76.61	6.1
KapCen(35)E	48.5	85.5	86.1	302.8	-5074.8	1	279	305	0.12	92.03	5.8
TheCar(190)I	-43.3	252.4	72.2	219.3	-4463.7	1	276	276	0.16	25.33	5.7
ZetCen(62)E	53.6	70.1	75.9	8.9	-4066	1	46	85	0.19	212.18	5.5
TheAra(41)E	53.9	82.4	84.5	205.4	1720.2	-1	193	193	0.09	23.52	5.5
DelCen(64)E	55.6	110.6	76.4	194.3	4773.2	1	327	353	0.09	52.91	5.0
KapCen(36)I	48.5	241.2	67	228.6	-2480.8	-1	329	200	0.24	88.26	5.0
DelPer(37)I	-54	264.5	86	145.7	4558.5	-1	28	28	0.08	27.26	5.0
AlpLup(248)E	53.9	111.4	75.1	73.2	4024.3	-1	150	175	0.22	16.97	4.8

Table 2

Occultation	B [deg]	ϕ [deg]	$B_{\rm eff}$ [deg]	Lon. [deg]	Z	sign($\dot{Z}$)	$\Phi_{\rm theory}$[deg]	$\Phi_{\rm obs}$[deg]	b	I_0	$\tau_{\rm max}$
$B < 30^\circ$ and $\lvert\cos\phi\rvert > \frac{1}{2}$	Complete subset size = 11 occultations										
GamPeg(172)I	-20.3	36.7	24.7	283.4	4683.3	1	328	339	0.01	11.49	1.7
AlpCMa(274)E*	13.5	40.4	17.5	188.9	2833.2	-1	245	232	0.07	23.75	1.7
SigSgr(114)I	29.1	330.2	32.6	262.3	-492.7	1	160	133	0.04	33.50	2.7
AlpVir(34)E	17.3	332.9	19.2	259.5	2584	1	207	220	0.50	979.08	1.7
GamPeg(32)I	-20.3	138.6	26.2	226.6	2857.3	1	342	342	0.53	149.51	1.8
AlpVir(8)I	17.3	141.1	21.8	162.3	4488.6	-1	144	221	5.00	1000.46	1.8
KapCMa(168)I	29.3	175.9	29.4	268.8	-3886.5	1	270	321	0.04	6.06	1.7
BetCMa(211)I#	14.2	223.4	19.2	67.1	-3637.3	1	1	232	0.05	43.52	1.8
EpsCMa(276)E	26	50.6	37.5	217.7	4192	-1	108	173	0.12	69.53	2.6
AlpVir(210)I#	17.3	311.5	25.1	46	-4015.8	1	259	104	0.04	138.22	2.5
$B < 30^\circ$ and $\lvert\cos\phi\rvert < \frac{1}{2}$	Complete subset size = 20 occultations										
DelSco(236)I	28.7	263.2	77.9	10.8	-5022.7	-1	171	168	0.65	22.98	2.8
AlpVir(232)E	17.3	89.3	87.8	316.7	-2068.6	1	284	284	0.46	125.75	2.3
AlpVir(34)I	17.3	232.8	27.2	24	579.6	1	225	186	0.29	1021.26	2.2
SigSgr(244)I	29.1	269.3	88.8	86.6	-1341.1	1	313	313	0.04	16.60	2.1
GamPeg(36)E	-20.3	66.8	43.2	343.5	3206.1	1	59	34	0.45	141.95	1.8
GamPeg(211)E	-20.3	122.5	34.6	207.2	518.8	-1	200	200	0.02	13.19	1.8
AlpVir(211)I	17.3	267.2	81.2	103.3	-2632.7	1	230	269	0.47	132.50	1.8
AlpVir(8)E	17.3	91.3	85.9	197.2	3679.9	-1	19	45	5.00	1053.60	1.7
KapCMa(168)E	29.3	127.3	42.8	286.8	-1613.5	1	229	284	0.04	6.19	1.7
AlpCMa(281)I*	13.5	230.1	20.5	144.3	3652.3	1	143	195	0.06	27.91	1.7

Table 2 (continued): Dataset for this work. We divided the UVIS data set into 6 subsets comprising different geometries, each containing 10 occultations. The theoretical phases of the waves were computed using equation (2.33) and the latest SPICE kernel for the longitude of the occultation relative to Mimas (the 'Lon' column). The observed phases were computed by fitting the phase of the wave in each occultation individually with fixed global parameters (β, ν, σ). Z and $\dot{\rm Z}$ are the vertical position of Mimas with respect to the equator and the sign of its velocity respectively, both are required to compute the phase of the wave. "#" indicates that the difference between the theoretical and predicted phase is more than 90°. "$*$" indicates that the dispersion relation, or the predicted distances between peaks of optical depth, are inconsistent with the data for these occultations.

	$GM\,[\frac{\rm km^3}{\rm s^2}]$	$a\,[\rm km]$	$i\,[\rm deg]$
Mimas	2.50349	185539	1.574
Saturn	37931206.2	-	-

Table 2.3: Physical parameters of Mimas and Saturn used in this work. Taken from the JPL Horizons database (accessed in November 2019).

$$\tau = \int_{l_1}^{l_2} n\bar{\sigma}_{\rm ring} dl \tag{2.34}$$

where n is the number density along the lightray, $\bar{\sigma}_{\rm ring}$ is the average cross-section of absorbers over the path of the light ray, and l_1 and l_2 are the ring's entry and exit points along the light ray.

Since we use SCL theory to trace the wave profile, $\bar{\sigma}_{\rm ring}$, n, and the thickness of the ring d are uniform throughout the wave (Shu et al., 1983; Gresh et al., 1986). The predicted haze is formed by relatively small particles (see Table 2.1) and hence keeping n uniform is compatible with the haze. A quick calculation shows that if the haze particles are an order of magnitude smaller than the ring's they will constitute be 1% of the mass at the peak of the haze's optical depth. This allows us to write the product $n\bar{\sigma}_{\rm ring}$ in terms of the normal optical depth outside of the wave τ_{n0}. Consider an occultation along the wave where the light comes only from the direction normal to the plane, then

$$\tau_{n0} = \int_0^d n\bar{\sigma}_{\rm ring} dz = n\bar{\sigma}_{\rm ring} d \tag{2.35}$$

$$n\bar{\sigma}_{\rm ring} = \frac{\tau_{n0}}{d} \tag{2.36}$$

So we can write

$$\tau = \int_{l_1}^{l_2} \frac{\tau_{n0}}{d} dl \tag{2.37}$$

In order to better match the Voyager I radio occultation, Gresh et al. (1986) introduces a Gaussian enhacement to the optical depth without a physical motivation for producing such an enhacement. We showed in section §2.3 that a haze (Eqn. 2.28) is generated as a consequence of the rotation of self-gravity wakes within the BW; adding this haze to Eqn. (2.34) we get:

$$\tau = \int_{l_1}^{l_2} \frac{\tau_{n0}}{d} dl + \int_{l_3}^{l_4} \frac{\beta}{D} \left|\frac{dz}{dx}\right|_{\rm max} dl \tag{2.38}$$

where l_3 and l_4 are the entry and exit points of the haze along the lightray, β is related to the number of particles released by the wakes (see section §2.3) and D is the vertical thickness of the haze. $\left|\frac{dz}{dx}\right|_{\rm max}$ is the

maximum slope over a period at a given radial coordinate x. To simplify equation (2.38) we make use of the azimuthal and north-south symmetry of the rings which makes the integrals depend only on the radial coordinate x. Then, if B is the angle between the rings and the light ray and ϕ is the angle between the radial direction and the lightray (projected into the ring's mean plane), we can write:

$$dl = \frac{dx}{\cos B \cos \phi} \tag{2.39}$$

We know the cross-section $\bar{\sigma}_{\rm ring}$ and the column density $n_{\rm ring}$ are not isotropic however, due to self-gravity wakes having a consistent average orientation (Colwell et al., 2006). Thus, the normal optical depth obtained by simply multiplying the oblique optical depth by $\sin B$ is not the true normal optical depth defined in Eqn. (2.35). Nevertheless, it isn't the goal of our model to describe the dependence of $\bar{\sigma}_{\rm ring}$ or $n_{\rm ring}$ on the geometry of the occultation, but only to explain the variation of the optical depth in the wave with respect to the optical depth outside the wave region. Thus, we define the background slanted optical depth as:

$$\tau_0 = \frac{\tau_{n0}}{\sin B} = \frac{n \bar{\sigma}_{\rm ring} d}{\sin B} \tag{2.40}$$

where τ_0 is determined by averaging values for the optical depth between $r = 131600\,\mathrm{km}$ and $r = 131700\,\mathrm{km}$, a region just outside of the wave.

By substituting Eqns. (2.39) and (2.40) into Eqn. (2.38) we get the equation for the predicted optical depth in terms:

$$\tau = \int_{r_1}^{r_2} \frac{\tau_0}{d} \sin B \frac{dx}{\cos B \cos \phi} + \int_{r_4}^{r_3} \frac{\beta}{D} \left| \frac{dz}{dx} \right|_{\rm max} \frac{dx}{\cos B \cos \phi} \tag{2.41}$$

where the limits of integration r_1, r_2 and r_3, r_4 are the radial coordinates of the entry and exit points of the light ray as it crosses the ring and the haze respectively. These radial coordinates are computed by numerically finding the intersection of the trajectories of incoming photons,

$$z_{\rm photon} = \sin B \frac{x_{\rm photon} - x_0}{\cos B \cos \phi},$$

with the curves $h(x_V) \pm \frac{d}{2}$ (for r_1 and r_2) and the curves delimiting the upper and lower boundary of the haze depicted by the blue fill in Figure 2.11 (for r_3 and r_4). Here $h(x_V)$ is the wave profile derived in SCL (see Eqn. (2.2)). To visualize the ray-tracing, consider the light-ray (dashed gray line) shown in Figure 2.11. The haze's shape cannot be written in closed form; therefore, in order to trace its upper and lower boundaries we run the numerical procedure described in section §2.3.3 for each occultation.

Contrasting with Gresh et al. (1986)'s second integral in Eqn. (2.41), their Gaussian enhacement has three free parameters that vary independently: width, amplitude, and position. In our case we have one free-parameter for the haze $\beta = \Sigma\sigma_{\rm haze}$, which is related to the number of particles released by the wake as they rotate and collide with neighboring particles (see §2.3.3); all the spatial information of the haze—shape, width, and position—is fixed by the wave profile h (Eqn. 2.2) which is also heaviliy constrained by the first integral in equation (2.41). In Gresh et al. (1986) the combinations of angles $\frac{\tan B}{\cos\phi}$ lead to the definition of the angle $\tan B_{\rm eff} = \frac{\tan B}{\cos\phi}$. Because this combination does not occur in the second term in equation (2.41), we prefer to leave the angle ϕ explicit.

The shape of the wave itself is a function of the surface mass density σ, the viscosity ν, and the thickness d which are free parameters. New to our model is free-parameter β. The quantity to be compared to the data is the transparency, which is the normalized stellar counting rate after background subtraction:

$$T_{\rm model} = e^{-\tau} = \exp\left(-\int_{r_1}^{r_2} \frac{\tau_0}{d} \sin B \frac{dx}{\cos B \cos\phi} - \int_{r_4}^{r_3} \frac{\beta}{D} \left|\frac{dh}{dx}\right|_{\rm max} \frac{dx}{\cos B \cos\phi}\right) \tag{2.42}$$

Note that while the thickness d appears directly in the above expression it does not figure as a relevant predictor in our model. As Gresh et al. (1986) discovered, the effects of increasing d on these ray-tracing simulations of bending waves are equivalent to increasing the resolution of the simulation. The optical depth profile becomes smoother in both cases because there are more data points probing the slopes of the ring. Any difference between a thickness of 10 m to 100 m in the rings would not make a difference in a dataset that is fixed at a resolution of $400\,$m. Since the BW occultations at these resolutions can't be used to determine the thickness of the rings directly, we can fix the value of d for all runs, which we choose to be $15\,$m. Similarly, the thickness of the haze, which determines the limits of the second integral in Eqn.

(2.42), is derived from the dynamics in section §2.3 and also has values under the resolution of our data so by the same argument we choose to fix ϵ (the coefficient of restitution which determines the thickness of the haze) at two values, 0.5 and 1. We are then left with three free parameters: the viscosity ν, the surface mass density σ, and the particles released by the wakes per area times their cross-section β.

Note that by taking β to be a constant for all occultations we assume that the product $n_{\rm haze}\sigma_{\rm haze}$ does not depend on the azimuthal viewing angle ϕ. This becomes important in the next section as we compare. Eqn. (2.42) against the data.

2.6 Comparison with data

The ray-tracing code is used to compute the path integrals in equation (2.42) for 500 lightrays which are drawn at a radial separation of $400\,\mathrm{m}$ each, covering a radial distance of $200\,\mathrm{km}$ in the wave region, hence matching the resolution of the data set (the expection to this is EpsCas104E, for which which had one null value in the data set, which was likewise emulated in the simulation). We use a reduced χ^2 minimization method where we find the best parameter values by comparing the model with the 60 occultations shown in table 2.2. The reduced χ^2 is given by:

$$\chi^2_R = \frac{1}{D_f}\Sigma\left(\frac{T - T_{\rm model}}{\Delta}\right)^2 \tag{2.43}$$

where $\Delta = \frac{\sqrt{I-b}}{I_o}$ and D_f is the degrees of freedom. The uncertainty of I_0 and b is negligible due to the small value of b and the amount of data points used to compute them both. $T_{\rm model}$ is given by equations (2.42), and T is given by equation (2.31). The wave profile predicted by SCL theory has been modified to include a haze of particles whose shape is computed using the particles' velocity (Eqn. 2.29) and number density (Eqn. 2.28) with β as a free parameter. The total free parameters of our model are β, the surface density σ, and the viscosity ν, while the thickness of the ring d and the coefficient of restitution ϵ have been fixed at values $d = 15\,\mathrm{m}$ and $\epsilon = 0.5$ and 1.

The best-fit parameters for the haze model and the SCL model (no haze), are in table 2.4. Figures 2.12 and 2.13 plot the best-fit optical depth profile for the haze (black line) and SCL (dashed green line)

models for 7 occultations.

Table 2.4 shows that the models with the haze ($\beta \neq 0$) fit significantly better than the SCL model for low $B_{\rm eff}$ occultations. The same can be seen Figure 2.12: the unmodified SCL (dashed green line) has a significantly lower explanatory power for the dataset (red line). Most notably, Figure 2.12 shows that the throughs of the optical depth pattern now conincide with the predicted optical depth due to the Gaussian-like enhacement produced by the haze. Moreover, the bases of the peaks are broader than those of SCL theory and resemble the observed shape of the optical depth profile. The broadening of the peaks' bases is caused by the thickening of the haze at the minima and maxima of the wave (which are evident in Figure 2.11). The damping length due to the $\nu = 576\,\mathrm{cm}^2/\mathrm{s}$ viscosity matches the observed length of the wave. An additional effect of this high viscosity is to increase the predicted value for the slope of the wave which is 17° for our best-fit model.

Table 2.4 shows that using the observed phase instead of the theoretical phase improves the fit, but it does not change our values for β, ν, and σ significantly. Likewise, changing the coefficient of restitution, which changes the thickness of the haze (see Figure 2.11), does not alter the agreement with the data.

In Figure 2.13 we present 6 occultations, once for each of the data subsets in Table 2.2. The occultatios range from higher to lower B from left to right in the figure. Our model represents a significant improvement over SCL for both radial (lower row) and azimuthal (upper tow) occultations. For higher $B_{\rm eff}$ occultations, the SCL theory predicts little change in the optical depth, while the haze model produces the shape of the optical-depth enhacement seen in the data. Nevertheless, we see in the top row that the scaling with B for the haze optical depth, which is simply $1/\sin B$ in our model, fails to reproduce exactly the intensity

Model	Phase	$\epsilon\,[-]$	$\chi^2_R\,[-]$	$\sigma\,[\frac{\mathrm{g}}{\mathrm{cm}^2}]$	$\nu\,[\frac{\mathrm{cm}^2}{\mathrm{s}}]$	$\beta\,[-]$
SCL	$\Phi_{\rm theory}$	$-$	22.15	36.4 ± 5	3540 ± 40	$-$
Haze	$\Phi_{\rm theory}$	1	5.56	37.0 ± 0.4	623 ± 3	1.48
Haze	$\Phi_{\rm obs}$	1	4.46	36.7 ± 0.3	576 ± 3	1.39
Haze	$\Phi_{\rm obs}$	0.5	4.48	36.6 ± 0.3	576 ± 3	1.37

Table 2.4: Best fit parameters for the SCL and haze models. There is a significant improvement in the fit of the haze model over the SCL model. Error bars show the 1σ of the likelihood given by $e^{-\chi^2/2}$. The haze model has 3 free parameters, so all have $D_f = 29819$ degrees of freedom. SCL has 2 free-paramters and hence $D_f = 29879$.

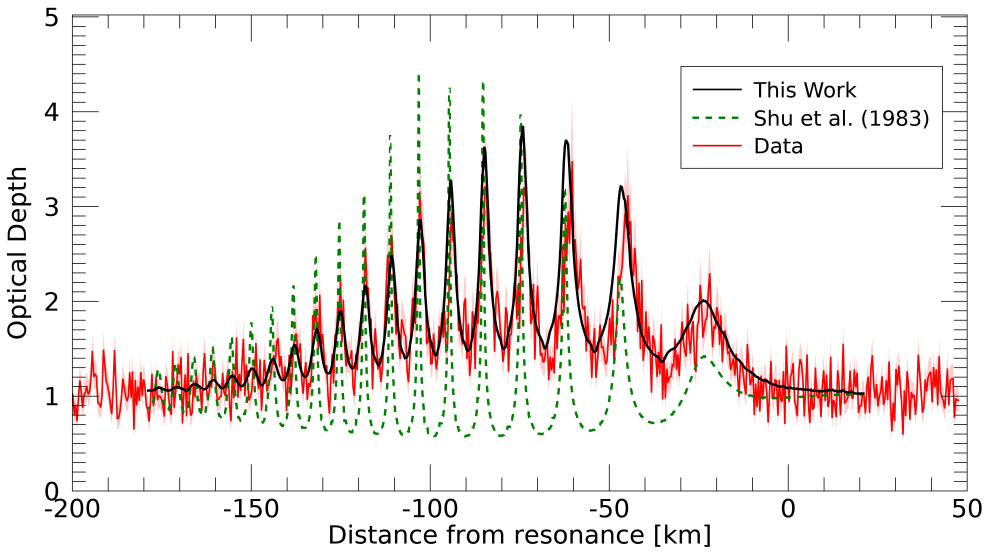

Figure 2.12: We compare an occultation of γ-Pegasus (rev 32I, $B = 20.3$,$B_{\rm eff} = 26^\circ$) seen by Cassini (solid red) to our model (solid black) with the parameters from the 3rd row in Table 2.4, and SCL theory (dashed green) using the viscosity from Esposito et al. (1983) ($\nu = 280\,{\rm cm}^2/{\rm s}$) and our best-fitted σ (our σ is used to ensure the peaks between both models better match the data). The error bars in the data are shown by a light red filled curved in the background of the plot. The underprediction of the troughs in SCL is addressed in the new model, as the haze layer increases the minimum optical depth of the occultation, and the peaks fit better due to the shorter damping length. Note that the peaks are now broader in the new model due to the extended height of the haze, which is something we also see in the data. The discrepancies in the separation of the initial peaks of the model with respect to the data persist.

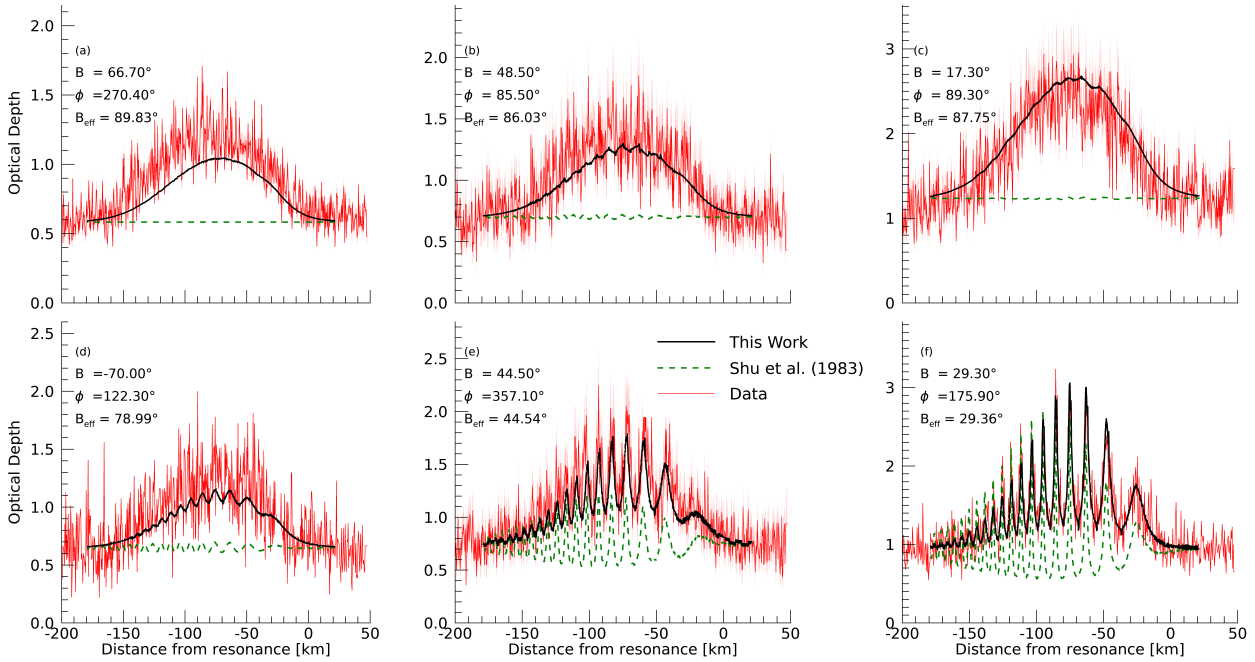

Figure 2.13: The haze model (3rd row of Table 2.4, solid black lines), and the SCL model (dashed green; same parameters as in Figure 2.12) compared to occultations (red lines) of (a) β-Centauri (rev77I), (b) κ-Centauri (rev35E) (c) α-Virginis (rev232E), (d) ϵ-Cassiopeiae (e) η-Lupus (rev34E), and (f) κ-Canis Majoris (rev168I). The error bars are shown by a light red filled curved in the background of the plot. In the top row we have azimuthal occultations ($\cos\phi < 1$), on the bottom row radial occultaions ($\cos\phi > 1$), at high, mid and low B angles (from left to right). For high $B_{\rm eff}$ occultaions, the SCL theory predicts an unchanging optical depth throughout the wave, but instead the data shows a symmetric rise in the optical depth centered at $-80\,\mathrm{km}$ from resonance. Our model reproduces both the position of the peak and the width of the Gaussian-like enhancement. The amplitude of these peaks, however, does not vary with opening angle B as our model predicts: for azimuthal occultations the scaling with B of the optical depth (which we model as $1/\sin B$) is too rapid—the model underpredicts (a) and slightly overpredicts (c)—while for radial occultations the scaling works well. The haze model also present a significant improvement when matching the data of low $B_{\rm eff}$ occultations.

of this optical depth enhacement for azimuthal occultations. While it fits well for intermediate B (b), for high (a) and low B (c) angles our haze model underpredicts and overpredicts the maximum optical depth respectively. This effect is not evident in the radial occultations (bottom row). This is a clear example of a ϕ dependent optical depth, or what has been called azimuthal brightness asymmetry. In other words, the haze does not behave an an isotropic absorbing medium. A potential explanation for this is discussed in the next section.

2.7 Discussion

Discrepancies between the optical depth predicted by the SCL model and those measure by Cassini UVIS and Voyager I (Gresh et al., 1986) have been partially addressed by our modifications to the theory (Figure 2.12). The addition of haze of particles released by self-gravity wakes improves the likelihood considerably, with a best value of χ^2 of 3.64 for the haze model with observed phases. Most of the explanatory power in the model comes from the existence of the extra layer of particles.

However, Figure 2.13 shows that the observed haze optical depth presents azimuthal brightness asymetry (ϕ-dependence). Given that the haze is hyposized to come from self-gravity wakes, the observed anisotropy may be inhereted from the self-gravity wakes, which are reponsible for the ϕ-dependence of the flat ring's optical depth. To improve our model to explain this anisotropy, a more-in-depth analysis of the dynamics presented in section §2.3 is called for. If the self-gravity wakes do have a preffered direction inside the BW, and the haze is coming from said wakes, the haze will present an anisotropy; this can be compared against the observations as an additional test for the dynamical model. Preliminarely, Figure 2.9 suggests that the azimuthal direction may be a preffered orientation for self-fravity wakes in the BW, but a chaos analysis needs to be done to determine the attractors in the rotation of wakes in the BW.

Figure 2.12 shows that the haze model's fit of the observed wave damping length yields a significantly high kinematic viscosity. It more than doubles the viscosity obtained from neighboring density waves Tiscareno et al. (2007), and it falls outside the upper error bars in Gresh et al. (1986). We compare our value with the literature in Figure 2.14 (Lissauer et al., 1984; Esposito et al., 1983; Gresh et al., 1986).

Figure 2.14 shows that Gresh et al. (1986), Lissauer et al. (1984), and Esposito et al. (1983) measured

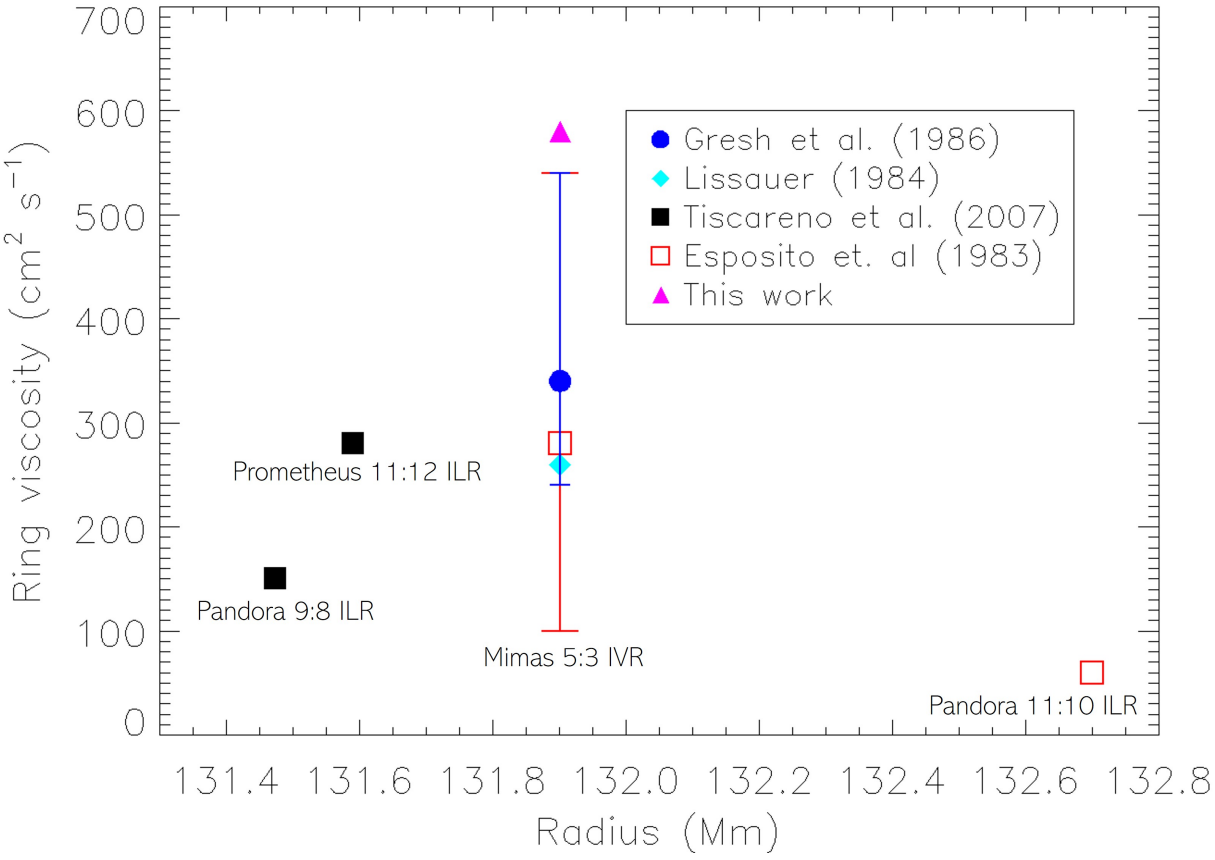

Figure 2.14: Measurements of the viscosity of the rings made by various authors around the bending wave region. The measurements done using the Mimas BW are the ones at 131.9 Mm. The values computed in this paper are the filled triangles. This work's values are considerably higher than the more recurrent value of $\nu = 280\,\mathrm{cm}^2/\mathrm{s}$. Our measurement lies outside the error bars of Gresh et al. (1986) and Esposito et al. (1983) (Tiscareno et al. 2007 and Lissauer et al. 1984 didn't include error bars). When comparing the values it is important to note that Esposito et al. (1983), Gresh et al. (1986), Tiscareno et al. (2007) and Lissauer et al. (1984) were fitting at most two occultations (or images) for their estimates, while in this work we use 60 occultations at different geometries to compute our values.

a lower viscosity than the best-fitted values of our work. Esposito et al. (1983) used one occultation of δ-Scorpii, while Gresh et al. (1986) used one low-angle radio occultations of the Earth (at two frequencies). Lissauer et al. (1984) used images of the shadows cast by the elevated ring to estimate where the wave-train ended. In this work we use 60 occultations at better resolution (400 m vs. 2 km). The signal-to-noise is also higher on average since we are looking at brighter sources, like γ-Pegasus and β-Centauri.

We see two reasons why their viscosity is lower. The first one pertains to the noise and the spatial resolution of the data: they didn't fit all the cycles because they couldn't see them, so instead of fitting the complete wave-train to find the viscosity they instead were attempting to fit the damping length ξ_D, which is the point at which the amplitude of the wave drops a factor of e. This approach would work if the SCL theory were adequate for this bending wave, which we see it isn't in its entirety, as shown in the first row of table 2.4 and Figures 2.12 and 2.13. This leads us to our second reason, the lack of a proper model for the extra optical depth. Without the haze our value for the viscosity would underpredict all of the peaks in 2.12. Moreover, in the case of Gresh et al. (1986), the occultations were so low angle that the optical depth of the peak was taken to be infinity (the slope of the wave and the viewing angle were almost the same), which means they mostly fit the troughs and not the peaks and we can see in Figure 2.12 that the underdamping in Gresh et al. (1986)'s fit is more evident in the peaks than in the troughs. In summary, Gresh et al. (1986), Lissauer et al. (1984) and Esposito et al. (1983) viscosity values are lower than the ones suggested in this work because in our occultations the late part of the wave-train can be clearly distinguished from the noise, and their prediction for the damping length relies on the SCL theory.

Nevertheless, the value Gresh et al. (1986) computed for the region is still higher than what Tiscareno et al. (2007) calculated from analyzing the 11:12 Prometheus density wave which used Cassini data and looks at weak bending waves where SCL is adequate (although Tiscareno et al. 2007 points out that the Prometheus 11:12 shows some non-linearity, it isn't enough to expect his results to be inaccurate, given their consistency with other estimates of the viscosity in the region). To be consistent with Tiscareno et al. (2007) we then have to consider that the bending wave itself increases the viscosity in a way that a density wave doesn't.

While a modification of SCL linear theory that accounts for the back-reaction of the wave to the

wake's rotation is yet to be done, we can expect that the inclusion of the wake-wave interaction will affect the damping length of the theory. A way to include this added dissipation is to consider the effects that the collisional forces (Eqn. 2.12) have on the wakes' vertical motion. In our current model the collisions are taken to be north-south symmetric in the frame of the wake: the same amount of particles are hitting the wake from above and from below, which results in a net vertical force of zero. This is probably not true, and the inelastic wake-wave collisions would cause a net damping of the the vertical motion of the wakes, and of the ring particles in general. Since we haven't included this effect, our model accounts for the extra dissipation by having a high value in the kinematic viscosity of the SCL term, in which the viscous effects of vertical collisions are modeled simply by $F_{\rm visc}/m = \nu d\dot{z}/dx$ (where m is the mass of the affected particle). However, even our simple collision model suggests a more complex interaction that depends on the slope, on the mass colliding with the self-gravity wake, and on the wake's size. The computation of this viscous force and the subsequent modification to SCL's wave profile are left to future work.

Angular momentum conservation between the rings and satellites indicates that the viscosity responsible for the spreading of the rings, and that which damps the waves, may not be related in a simple fashion (Tajeddine et al., 2017). However, if the momentum transport in both cases is dominated by the motions of self-gravity wakes, as suggested above, a higher damping viscosity will be closely related to a more efficient momentum transport in that region. Then, while the Mimas 5:3 BW is relatively strong (the 2nd strongest BW in the rings), self-gravity wakes allow the rings to transport the inflow of energy at resonance and form a continuous wave. Despite this extra dissipation, the Mimas 5:3 BW still has a slope of $\sim 15^{\circ}$, hence we can speculate that without the enhancement in viscosity provided by the self-gravity wakes, the rings would rift and create a gap similar to the ones seen in the Titan 0:-1 nodal bending wave (Nicholson & Hedman, 2016) and in protoplanetary disks misaligned with their star's obliquity (Rowther et al., 2022). Without a theory of when (at what slope and at what efficiency of viscous transport) warped disks break however, this remains a speculation. An attempt at modeling the Titan 0:-1 nodal bending wave using Cassini data may shed light on a general theory of rifted warps in disks.

The more efficient angular momentum transport within the wave could also be causing the diffusion of material into the neighboring regions. Consider the values measured by Tiscareno et al. (2007) of the

average surface mass density of the Prometheus 12:11 wave, which lies about 100 km closer to Saturn than the Mimas 5:3 BW. The average measured surface density value is $\sigma = 46.1\,\mathrm{g/cm^2}$. This corresponds to an increase of 25% with respect to our best-fit BW value (and a 24% increase with respect to Gresh et al. 1986's best-fit value). The non-linear nature of this density wave could be changing the local value of the surface density (Borderies et al., 1986), but the Prometheus 12:11 is not strong enough for this effect to change it more than 20%. So why does σ increase in this region? A possible explanation is that density waves, by their very nature of being density-changing phenomena, are unreliable measures for σ, although this wouldn't explain why the measured values are overstimating the BW value. Another more plausible explanation is that the higher viscosity in the BW region is causing the migration of material. A local radial increase (decrease) in viscosity has been shown to correspond to a local decrease (increase) in surface density in protoplanetary disks (Lyra, W. et al., 2015). If the change in viscosity is too abrupt, it can lead to an instability that can excite the growth of vortices in the disk (Papaloizou & Pringle, 1985). While this is not the case here, the increase in viscosity in the bending wave region may be causing a decrease in surface density there, and a corresponding increase in the nearby regions.

Comparing the values of Φ_{theory} and Φ_{obs} we see a general agreement for the theoretical phase of the wave (table 2.2). While there are many waves with a phase difference of $\sim 20°$, this is to be expected considering that a radial offset of $10\,\mathrm{km}$, either in the radial vector or the resonance position, and an error of $1°$ in the longitude of Mimas translates into a possible phase difference of $25°$ between theory and observation. Nevertheless, two stars show an offset in the phase greater than $90°$: AlpVir(210)I and BetCMa(276)E. Note that the dispersion relation works well for these occultations once the offset in the phase is corrected. That this only occurs in two out of 40 occultations makes us hesitant to propose a mechanism driving such a big offset. On the other hand, the offset could be due to a bigger systematic error in the radial offset of these particular occultations.

We also find two low-angle occultations in which the dispersion relation fails not only at the first cycles but everywhere in the wave-train: AlpCMa(274)E and AlpCMa(281)I. A possible cause of the dispersion relation difference can be a radial variation in the surface mass density of the ring. By using the fitted value for the isotropic model $\beta = 1.39$, via equation $\beta = \Sigma_0 \bar{\sigma}_{\mathrm{haze}}$ (§2.3.3), assuming $\bar{\sigma}_{\mathrm{haze}} = 1\,\mathrm{cm^2}$

we estimate a maximum haze surface mass density of $0.4\,\mathrm{g/cm^2}$ which is about 1% the best-fit for the ring's surface mass density. The existence of the haze is therefore consistent with Shu et al. (1983)'s dispersion relation which assumes a constant surface mass density throughout the wave and by itself is not evidence that there is a significant change in the ring's density. Nevertheless, if the average cross-section of haze particles is bigger ($10\,\mathrm{cm}$, although we note this is contrary to what is suggested by table 2.1) and radially changing (there are bigger particles released when the slope is bigger) there may still be a slow radial change of 5 to 10% which would affect the dispersion relation appreciably in low B_{eff} angles occultations. Nevertheless, why we only see this in two occultations out of 40 makes the answer to this question more complex. Note that incorporating the extra wake-wave interaction in the bending wave equation will also change the dispersion relation of the wave. The extent of this effect in the dispersion is left for future work.

Finally, we suggest how better understanding the Mimas 5:3 BW can help solve current problems in planetary rings. First, consider the overdamping of the Mimas 5:3 density wave (Borderies et al., 1986). Local increases in surface density may reduce the local shear-rate at that location, causing wakes to rotate as they adjust their pitch-angle (see Figure 2.7). While the rotation due to a changing shear-rate will be more gentle than the one described in this work, it can contribute to the increase in local viscosity seen in this density wave. Secondly, consider the puzzle set by Tiscareno et al. (2007) for the Iapetus -1:0 BW. This bending wave propagates outwards through an abrupt increase in optical depth called 'the inner A-ring edge.' Historically, researchers have interpreted this increase in optical depth as an increase in σ. However, σ also affects the dispersion relation of waves, and no such abrupt change is seen in the wavelength of the Iapetus -1:0 BW. If this edge corresponds to a point where self-gravity wakes start forming, given how unstable BW are to vertical perturbations within BWs, a haze of particles may contribute to the slanted optical depth increase. Properly applying the rigid-bar and haze models to these issues is left for future work.

2.8 Conclusion

We have shown that a necessary consequence of introducing rigid self-gravity wakes to the linear bending wave theory is that bending waves generate an extra layer of particles that is proportional to the amplitude of the slope. Even if we consider the scenario of the wake's partial disruption due to the interaction

with the bending wave, this disruption still creates the same layer of haze particles, given that the relative vertical velocities between the wakes and the ring are comparable to the characteristic vertical velocities of the particles as the wave propagates.

Using a ray-tracing code, we tested this additional signal and found that the extra layer of particles has considerable explanatory power for the Cassini UVIS occultations of the BW compared to Shu et al. (1983). Our best model explains the most discrepant and surprising features of the Mimas 5:3 BW; namely, the enhancement of the signal for the cases of normal occultations and a bigger than expected viscosity, $\nu = 576\,\mathrm{cm}^2/\mathrm{s}$, more than two times bigger than the viscosity computed from density waves. This shows that self-gravity wakes can be especially effective in preventing the opening of gaps in a vertically perturbed disk.

The rigid-bar model for self-gravity wakes proved to be successful not only in the case of the bending wave but also in the flat ring, as it showed that wakes tend to align at the same pitch-angle due to their mutual self-gravity, thus explaining why the average pitch-angle of the wakes is the same throughout the A and B rings even if the ring properties, like surface mass density and distance from Saturn, change considerably within them. The rigid-bar model can be used as an analytical tool to investigate the motion of self-gravity wakes in a perturbed environment, such as density waves.

While improvements have been made in explaining the Cassini UVIS dataset for the Mimas 5:3 BW, there are still issues with the current bending wave theory and we suggest a path to modify it in a way consistent with the results of this paper. We find that the theoretical dispersion relation tends to fail in the first cycles of the wave, and in some cases, it fails through the entire wavetrain. The reason for this may be the back-reaction that the self-gravity wakes' motion has on the propagation of the wave. The inclusion of this effect is suggested as a path to further improve the theory.

Chapter 3

Turbulent Magnetic Reconnection as an Acceleration Mechanism in the Earth's Magnetotail

3.1 Preface

This chapter is an unedited version of a paper submitted to the *The Astrophysical Journal* in September 2023. It is currently under review. The conceptualization of the problem was done by Robert Ergun, and the problem-solving strategy and the analysis of the simulation results were executed jointly between him and myself.

3.2 Introduction

In a magnetic reconnection region of the Earth's magnetotail, the Magnetospheric Multiscale (MMS) mission measured non-Gaussian distributions with accelerated ions (Ergun et al., 2020b); how these accelerated ions are energized is not well understood. Super-thermal ions of energies up to $100\,\mathrm{keV}$ have been seen in previous magnetospheric missions (DeCoster & Frank, 1979; Christon et al., 1991; Keiling et al., 2004; Grigorenko et al., 2009; Haaland et al., 2010; Artemyev et al., 2010) and theoretical literature followed proposing acceleration mechanisms. Energizing via the dawn-dusk electric field of magnetic reconnection has been considered (Speiser, 1965; Zelenyi et al., 2004, 2007) as well as ion jet acceleration (Litvinenko & Somov, 1993; Zharkova & Gordovskyy, 2004) and interaction with electromagnetic fluctuations (Artemyev et al., 2009; Perri et al., 2011). An acceleration mechanism that includes stochastic heating and generates magnetic holes has been shown to explain the energy distribution of electrons (Dolgonosov et al., 2013; Ergun et al., 2020a), but the case of energetic ions is more complex due to their slower initial speeds and their partially unmagnetized orbits (e.g. "serpentine orbits") (Speiser, 1965; Somov, 2013). When turbulence is

present, observed ion distributions have a substantial non-thermal tail extending to one hundred times the initial ion thermal energy.

Development of a power-law distribution generally requires an acceleration mechanism that favors energetic particles (Blandford & Eichler, 1987). Fermi-like processes, of which there are several flavors, are often invoked; for example, simulations show that repeated impulses to a set of partially trapped electrons in magnetic islands can cause a power-law distribution (Drake et al., 2006). Likewise, it has been advanced that turbulence in the near-Earth magnetotail also favors energetic electrons (Ergun et al., 2020b, 2022; Usanova & Ergun, 2022). While observations indicate that turbulence plays a role in ion acceleration, it is unclear what feature of turbulence favors energetic ions.

The MMS observations of strong turbulence suggest that at least three energization mechanisms are active (Ergun et al., 2018), all necessary to understand the energy balance that occurs in the reconnection region. These are: stochastic turbulent acceleration, ions jets, and the dawn-dusk electric field, E_y. The combined effect of the first two mechanisms — stochastic acceleration by turbulent electric fields and bulk acceleration of ions into opposing jets — carries a significant fraction of the magnetic field annihilation energy away from the x-line. Likewise, the measured reconnecting electric field (E_y in this article) is sufficient to energize ions to ten times the initial thermal energy, supporting that energization due to advancing along the E_y dawn-dusk field can also be active (we refer to this energization as "Speiser-like"). An important question that needs to be resolved is the relative contribution of these three mechanisms and how they interact.

Test-particle simulations are often employed to elucidate the acceleration mechanism for ions. They subject ions in a magnetic field-reversal region to various electromagnetic field models and allow the analysis of their individual trajectories as well as their statistical behavior. Veltri et al. (1998), Greco et al. (2002) and Taktakishvili et al. (2003) studied the motions of ions under static magnetic fluctuations, and Greco et al. (2009) and Perri et al. (2011) included electromagnetic fluctuations as clouds of electromagnetic fields that oscillate throughout the reconnection plane; this scheme was proposed to suggest a Fermi acceleration mechanism, which is known to produce power-law tails in the most energetic parts of a distribution (Fermi, 1949; Davis, 1956). Dolgonosov et al. (2013) showed that a power-law of index -4.45 can indeed be

produced with this mechanism in the relevant energy range (>80 keV) whereas Artemyev et al. (2009) found a negative result (no power-law tail) by adding the electromagnetic fluctuations as phase-mixed plane-waves following a power-law spectrum.

The test-particle simulation used in this article is based on measured turbulent magnetic ($\delta\boldsymbol{B}$) and electric ($\delta\boldsymbol{E}$) fields and has several advantages over many current self-consistent codes. To properly reproduce the measured $\delta\boldsymbol{B}$ and $\delta\boldsymbol{E}$, a self-consistent code must have an enormous range of scales, a representative large number of particles at the smallest scales, and a correct electron-to-ion mass ratio. To properly treat ion acceleration a code must have a very large 3D simulation domain, long run times to allow ions to pass through the system, and, very importantly, fully open boundaries. A test-particle code can incorporate all of these features at the expense of self-consistent behavior. Moreover, most of the parameters of our simulation are well constrained by measurements: the particle distributions (densities and temperatures) at the boundaries, as well as the size of the turbulent region, can be estimated from data (Angelopoulos et al., 1994; Ergun et al., 2018, 2020b), the only exception being the length of the x-line of magnetic re-connection.

Basing the test-particle simulation on the event described in Ergun et al. (2020b), we find that, while energization by ion jets from magnetic reconnection and Spieser-like processes have substantial contributions, the most energetic ions (>80 keV) result from turbulent fields. Dynamically, most of these energetic ions cross the magnetic null plane multiple times, which results in higher energization by the turbulent fields, and, as we show, present the highest energization rate at $z = 0$. By preferentially energizing these 'serpentine' ions, the turbulence creates a separate population of ions that mostly exits in the dawn direction of the magnetotail and forms a high-energy, power-law tail in the distribution.

In section §3.3 we briefly overview the MMS observations. In section §3.4 we describe the test-particle simulation domain. In section §3.5 we show how a simulation with a $2R_E$-long x-line reproduces the MMS-measured ion flux and density depletion seen in the turbulent region. We explain the mechanics of the acceleration by following the trajectories of super-thermal ions and change the amplitude of the turbulent fields in order to expose the interplay between turbulent, Speiser-like, and ion jet energization. In section §3.6 we will discuss the implications of our findings for larger-scale regions of magnetic reconnection in astrophysics and in section §3.7 we end with the conclusions.

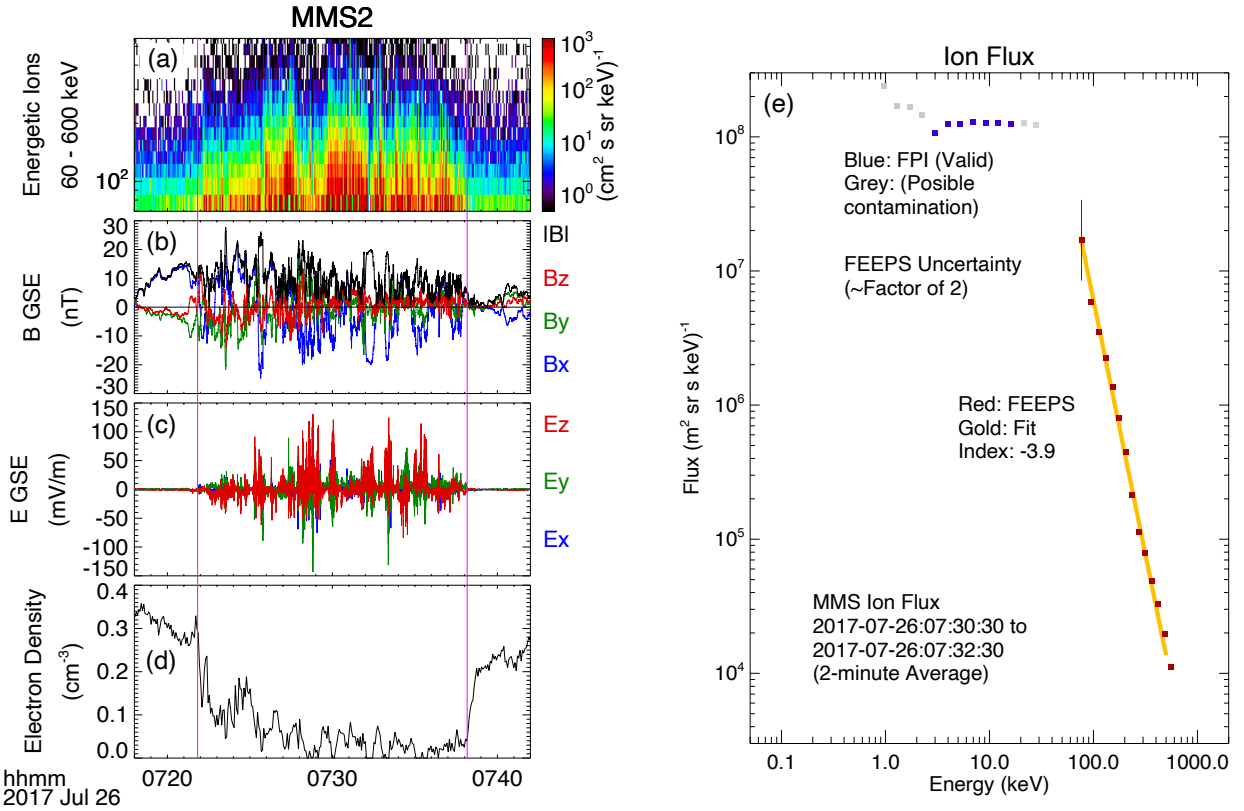

Figure 3.1: MMS 2 observations of a magnetic reconnection event in 2017 July 28th. Panel (a) displays high-energy ions measured by the Fly's Eye Energetic Particle Spectrometer (FEEPS); these include ions with energies >80 keV. Below are the turbulent magnetic fields (b), electric fields (c), and density depletion in the region (d). Panel (e) shows the ion fluxes extracted from the measurements of the FEEPS instrument.

3.3 MMS observations

A subset of MMS observations of accelerated ions in a turbulent magnetic reconnection event is displayed in Figure 3.1. The event is in the Earth's magnetotail roughly 23 R_E from Earth. Panel (a) displays the intensity of energetic ions from 60 keV to 600 keV measured by the Fly's Eye Energetic Particle Spectrometer (FEEPS; Blake et al. 2016). Given the nominal ion temperature in the plasma sheet is roughly 4 to 5 keV, these fluxes have been energized by more than a factor of ten. The concurrent magnetic fields, electric fields, and plasma density are shown in the panels below. The magnetic field signal shows that the fluctuations ($\delta \boldsymbol{B}$) have nearly the same amplitude as the background field ($\boldsymbol{B_0}$) suggesting strong turbulence. Intense electric fields and a strong density depletion are evident.

Figure 3.1(e) shows the ion intensity averaged over a two-minute period of the turbulent region. The

blue squares are from the Fast Plasma Investigation (FPI; Pollock et al. 2016) and the red circles are from FEEPS. The orange line is a power-law fit. A power-law tail can be seen at the highest with an index of -3.7. The energetic ions appear to be locally accelerated. From arguments elaborated in Cohen et al. (2017), these high-energy ions are predominantly protons.

3.4 Test Particle Simulation

We design a test-particle simulation after the above event to better understand ion acceleration. The basic idea is to reproduce realistic background and turbulent electromagnetic fields in order tofollow the ion trajectories through the region and analyze the kinetic behavior of ions under those fields. The features of the ion fluxes from the simulation can then be compared to those of the measured ion fluxes. In this section we describe the simulation domain (§3.4.1), the background fields (§3.4.2), the turbulent fields (§3.4.3) fields, and the boundary conditions (§3.4.4). More details about the simulation can be found in Appendix B.

3.4.1 Simulation Domain

Figure 3.2 sketches the simulation domain, which contains a smaller turbulent region. Ergun et al. (2020b) estimated the physical extent of the turbulent region to be roughly (factor of two) 16 R_E in the direction of the reconnecting magnetic fields (the x direction) using an estimated the retreat velocity of $\sim 100\,\mathrm{km/s}$ and the fact that the turbulence and accelerated ions are detected for roughly 16 minutes. The turbulence appears to extend in the z direction (normal to the current sheet) to the plasma sheet boundary layers (South to North), which gives a z extent of roughly $\sim 1.5R_E$ (Baumjohann et al. 1989). This distance is in consort with the expected extent of the ion diffusion region of magnetic reconnection normal to the current sheet of several ion skin depths ($d_i \sim 1000\,\mathrm{km}$).

The extent along the y direction (x-line of magnetic reconnection) cannot be established given the close spacing of the MMS spacecraft. Observations from multi-spacecraft missions such as Geotail and Cluster (Nakamura et al., 2004; Grigorenko et al., 2009; Haaland et al., 2010; Artemyev et al., 2010) indicate the x-line can be anywhere from $1R_E$ to $3R_E$. In the simulation, we treat the length of the turbulence along the x-line as a parameter, $2R_E$ being the value that best reproduces the ion fluxes observed by MMS (Figure

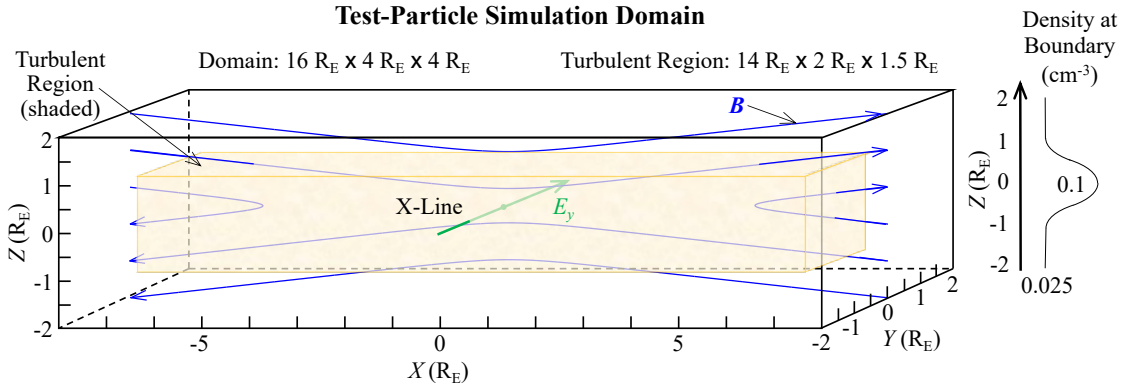

Figure 3.2: Sketch of the simulation box. The turbulent region is shaded in tan. The boundaries of the turbulent region are gradual, extending $0.25R_E$ into and outside of the stated boundary. The blue lines depict the background magnetic fields. The diagram at the right shows the boundary density as a function of z.

3.1); the degree of ion energization is sensitive to this dimension.

The dimensions of the simulation domain are $16R_E \times 4R_E \times 4R_E$. The turbulent fields $\delta\boldsymbol{B}$ and $\delta\boldsymbol{E}$ are only present in a smaller region of dimensions $14R_E \times 2R_E \times 1.5R_E$. A no-turbulence buffer zone of at least $1R_E$ is introduced to allow high-energy particles to re-enter the turbulent region during a gyration.

3.4.2 Background fields

The event in Figure 3.1 occurs in a highly turbulent region of magnetic reconnection. Even though the turbulence visibly obscures the background fields of magnetic reconnection ($\boldsymbol{B_0}$ and $\boldsymbol{E_0}$), they can be estimated via data smoothing combined with modeling using well-established properties of magnetic reconnection. The background magnetic field in the simulation domain consists of an unperturbed, sign-reversing component in the x direction modeled after a Harris-like current sheet. The same reversal configuration is applied in the z direction (the north-south direction) to form a magnetic reconnection region with an 8:1 ratio. The background fields are described as:

$$\boldsymbol{B} = B_{0x} \tanh\left(\frac{z}{\lambda_z}\right)\boldsymbol{e_x} + B_{0z} \tanh\left(\frac{x}{\lambda_x}\right)\boldsymbol{e_z} \tag{3.1}$$

where $\lambda_x = 8\lambda_z$ and λ_z is the half-thickness of the current sheet, for which we use ion skin depth $d_i = c/\omega_{p_i}$ (where ω_{p_i} is the ion plasma frequency and c is the speed of light). From the average measured plasma

density, the ion skin depth is determined to be $\sim 1000\,\mathrm{km}$ (Ergun et al., 2020b). The extent of the simulation box is $\sim 100 d_i$ in x by $\sim 25 d_i$ in z. B_{0x} is set to the measured value of $20\,\mathrm{nT}$ (Ergun et al., 2020b) and B_{0z} is $1/8$ of that value, $2.5\,\mathrm{nT}$. The blue lines in Figure 3.2 represent the background magnetic field lines. Note that the sign-reversing north-south magnetic field makes the total magnetic field at $z = 0$ non-zero (except at a point), and hence it plays the role of B_n in Greco et al. (2002) and Perri et al. (2011).

The background electric field is:

$$\boldsymbol{E}_0 = E_y \boldsymbol{e_y} \tag{3.2}$$

with E_y set to the measured value of $2.7\,\mathrm{mV m^{-1}}$ (Ergun et al., 2020b) within the turbulent region and reducing to $E_y = 1.35\,\mathrm{mV\,m^{-1}}$ in the buffer zone.

3.4.3 Turbulent fields

A chief advantage of a test-particle simulation is that the turbulent electromagnetic fields, $\delta\boldsymbol{B}$ and $\delta\boldsymbol{E}$, can be designed to closely mimic those in observations. In this effort, we employ a set of pseudo-randomized electromagnetic and electrostatic waves designed to match the measured properties of $\delta\boldsymbol{B}$ and $\delta\boldsymbol{E}$ including amplitude, wave speeds, coherence times, coherence scales, and the measured power spectra. $\delta\boldsymbol{B}$ shows a Kolmogorov (1991)-like turbulent power-law. We reconstruct $\delta\boldsymbol{B}$ with 200 plane-waves:

$$\delta\boldsymbol{B} = \sum_n \boldsymbol{A_n} \cos\left(\boldsymbol{k_n} x - \omega_n t + \phi_n(x,t)\right) \tag{3.3}$$

where $\boldsymbol{A_n}$ is the amplitude of wave n, $\boldsymbol{k_n}$ is its wave number, ω_n is the angular frequency, and ϕ_n is an arbitrary phase. The amplitudes and directions of $\boldsymbol{A_n}$ are pseudo-random, biased to match the measured spectra, ω_n and k_n are set to mimic the measured speeds (see Appendix B), and ϕ_n are randomly assigned (0 to 2π) and vary in time and space to match the measured coherency times and distances as a function of frequency.

Once $\delta\boldsymbol{B}$ is determined, the electromagnetic part of $\delta\boldsymbol{E}$ is constructed directly from Faraday's law. An electrostatic component of $\delta\boldsymbol{E}$ is also developed emphasizing the perpendicular (to $\boldsymbol{B_0}$) component

using the same procedure. The wave numbers are estimated from measured speeds of $\delta \boldsymbol{E}$. A small parallel contribution is added to match the $\delta \boldsymbol{E}_{||}$ spectrum. A comparison of the reproduce $\delta \boldsymbol{B}$ and $\delta \boldsymbol{E}$ spectra with the measured spectra is in Appendix B.

The total fields are then given by:

$$\boldsymbol{B} = B_{0x} \tanh\left(\frac{z}{\lambda_z}\right)\boldsymbol{e_x} + B_{0z} \tanh\left(\frac{x}{\lambda_x}\right)\boldsymbol{e_z} + \delta \boldsymbol{B}(\boldsymbol{r}, t) \tag{3.4}$$

$$\boldsymbol{E} = E_y \boldsymbol{e_y} + \delta \boldsymbol{E}(\boldsymbol{r}, \boldsymbol{t}) \tag{3.5}$$

The equations of motion for protons is $m d\boldsymbol{v}/dt = e(\boldsymbol{E} + \boldsymbol{v} \times \boldsymbol{B})$.

3.4.4 Boundary Conditions

The particles that enter the plasma sheet from the lobes have a source located somewhere in the magnetosphere mantle (Russell et al., 2016), and hence historically the temperature of the injected particles in simulations has been $0.1 - 1\,\mathrm{keV}$ (Greco et al., 2002). However, MMS measures a distribution outside of the turbulent region with a temperature of $4\,\mathrm{keV}$ which we employ. The measured distribution can be described as a shifted Maxwellian with a temperature if $v_{\mathrm{th}} = 4\,\mathrm{keV}$.

The simulation uses the measured number density outside the region of about $n_{\mathrm{sheet}} = 0.1\,\mathrm{cm}^{-3}$. The number density varies with the distance from the plasma sheet, reducing by a factor of 4 in the lobes (n_{lobe}):

$$n(z) = (n_{\mathrm{sheet}} - n_{\mathrm{lobe}})\,\mathrm{sech}^2\left(\frac{z}{z_{n0}}\right) + n_{\mathrm{lobe}} \tag{3.6}$$

where z_{n0} is the thickness of the current sheet. Ions are injected at the boundaries to mimic the prescribed density and temperature. Ions that exit the domain are removed.

3.5 Results and analysis

In this work, most of the numerical results are obtained by averaging the results of multiple runs. A "run" starts by initializing 1800 particles in the simulation domain at $t = 0$ with the density profile described in Equation (3.6) and a temperature of $4\,\mathrm{keV}$. During a run, one particle is randomly injected at every time-step of $dt = 0.01$ s, following the density profile and fixed temperature (4 keV) at the boundary. Each run advances in time until it reaches a steady-state at $t = 100$ s (no results used) after which few of the initialized ions remain. The resulting ion fluxes, temperature, and density are recorded from $t = 100$ to 300 seconds during which $\sim 20,000$ ions pass through the simulation domain. Each run has a unique set of 600 pseudorandomly generated waves ($\delta\boldsymbol{B}$ and $\delta\boldsymbol{E}$) as described above. We distinguish a run from a simulation. A "simulation" is an ensemble of runs where the random variables are regenerated including $\delta\boldsymbol{B}$ and $\delta\boldsymbol{E}$. To compile distributions, for example, we use an ensemble average of 50 runs during which roughly 1 million particle pass through the system and $30,000$ waves are generated.

The main goals of section §3.5.1 are to (1) determine the extent of the turbulence in the y (dawn-dusk) direction, which is not well constrained in the observations, and (2) demonstrate that the test-particle simulation reproduces MMS observations reasonably well. In section §3.5.2, we examine the acceleration mechanisms that allow ions to reach the high energies ($>80\ \mathrm{keV}$) seen in the data. In the acceleration study, we show that the motion near $z = 0$ is most critical and that the majority of the energetic particles exit through the $+y$ (dusk) face. By analyzing individual and collective trajectories, we determine that energization favors ions crossing the magnetic reversal plane. Moreover, once energized after crossing the magnetic reversal, those particles are more likely to further gain energy, which leads to the development of a power-law tail (acceleration). To demonstrate the impact of turbulence, we compare the results of simulations with and without turbulence imposed.

We start by showing how our simulation can reproduce the MMS-measured omnidirectional fluxes, temperatures and densities in the turbulent region.

3.5.1 Baseline Simulation

The Baseline Simulation employs parameters determined by MMS including $\boldsymbol{B}$, $\boldsymbol{E}$, ion boundary temperature and density, and the extent of the turbulent region. The dawn-dusk extent of the x-line ($y-$direction) is the only poorly constrained parameter. To determine this distance, the simulation is performed over a range of x-line lengths. The extent in the y direction is then chosen so that ion fluxes best agree with those observed by MMS.

Figure 3.3 compares the simulated fluxes to the observed fluxes. The simulated ion fluxes are plotted in physical units by properly weighting ions as they enter the domain. The measured flux distribution (magenta and red squares) is best matched by the simulation with an x-line distance (turbulent region length in y) of $2R_E$. A $4R_E$ x-line length in the simulation increases the energetic (>80 keV) fluxes by more than a factor of 2, whereas a shorter x-line (not displayed) decreases the energetic fluxes. Since the observed energetic particle fluxes vary by over a factor of two, we believe that the simulation reproduces the energetic acceleration well. The measured 15 keV to 27 keV ion fluxes (magenta squares) are somewhat higher but within the observed variations (factor of two). A better agreement is found if the ion fluxes in the simulation are measured on the $+y$ side of the domain.

Figure 3.4 (top) shows the ion temperature as a function of run time. The initial transient from $t = 0$ to 50 seconds shows rapid ion energization. One can see that the test-particle simulation achieves a steady state before 100 seconds. The resulting steady-state ion temperature of $\sim$ 14 keV is in good agreement with that reported in Ergun et al. (2020b). Figure 3.4 (bottom) shows the ion density in the center of the simulation domain as a function of x. The density inside the turbulent region is roughly $1/4$ of its value outside of the box, which is consistent with the data shown in Figure 3.1 (lower left panel).

As the system enters its steady-state, pressure balance is maintained (within a factor of 2) because the temperature increases as the density depletion onsets. Deviations from the pressure equilibrium are to be expected given the magnitude of the turbulent fields. It is also to be expected that the pressure balance is not exact but remains within a factor of 2 throughout the simulation given the absence of electrons. In this point we see a similarity to Greco et al. (2002)'s test-particles simulation: while our simulation is not *a*

priori self-consistent, we find it is nearly self-consistent *a posteriori*. An necessary component for achieving pressure balance in current sheets in Greco et al. (2002), Artemyev et al. (2009), Perri et al. (2011), and in the present work is the electromagnetic fluctuations themselves.

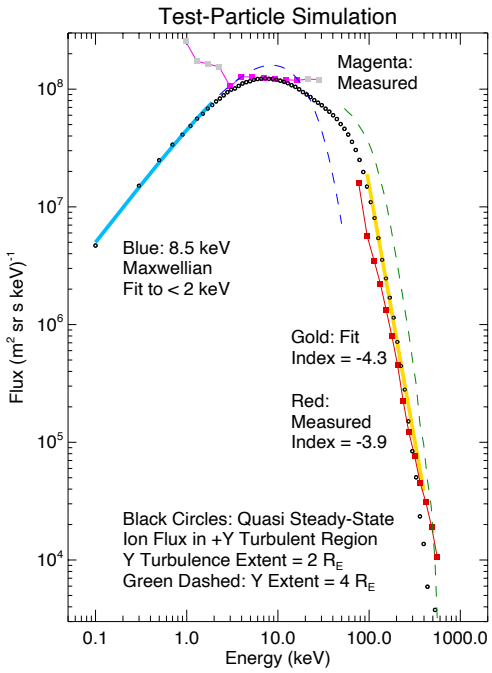

Figure 3.3: MMS data compared to the Baseline Simulation. The black dots represent the omnidirectional ion flux as a function of energy taken in the $+y$ side of the simulation domain, and the yellow line is a power-law fit of index -4.3. The magenta squares and red squares are MMS observations extracted from the event in Figure 3.1; the red squares fit a power-law of index -3.9. The blue line represents a Maxwellian distribution at $8.5\,\mathrm{keV}$ which we fit to the ions with energies lower that $2\,\mathrm{keV}$. The dashed green lines show the ion flux for a simulated x-line twice as long. With respect to the red line, the high-energy flux increases by more than a factor of 2.

In order to better understand how the energetic tail is generated, we can ask where ions are energized the most. To do so, we record the instantaneous energization rate at 0.1 second intervals as a function of position and find that the majority of the energization (and de-energization) occurs near $z = 0$, where the background magnetic field is the weakest (see Figure 3.5). The positive and negative changes in energy reflects the stochastic nature of turbulent energization. Similar results regarding z dependence of the heating rate were reported in Greco et al. (2002) and Artemyev et al. (2009), and were mostly interpreted as *quasi-adiabatic acceleration* due to the dawn-dusk electric field E_y. However, we also find a net positive

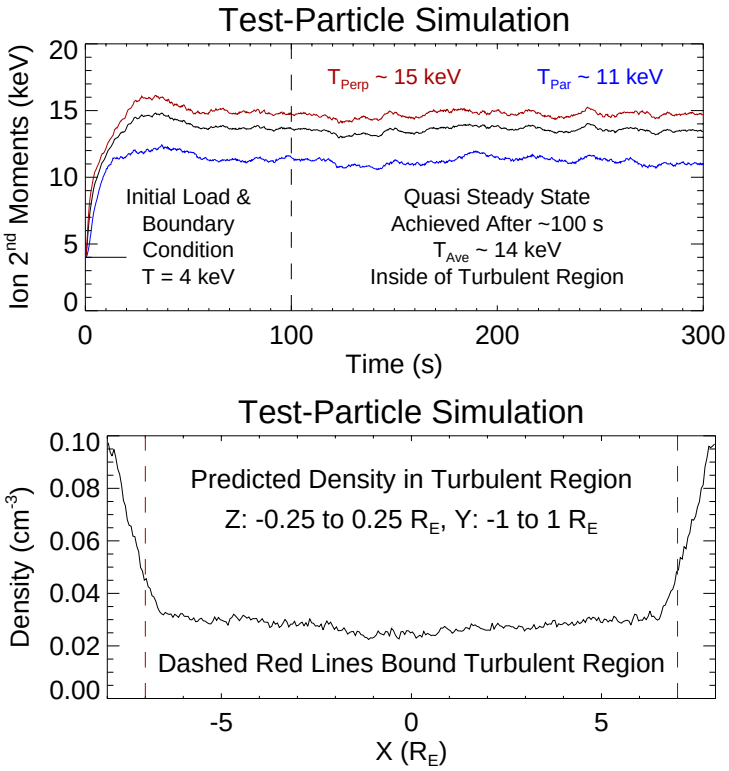

Figure 3.4: Top: Evolution of the temperature inside the turbulent region of a function of time. The simulation is initially loaded with particles at $4\,\mathrm{keV}$ and particles are injected at the boundaries also at $4\,\mathrm{keV}$. The temperature quickly reaches a steady-state at $14\,\mathrm{keV}$. Bottom: Density profile in the x direction for the Baseline Simulation. The density depletion results from the strength of the turbulent fluctuations of the electromagnetic fields.

energization that emerges when we sum the negative and positive energy changes produced by the turbulent fields, which is characteristic of second order stochastic acceleration (Miller et al., 1996; Somov, 2013). Quasi-adiabatic and stochastic processes are combining and interacting to generate a net energization when the turbulent is present; a closer analysis is needed to separate and understand the two effects.

The agreement between simulation and observation in the ion fluxes (Figure 3.3), ion temperature and density (Figure 3.4), and consistency with previous analysis (energization near $z = 0$) (Greco et al., 2002; Artemyev et al., 2009) makes the case that the simulation is properly representing the observed ion acceleration, and can be used to better understand the mechanism behind this energization. To unveil the role of turbulence versus Speiser-like energization, we take a closer look at individual ion trajectories of ions with or without the turbulent fields.

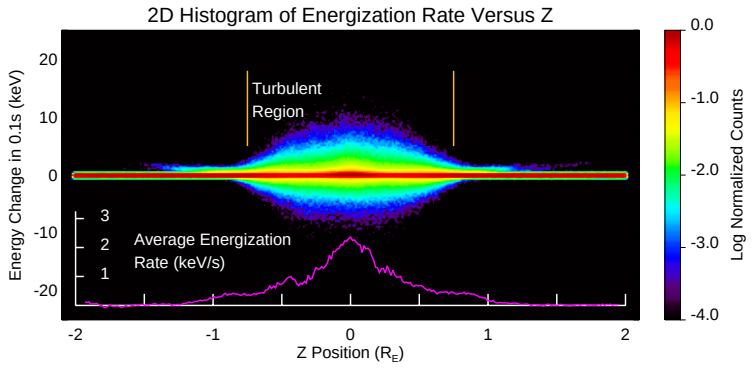

Figure 3.5: 2D histogram of the energy change (gain or loss) over 0.1 seconds of each ion in the baseline simulation, as a function of their position in z. The vast majority of ions see less than 0.1 keV in 0.1 seconds, which appears as a horizontal red bar. However, a subset of ions see strong energy changes both positive and negative, which indicates a strong stochastic contribution from turbulence. When averaged, the net energization is positive (purple trace).

3.5.2 Ion trajectories and the role of turbulence

Without turbulence, energy gains come uniquely from the electric field E_y, the longer the drift along y the higher the energy gain. From a 2D magnetic reconnection point of view, most particles forming the ion jet enter a z face and exit an x face, often accelerated to near-Alfvén speed (Figure 3.6 top left, magenta trace, "Ion jet"). With no turbulence, we find this "Ion jet" trajectory forms roughly 30% of the ion jet in the 3D case. "Fermi-reflected ions" (top left, green trace) make a similar contribution to the ion jet. Ions that enter through the $\pm x$ faces can migrate along y with non-adiabatic orbits gaining additional energy and leave the $+y$ face (bottom left, red trace, "x-entering Speiser"). We also find many ions that enter the $-y$ face, gain energy with a non-adiabatic motion, then exiting the $\pm x$ face (bottom left, blue trace, "Speiser-enhanced ion jet"). These orbits are also common (likely due in part to the limited y extent of the simulation domain) and dominate the highest-energy part of the ion jet. Even with no turbulence, we find that the net energy flux exiting the $+y$ face is only slightly less than that carried by the $\pm x$ jets. The most common $+y$-exiting trajectory is the purple trace (enters $\pm z$ and exits $+y$, left panel, "Drifting Speiser"). The classical Speiser orbit (orange trace in the right panel; enter $-y$ exit $+y$) is relatively rare comprising only about 5% of the net energy flux exiting the $+y$ face in the no turbulence case.

To study how turbulence changes this picture we do two 1000 seconds runs: one with turbulence and

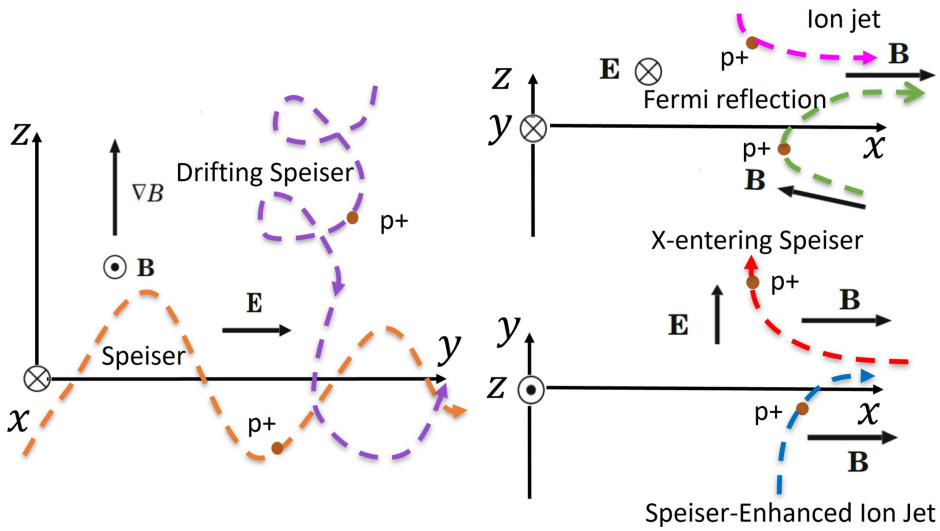

Figure 3.6: Orbits in the no turbulence case. Left: Sketch of a drifting trajectory due to $\boldsymbol{E} \times \boldsymbol{B}$ drifts (purple) and a Speiser-like trajectory (orange) moving parallel to the field E_y and crossing the $z = 0$ plane. Top Right: Sketch of a common trajectory of an ion jet (magenta), which enters a z face and leaves the through the x face, and a Fermi reflected ion (green) which enters and exits the $+x$ face, Bottom right: A x-entering Speiser orbit (red) which penetrates the reconnection region enough to become non-adiabatic and leave out of the $+y$ face. A Speiser-enhanced ion jet (blue), which enters the $-y$ axis and leaves the $+x$ face following the magnetic field line.

one without ($\delta\boldsymbol{B}$ and $\delta\boldsymbol{E}$ set to zero). For each run we count the ions leaving the $+y$ face while recording their energy and whether they cross the $z = 0$ plane. The results are presented in Figure 3.7. In order to highlight the differences between the plotted energy fluxes, we normalize the result such that the reference 4 keV Maxwellian entering energy flux peaks at unity.

A primary difference between the no turbulence and turbulence case is the dramatic increase in >80 keV fluxes when turbulence is present (Figure 3.7, right panel). In both cases the most energetic ions cross the $z = 0$ plane before leaving the $+y$ face (green traces in Figure 3.7), but the turbulence further separates this energetic population into a secondary population of highly energized ions, effecting a bi-modality in the flux-energy distribution. We identify a quasi-thermal peak at an energy of 9 keV (red trace, right panel) and a highly-energetic peak at 85 keV (green trace, right panel).

The peaks in quasi-thermal cores of the exiting fluxes (red traces in Figure 3.7) have nearly the same energy. The turbulence case has a slightly higher flux level. The increase in energy the quasi-thermal core of the distribution (from 8 keV to 9 keV) is consistent, roughly, to moving along E_y a distance of

an ion gyroradious, which is the most likely displacement in the no turbulence case (Russell et al., 2016; Taktakishvili et al., 2003). However, a displacement along E_y cannot explain the energies gained at the energetic end in the turbulent case, which is considerably greater than what the E_y field can yield, even when when considering displacements across the entire simulation domain.

We can further examine the relationship between Speiser-like energization and energization by turbulent fields by plotting energization as a function of the displacement Δy. In Figure 3.8, the dots represent the ions that leave the $+y$ face in the same 1000 s run that we use for Figure 3.7. The abscissa and ordinate values correspond to the ion's final energy gain and displacement, respectively, and the blue and black dots correspond to the simulations with and without turbulence. The relationship shown suggests that the acceleration process that generates the tail of the energy distribution still has a linear trend with displacement, the final energization of the ions being a combination of the effects of the Speiser and turbulent fields. Although it is expected in the no turbulence case to see a monotonically increasing trend between the displacement in y and the energization of the particle, the slope of this dependence steepens when turbulence in present.

We find the average dwell time of ions to be nearly the same, with and without turbulence. However, we find a greater net energization in the turbulent case for the $+y$-exiting ions. This stems from the fact that ions that cross $z = 0$ once tend to cross it multiple times, and the energization rate is also significantly larger for particles near $z = 0$ (see Figure 3.5). Therefore, ions that get energized due to their proximity to $z = 0$ tend to have trajectories that favor more subsequent energization, which leads to a runaway that generates the highly energized population seen in Figure 3.7.

That electromagnetic (EM) and electrostatic (ES) turbulence does not affect the average dwell time of particles complements earlier results (Veltri et al., 1998; Greco et al., 2002; Taktakishvili et al., 2003), which show that magnetostatic turbulence, contrastingly, increases the dwell time and the average Δy of particles, effecting a net acceleration. The combination of EM & ES turbulence, on the other hand, decreases and increases the dwell time of individual ions by roughly the same amount on average. Examining the trajectories in Figure 3.9 we can see both effects on the dwell time at play. We show four trajectories of ions in runs without (top) and with (bottom) turbulence, the two trajectories shown for each case having the same initial conditions. The blue-yellow trajectory is a known Speiser orbit with no turbulence: it enters a

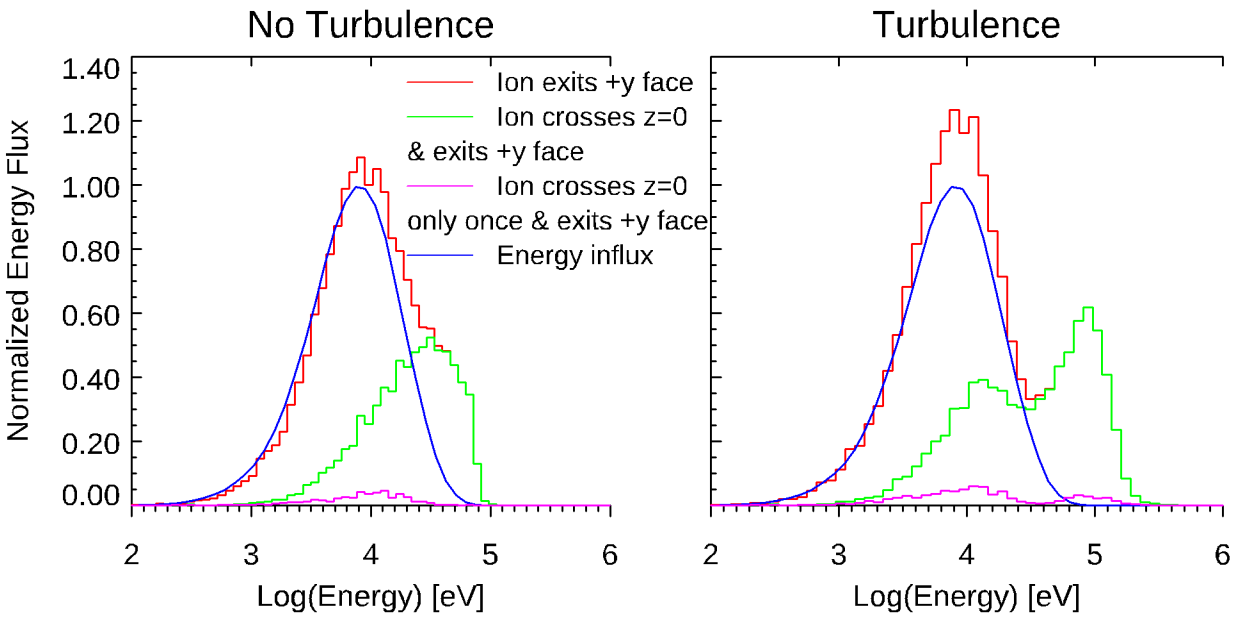

Figure 3.7: Left: Normalized log-linear plot of the exiting energies at the $+y$ face over a 1000 seconds run. Particles that cross $z = 0$ tend to partake in Speiser-like orbits and exit with a higher energy than those that do not cross the magnetic null. Right: The bimodal distribution, results from turbulent $\delta\boldsymbol{E}$ and $\delta\boldsymbol{B}$ acting on the ions that cross $z = 0$. The green histogram only counts the particles that cross the $z = 0$ plane at least once. The magenta histogram counts the particles that cross $z = 0$ only once. The observed energization of low-energy peaks (red traces) is from $8\,\mathrm{keV}$ to $9\,\mathrm{keV}$. Adding the turbulent results in a a similar low-energy profile profile, but the extra population of heated particles emerges.

x face, drifts into the current sheet ($\boldsymbol{E} \times \boldsymbol{B}$ drift), then exits the $+y$ face. On the other hand the green-red orbit contributes to the ion-jet with no turbulence: it enters the $-y$ face, then follows the magnetic field out of the $+x$ face. The dwell times for these orbits are represented in the color bars at the lower-right corner of the plots. While the dwell time of the blue-yellow trajectory increases due to turbulence (and its energy), the green-red trajectory accelerates through the region faster also due to turbulence. We find that when applying MMS-based EM & ES turbulence the turbulent acceleration exceeds the Speiser energization mechanism, and together they can energize particles by over a factor of ~ 20, achieving energies greater than $80\,\mathrm{keV}$.

Figure 3.10 shows the fluxes out of each of the faces of the simulation domain, without turbulence (top row), and with turbulence (bottom row). The red region highlights the $>80\,\mathrm{keV}$ energies of the flux-energy distribution. Fluxes exiting the $\pm x$ faces in the no-turbulence case show the expected ion jets common of magnetotail reconnection (e.g. Angelopoulos et al. 1994). Speiser-enhanced ions, such as the one depicted

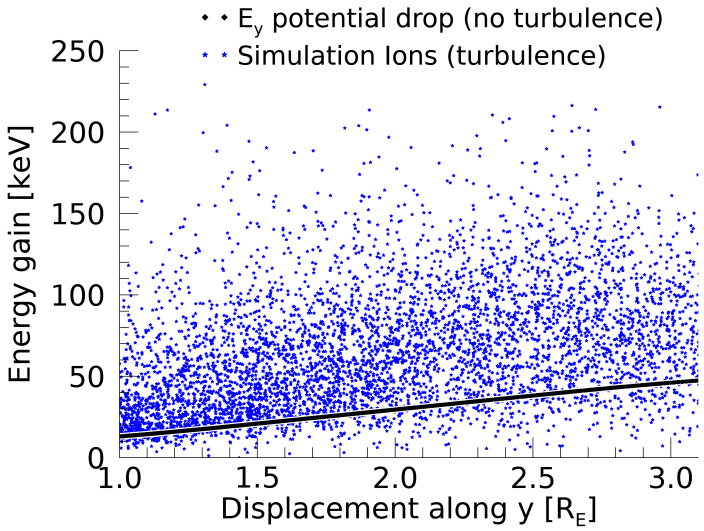

Figure 3.8: Energization of all particles leaving the $+y$ face as a function of their displacement in the y direction in a 1000 second run. The black and blue dots representing the ions in the no turbulence and turbulence runs respectively. The linear trend due to the electric field E_y is still present in the energy gained by the ions affected by turbulence (after Figure 4 in Dolgonosov et al. (2013))

in the green-red trajectory in Figure 3.9 (top), contribute the majority of the ions in the most energetic part of the jet ($>30\,\mathrm{keV}$). Without turbulence we find the expected result that the majority of the energetic ions leave through the combined $\pm x$ faces; however, a substantial number of energetic ions exit the $+y$ face as well, likely due to the relatively short extent of the turbulence in the y direction. In the no turbulence case, very few ions are energized to over 80 keV.

Once the MMS-based EM and ES turbulence is applied, the net energy flux out of the $\pm x$ faces increases, but the majority of the energetic ions exit through the +y face (Figure 3.10, bottom row). The net energy flux out of the $+y$ face dramatically increases. The energetic tail (> 80 keV) forms.

Therefore, as showcased through the trajectories in Figure 3.9, to understand the ion energization process one needs a 3D simulation with open boundaries, given that the ion jet acceleration and the Speiser acceleration and turbulence interact and enhance the total current leaving tailward. The inclusions this feature in our simulation, together with the MMS-measured turbulent field, provide the necessary component to produce the measured power-law. Comparisons between our scheme and others will be discussed in the

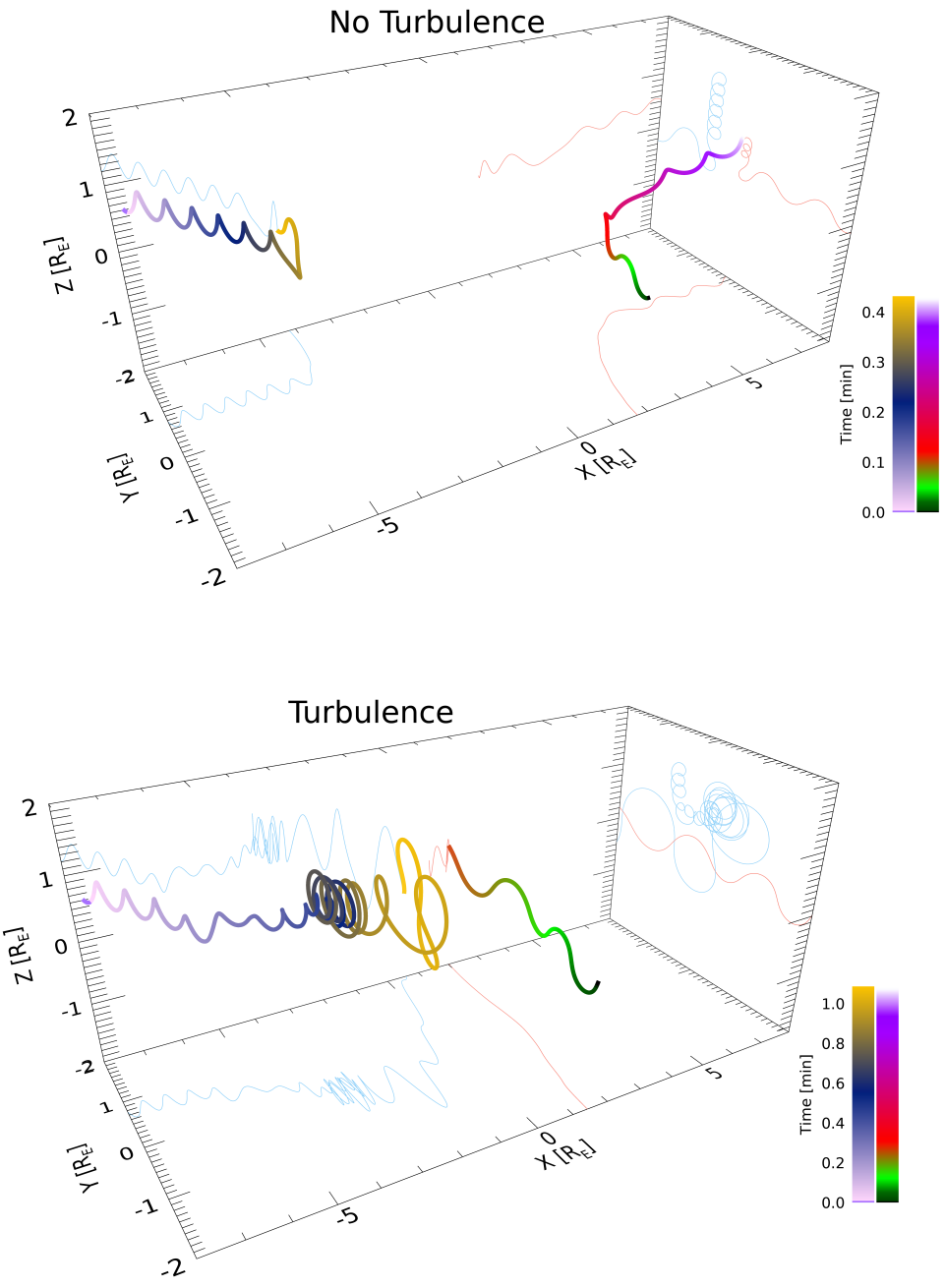

Figure 3.9: Top: Two simulated ion trajectories without turbulence. Blue-yellow trace: Speiser-like trajectory that drifts towards the magnetic null plane and then is directed towards the +y face. Green-red trace: A particle that contributes to the ion jet that follows the hyperbolic magnetic field and exits the $+x$ face. Bottom: the same ions but with turbulence. Blue-yellow trace: A non-thermally accelerated ion. When the particle crosses the magnetic null plane it engages in a Speiser-like orbit, and the dwell time and energization increase. The energized particle is redirected towards the $+y$ face due to the background electric field. Green-red trace: the ion is redirected toward the $+y$ face due to turbulence, and the dwell time decreases.

next section.

3.6 Discussion

In modeling an observed turbulent magnetic reconnection event, we have found that accelerated ion jets, Speiser-like energization, and the turbulence all are necessary ingredients to explain the net acceleration of ions in the magnetic reconnection current sheet of the magnetotail. Veltri et al. (1998), Greco et al. (2002) and Taktakishvili et al. (2003) did not include the electric field turbulence because they theorized that the measured magnetic turbulence by Geotail was due to tearing instabilities. However, MMS measured a turbulent electrostatic field which is significantly stronger than expected when considering the inductive field of the magnetic turbulence alone.

The impact of the stronger electric fields is clear when considering Artemyev et al. (2009) where the only electric component comes from this inductive field and no ions have energies of $100\,\mathrm{keV}$ or more. The main difference between Artemyev et al. (2009) and this work is the introduction of an electrostatic component of $\delta\boldsymbol{E}$ to the power-spectrum of the turbulent field. Secondarily, Artemyev et al. (2009) uses a Cluster-measured spectrum for the plane-waves with a single index of $-\frac{7}{4}$, and their turbulence is based on a measured correlation length. While we are using MMS-measured indices (see Appendix B) and correlation length and time in our turbulent field reconstruction, we believe the principal difference in the ion's energies in these two simulations stems from the inclusion of the electrostatic component of the turbulence.

The effects of the ES-turbulence in the energies also becomes appartent when comparing to the magnetostatic-only turbulence case studied by Veltri et al. (1998), Greco et al. (2002) and Taktakishvili et al. (2003). The highest ion energies in our simulation are an order of magnitude higher compared to the ones obtained in their simulation. Nevertheless, we confirm some of the findings in Veltri et al. (1998) and Greco et al. (2002): the density depletion centered at at $x = 0$ and the thickening of the Speiser layer. Unlike Veltri et al. (1998) and Greco et al. (2002) however, we don't see a reverse current layer forming on top and below the quasi-current sheet. Such a structure appears to be hard to maintain in an environment with high electric field fluctuations ($\delta\boldsymbol{E}$). Note that the density depletion has been measured by MMS and other spacecraft (Artemyev et al., 2010; Ergun et al., 2020b) and while the pressure remains mostly balanced by

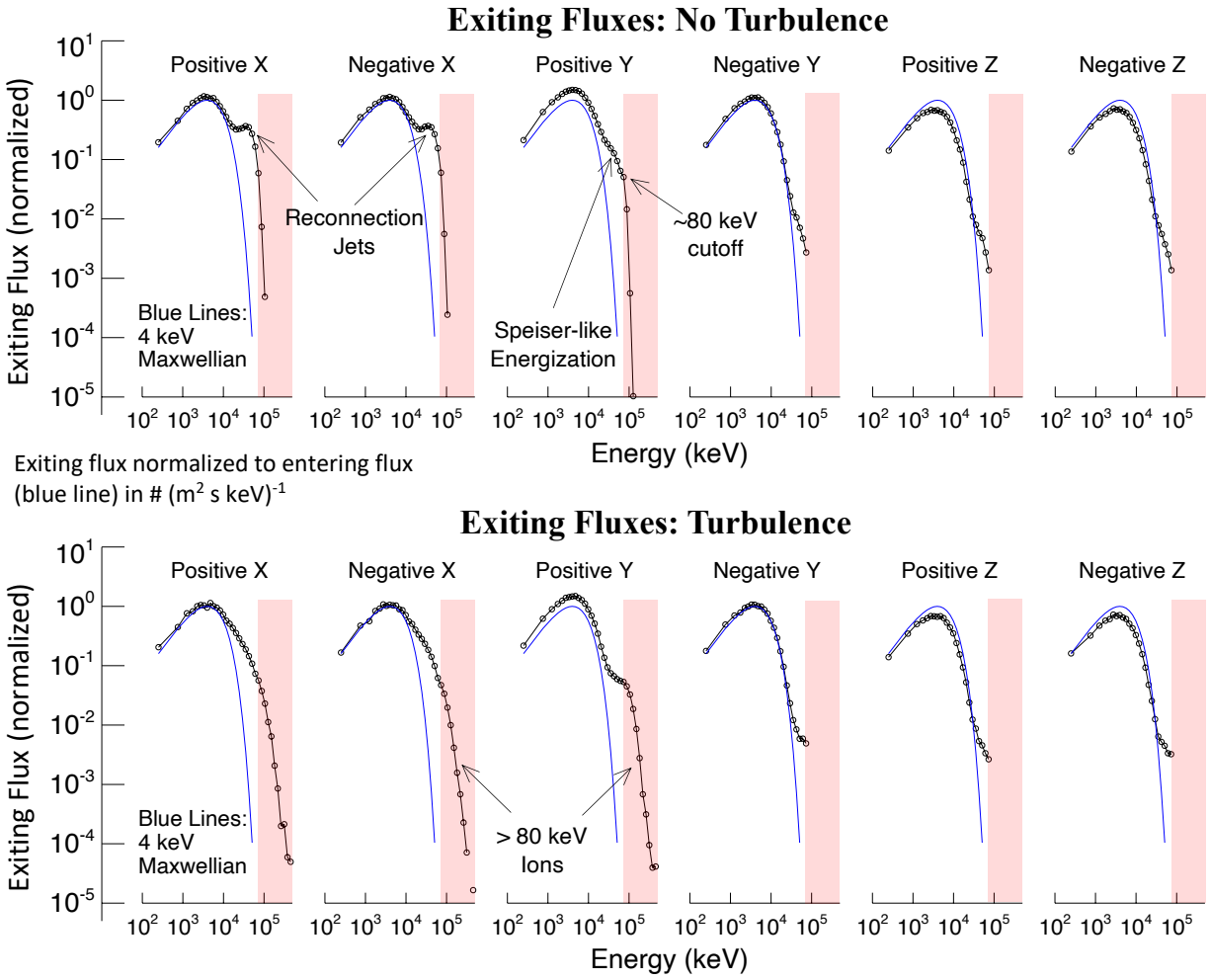

Figure 3.10: Exiting fluxes for each of the faces of the simulation, with and without turbulent fields. The red shaded region indicate the $>80\,\mathrm{keV}$ energies of the flux-energy distribution. A tail forms in the $+y$ face when we apply the turbulent fields. Moreover, the reconnection jets get energized as well.

the corresponding increase in the temperature within the turbulent region, the existence of extra turbulent magnetic field pressure is still important to balance the system (this is also consistent with Greco et al. 2002).

The only relatively unconstrained free parameter in our model is the length of the y axis. All other parameters are constrained by either MMS measurement or theoretical consistency. This prompts the question of how the energization changes if we change the size of the turbulent region. The dashed green line on Figure 3.3 indicates that energization increases significantly with the y dimension. Figure 3.8 suggests a linear relation can represent the dependence between the displacement and the energization in the turbulent case, which invites speculation on the energization that can occur in larger regions in other astrophysical contexts.

There is no theoretical limit on the scale of turbulence. On the other hand, the extent of an x-line of magnetic reconnection or the dimension of a current sheet could be limited or discontinuous given the increased pressure from ion acceleration. Nonetheless, widely scattered turbulence could extend overs scales far greater than that in Earth's magnetotail. In supernova remnants, the high-energy emission region of has been estimated to be of the order of $10^{-2}\,\mathrm{pc}$, and the Neumann layer (where turbulence is expected to be strong) is estimated to extend 10^{-4} pc (Zhang et al., 2018). Even if strong turbulence has a limited filling factor in these extensive regions, ion acceleration could plausibly contribute to the solution of what Fermi called the 'ion acceleration problem': ions need to already be accelerated to 200MeV to partake in the Fermi acceleration mechanism in supernova shock fronts (Fermi, 1949; Davis, 1956).

From MMS observations, it appears that the strong turbulence is enabled by magnetic field annihilation due to magnetic reconnection. The substantial ion energy flux that exits the $+y$ face of the domain also opens a question in how strong turbulence and the resulting ion energization can influence magnetic reconnection. It has been observed that the x-line length in the magnetotail (which extends over $20R_E$) rarely exceeds $\sim 3R_E$ (Nakamura et al., 2004). The test-particle simulation results may provide an explanation. The ion energy density (pressure) is significantly higher on the +y side of the domain (e.g. Figure 3.8). The increased ion pressure may limit the extent of an x-line in turbulent magnetic reconnection.

3.7 Conclusions

In this work, we employed a test-particle simulation that recreates an observed turbulent magnetic reconnection region of the Earth's magnetotail. The plasma parameters including density profiles, ion temperatures, and magnetic fields are based on measurements. The turbulent electromagnetic and electrostatic fields are reproduced by taking advantage of the four-spacecraft MMS mission, which allows for estimation of correlation lengths, correlation time, and waves speeds as well as detailed spectral properties and accurate parallel and perpendicular amplitudes. The dimensions of the turbulent region are estimated from observation and/or constrained by theory, the only exception being the extent along the x-line, which is treated as a open parameter. The test-particle simulation employs fully open boundaries allowing particles to enter and exit the domain as they would in nature.

The test-particle simulation is able to reproduce the measured ion distributions, density depletion, and ion temperatures, which corroborates the realistic reproduction of the turbulent magnetic reconnection region. Even though test-particle simulations are not self-consistent, the boundary conditions are designed to achieve approximate pressure balance. The ability to reproduce measured ion properties lends support that one can derive meaningful conclusions on the energization process.

The test-particle simulation in this article focus on a the case of strong turbulence in a magnetic reconnection region. We found that (1) EM & ES turbulence is largely responsible for the generation of the power-law tail in the ion distribution. We also found that (2) all acceleration mechanisms (the ion jets, the Speiser drift, and the turbulence energization) contribute significantly to the overall dynamics of the ions, the largest energy input comes from the turbulence itself. Comparing to several simulations that have been done before supports several of their findings, but highlights the necessity of imposing realistic EM and ES fields and employing open boundaries. Moreover, we found that (3) the presence of turbulence significantly enhances the number flux and energy flux of ions out of the $+y$ face. The most energetic part of this flux having crossed $z = 0$ multiple times, and hence dwelling in the region were we find the highest energization rates in our simulation.

We speculate the consequence of scaling this picture to a larger reconnection region, specifically,

those generated by the shocks of supernovae shells. When considering such scales we find that the reconnection mechanism described here can accelerate ions to the order of 100's of MeV, which can contribute to generating an ion population energetic enough to be further accelerated by Fermi acceleration and generate the energetic part of the cosmic ray spectrum.

Chapter 4

Conclusions

In this work, we have presented models for two complex situations in astrophysics: bending waves in Saturn's rings and ion dynamics in Earth's magnetotail reconnection region. As models tend to do, our work partakes in a number of distortions of the systems we study. In the case of the rings, the main distortion corresponds to the rigid self-gravity wakes. In the case of the ions in the magnetotail reconnection region, the lack of self-consistency. We established in the Introduction that distortions are not only for computational convenience, they also highlight the explanatorily relevant part of the models by exposing the emerging causal structure of the systems in question. As we will see in this final analysis, the distortions of our models are different in kind. One is an idealization, the other one an abstraction. Margaret Morrison's distinction between idealization and abstraction can help us better understand the assumptions in our model.

> Where idealizations distort or omits properties that are often not necessary for the problem in hand, abstractions (typically mathematical in nature) introduce a specific type of representation that is not amenable to correction and is necessary for explanation/prediction of the target system. What is crucial about abstraction, characterized in this way, is that it highlights the fact that the process is not simply one of adding back and taking away as characterized in the literature; instead it shows how certain kinds of mathematical representation are essential for explaining/predicting concrete phenomena. (Morrison, 2009a)

The processes of "adding back and taking away" are the de-idealization and idealization processes that were mentioned in the introduction. Idealizations are a specific type of approximation where one ignores certain terms in an equation, terms one may decide to add back later. In this way the rigidity assumption is not an idealization but an abstraction. We are not ignoring terms in a Taylor expansion or an equation, rather,

we are choosing the mathematical representation of torques in order to place the opposing influences on the self-gravity wakes orientation in balance: the tidal force of Saturn and the Keplerian shear. Likewise, when the bending wave is included, we can further add torques and study how the orientation changes. There is no clear way of de-idealization via further complicating the torques or the Euler equations of rigid motion: rigidity is clearly an abstraction.

Nevertheless, it allows us to make precise predictions: the wakes within the bending wave shed regolith; a layer of particles taller than 100 meters forms. If the proposed mission, Saturn Skimmer, were to get funded and study this region of the rings, it will see signatures of the 100 m haze (because it will have an occultation resolution of about 50 m with the proposed high-speed photometer). These are concrete explanations/predictions made possible by the abstraction. On the other hand, the plasma model is an idealization. We are ignoring a particular term in the magnetic field, and that is the one coming from Amperes' law. These ions move around, yet they generate no field. Moreover, displacement currents are present, and their associated magnetic fields are not accounted for. We could, in theory, "add this back," but it will make the simulation significantly more complicated. Moreover, studies that have attempted self-consistent simulation have not been able to reproduce the measured MMS-field (quote). An easier way of studying how these fields move the ions around is by imposing the fields externally and making them independent of the ions' motion.

Regarding the neglect of Coulomb's law, there is a good argument for why the external electric field may not be affected by the motion of the plasma: the assumption of quasi-neutrality. The electrons are moving close enough to the ions that they don't affect the field much (which is the same reason we don't have to model the electrons). This simplification can be made self-consistently. On the other hand, the effects of the current densities on the magnetic field are affected by the motion of the ions. The model's ability to reproduce the data supports the unimportance of the Ampere term for the causal structure of the omnidirectional flux power-law; this implies that even if these fields can affect the trajectory of individual ions in the plasma, their presence may not affect the net ion energization in the region.

Even if both models managed to reproduce the phenomena, we said in the introduction that there are criteria to judge a representation beyond just matching the data, but that we must be mindful of the purpose

of the models when doing so. We will proceed to make a deeper analysis of our models and answer the questions we set up in the introduction for each model.

> *Q.1: What purpose do our models fulfill and how does it justify the distortions introduced?*
>
> *Q.2: How do these models fulfill the explanatory and descriptive functions of scientific modeling?*

After answering these questions, we will see how the argued-for relation between explanations and assumptions came to bear in the peer review process of our Chapter 2 article. One referee's analysis held that, given the success of the model in matching the phenomena, the causal story given, and hence the explanatory part of the paper, was plausible even if the assumptions may not hold. These assumptions, however, are what allowed us to give the casual account of the phenomena, and hence, for the reviewer, it managed to be explanatory even if they were skeptical of the assumptions made. Finally, we will conclude by outlining important questions to consider when evaluating a model.

4.1 The Mimas 5:3 Bending Wave

Our haze model has at its core the Shu et al. (1983) bending wave model. Its derivation has several assumptions which I have outlined in each section of Appendix C. Most SCL assumptions, like the rigidity assumption, are also abstractions, and we will see that the logic for their introduction in 1983 is the same as the one appealed to in our model. The most glaring SCL abstractions is the assumption that the surface density σ varies slowly radially on the scale of the wave's wavelength such that we can pull it out of the integral over the radial coordinate x:

$$\int f(x)\sigma(x)dx \approx \sigma(x)\int f(x)dx$$

where f is a function of the viscosity and the vertical frequency (see Eqn. C.51 in Appendix C).

While the assumption was stated explicitly in SCL, its lack of realism was not mentioned. By 1983 there was good evidence of self-gravity wakes and the clumpy nature of rings (Colombo et al., 1976), but they were still omitted in the SCL model Part of the reason for this omission is that more than an idealization,

taking the rings to be smooth was an abstraction. The strategy was this: let us imagine a smooth ring, for which we can derive an analytic solution, and let us see if the A ring's measurable characteristics are like the ones of this smooth ring. Nowhere did SCL state that the ring was in fact smooth. Moreover, finding that the ring isn't smooth doesn't invalidate SCL's bending wave treatment, unless their theory is inconsistent with the phenomena. The success of the SCL model does not depend on its smoothness assumptions being right, but on its empirical adequacy. By the same token, its being empirically adequate is no guarantee that the assumptions are descriptively accurate, nor was the model created in order to argue for a smooth ring.

The nature of this assumption is the same as the rigidity assumption introduced in our models of self-gravity wakes. The model's successful representation of the target does not hinge on self-gravity wakes actually being rigid. One may think that given that the model successfully reproduces certain phenomena measured in the ring, like the attenuation of light in normal optical depth, this is a reason to believe the self-gravity wakes are (approximately) rigid. But this belief is only weakly supported by the empirical success of the model.

It would hence be a mistake to speculate how self-gravity wakes may in fact be rigid in order to justify our model. At most, our claim in Chapter 2 is that self-gravity wakes behave as rigid in the timescale of the pattern speed of the wave. Or rather, that the rigidity assumption is capturing certain aspects of its behavior, not that they have the property of rigidity. Rigidity serves as a tool to parametrize the opposing influence that the tidal force and the shear have on the orientation of the wake. It is a convenient *abstraction* that allows us to put these two causes in action and equilibrate them, yielding a highly *explanatory* equation for the pitch angle (equation 2.40). Such an equation parametrizes the pitch angle in terms of the relevant parameters.

It is important to see why this abstraction is useful even when there exists an N-body treatment of the self-gravity wakes's pitch-angle. Michikoshi et al. (2015) explores the pitch-angle relationship with many of the ring's parameters with a shear-box simulation as the one shown in Figure 2.4. They took many measures to make the model realistic: a velocity-dependent coefficient of restitution is introduced, as well as a high number of particles, and robust self-gravity effects. The changes of the pitch-angle with local density and distance from Saturn are studied. In a later study, the change of the pitch-angle with shear-rate was studied via the same model (Salo et al., 2018). These N-body simulations are descriptive, but lose some explanatory

power, as the explanations are left as a matter of interpretating the numerical output of the simulation. The main result of the paper isn't an explanation but a description of the behavior of the system.

The rigidity abstraction, on the other hand, allows us to analytically relate these parameters in a concrete way. It allows us to understand with one equation the different pitch-angles that self-gravity wakes may present. And, importantly, it can be used to predict phenomena. For instance, we know from numerical simulation that Density Waves can increase the local shear angle of the rings (Lu et al., 2018). With Eqn. 2.6 (also see Eqn. D.15 in Appendix D), we can easily make a prediction on the change of orientation of the self-gravity wakes given this increase in shear-rate. Moreover, we have an explanation for the change: the collisional interaction between the shear and the wake weakens and hence the tidal torque causes the self-gravity wake to point radially. The rigidity assumption is a successful example of an abstraction in planetary ring dynamics that, while not entirely accurate, is useful and explanatory.

These two models, the self-gravity wake model and the SCL bending wave model, come together in the model in our paper, which is the one we are evaluating as a representation of the Mimas 5:3 bending wave. To evaluate it properly we must ask what the purpose of the model is. Our paper is focused on explaining the increase in normal optical depth in the bending wave region with a model that start from first principles (i.e. the Eulerian equations of rigid motion) Our goal was to provide a *dynamical account* of why there would be extra light-attenuation in the region. Once we establish that the signal was generated by the existence of an extra layer of material, the main goal then becomes to explain why such a structure forms in the Mimas 5:3 BW. This provides the answer to Q.1:

A.1: The main purpose of our model is to explain the existence of the haze in the bending wave. We also want to make predictions about the nature of this haze, which was achieved by describing the haze at the level of particle size, distribution and geometry. We explain why the haze has these properties by virtue of the rigid-bar model of self-gravity wakes. If the purpose of the model were to describe the interior of self-gravity wakes or their overall evolution over many orbital periods, our model would be unrealistic and a misrepresentation of the target. Nevertheless, because our model is focused on the haze, the model is a good one. With this discussion, we have also answered Q.2: A2: Even if the main goal of the model was to explain the existence of the haze, it also describes the haze in some detail; the model is both explanatory and

descriptive. The description of the haze helps to explain the signal. The main explanatory work, however, is done by the part of the model with the greatest distortion: the rigid self-gravity wake, the description of the haze being a byproduct of this. Thus, while descriptive, the main role the model plays is explanatory.

4.2 The Ions in the Reconnecting Region of Earth's Magnetotial

The Plasma physics model is an idealization because it ignores the Ampere contribution to the magnetic field, and we can add this contribution back without changing any of the fundamental equations of the model. It is, however, very convenient computationally to ignore the fields generated by the ions in the simulation.

We emphasize Chapter 2 that we based the fields of our test-particle simulation on the measured turbulent magnetic and electric fields. This gives us several advantages over self-consistent models. An accurate self-consistent code must have a large range of scales, a large number of particles, as well as an accurate electron-to-ion mass ratio to reproduce the turbulent magnetic and electric fields. Self-consistent codes must have a large 3D simulation domain, long run times so that ions can pass through the system, and fully open boundaries to properly handle ion acceleration. A test-particle code can incorporate these features at the expense of self-consistent behavior. Furthermore, we are well able to constrain most of our simulation parameters by measurements: particle distributions (densities and temperatures) at boundaries as well as turbulent region size can be estimated by using data, with the exception of the length of magnetic reconnection's x-line.

In the chapter, we uniquely justified the lack of self-consistency as a matter of computational convenience. This is, of course, a frequent motivation of distortions in modeling. When we represent the target as having (or lacking) certain properties, Cartwright calls these "properties of convenience."

> A model is a work of fiction. Some properties ascribed to objects in the model will be genuine properties of the objects modelled, but others will be merely properties of convenience (...) Not all properties of convenience will be real ones. There are the obvious idealizations of physics—infinite potentials, zero time correlations, perfectly rigid rods, and frictionless planes. But it would be a mistake to think entirely in terms of idealizations—of properties which we conceive as limiting cases, to which we can approach closer and closer in reality. (Cartwright, 1983)

Cartwright specifies that these properties can be either idealizations ("limiting cases") or abstractions. Again, our distortion in Chapter 3 is an idealization, not an abstraction. This is because it is a limiting case where we have excluded the Ampere component of the magnetic field.

Distortions, however, also highlight the explanatory relevant aspects of the simulation. What are the aspects highlighted by ignoring Amperes' law? The answer to this is hinted at in the discussion of Chapter 3, and our comparisons with the magnetostatics simulation ran by Veltri et al. (1998) and Greco et al. (2002). Veltri et al. (1998) and Greco et al. (2002) did not see the power-law in the ion flux develop in their simulation, they also lacked the electrostatic component of the turbulent field. Our distortions reinforce this effect: the main explanatory cause for the ion acceleration is the electrostatic turbulent electric field. Properly computing the Ampere component due to the ion currents can change the magnetic field significantly, but the magnetic field is not the explanatory relevant cause for the phenomenon the model is attempting to reproduce. This leads us to the answer of Q.1.

A.1: The purpose of the model is to explain the power-law in the ion flux distribution. Different simulations, including self-consistent simulations, have failed to produce this power-law (Scholer et al., 2003; Zhang et al., 2021). The only previously successful studies are Perri et al. (2011) and Dolgonosov et al. (2013), but they used a highly artificial model for the fields that is not consistent with the Turbulence spectra measured by MMS and other spacecraft. Our model is hence a first attempt at reproducing an ion energy-flux power-law based on realistic fields. Since we manage to reproduce the power-law and, provide a causal account for it—namely that the ions that cross the field-reversal plane get energized preferentially and in a runaway fashion— our model is a good representation of the target, even if it doesn't strictly obey all of Maxwell's equations.

Fundamentally, the reason the ions get accelerated to such high energies is due to the Lorentz force and Newtown's Law (or even more fundamentally, due to Quantum Electrodynamics). This is of course true, but it doesn't explain anything. We must establish causal relations between the emerging macroscopic phenomena: i.e., causal relationships between integrated fluxes and the turbulent fields power spectrum, causal relationships between the average dwell time of ions and the intensity of the turbulence. To do this, it is necessary to simplify. In simplifying, we often introduce "properties of convenience" which are, strictly

speaking, false. It is in this sense that Cartwright claims that "The Truth Doesn't Explain Much." Her framework for explanation is certainly exemplified by Chapter 3. This leads us to the answer to Q.2.

A.2 Hence, the model of the plasma is of the explanatory kind. The explanation is achieved by uncovering the causal relationship between the statistical phenomena of the flux distribution and the turbulent field spectra.

4.3 A Philosophical Analysis of a Referee Report

We answered both questions for both of our models and found that both models have an explanatory purpose. Both models aim to explain how the phenomena in question (the haze and the power-law tail) come about. For this purpose, they tell a causal story of the mechanism that generates the signal measured by the spacecraft.

One may think that the conditions for these assumptions to be valid are that the self-gravity wakes are rigid in the real world and that the Ampere component of the magnetic field is small compared to the background field. Both of these are probably false, however, so how can they be a reasonable part of the model?

One of the referees for the paper based on Chapter 2 raised this issue regarding the rigidity assumption in an earlier version of the manuscript. They say of our attempt to compute the motion of self-gravity wakes via a series of torques:

> While this may be a reasonable idea, the actual calculations in Sections 2.1 and 2.2 are difficult to follow and involve a number of assumptions and approximations that may not be valid. (emphasis by the author)

We agreed with the referee that there's a sense in which the rigidity assumption may not be valid. The wakes are certainly not perfectly rigid as we assume them to be in Chapter 2; they may not even be pseudo-rigid. Nevertheless, the rigidity assumption can be applied to situations where these strict validity conditions do not hold, insofar as they still capture a type of behavior that does hold. Our claim is that the rigidity assumption, even if false, properly reproduces the interplay between the different influences affecting the orientation of the self-gravity wake. We claim that these causes are real, even though the

rigidity is not. Cartwright's emphasis on the behavior of entities can shine some light on how the rigidity assumption can be a good one to use even if the wakes themselves are not rigid. The assumption is valid, in a different sense, if it helps to explain the behavior of certain causal interactions to orient the self-gravity wake at different angles.

> To ascribe a behavior to the nature of a feature is to claim that the behavior is exportable beyond the strict confinement of the *ceteris paribus*[1] conditions, although usually only as a "tendency" or a "trying." (Cartwright, 1999)

Our claim is then not that the wakes are rigid, but that the tidal and shear interactions tend to orient the wakes radially and azimuthally respectively: the equilibrium pitch angle arising for a balancing of these tendencies. This statement is not new, it was already suggested by the N-body simulations performed by Michikoshi et al. (2015). The rigidity assumption allows us to give a simple, analytical expression to that tendency. Hence, we "ascribe a behavior," to the "nature" of Tidal forces and shear interactions, which, for Cartwright, amounts to claiming that we can export the behavior beyond the *ceteris paribus* conditions (the rigidity of the self-gravity wakes). In other words, the balance of the tidal and shear interactions can be exported beyond the rigidity assumption, and hence beyond the assumption used to derive the balance equation, insofar these interactions still determine the pitch-angle of non-rigid self-gravity wakes.

Our ability to fit the data, however, gave the reviewer confidence that our main thesis was correct.

> Let me be clear that I have no reason to doubt the basic result of this paper, that the observed properties of the Mimas 5:3 bending wave can be reasonably well fit by a model that includes an extra particle population whose density scales with the slopes of the bending wave. The authors provide reasonable evidence that this is the case, and this finding alone would represent a significant advance in our understanding of these waves, since it provides clear evidence that the wave is having an effect on the ring's microstructure.

Many of the philosophical discussions in this thesis are encapsulated in this reviewer's report. A superficial read of this passage may suggest that the reviewer is justifying the publication of the model merely by its ability to fit the data. But at the end of the paragraph one can see that we managed to give some reasonable credence to the idea that this haze of particles came from self-gravity wakes (what he calls

[1] Meaning: all other things being equal. That is, that the relevant conditions under which the assumptions hold.

the "microstructure.") Moreover, they says that the model represents an advance in our understanding since it offers this origin story for the signal. Even with the possibly invalid assumption, we managed to make a good enough explanation for the origin of this haze by providing a causal mechanism based on the dynamics of rigid bodies. Our causal story, however, cannot be told without the distortions. The important lesson is that one can believe in the causal mechanism while being skeptical of the rigidity of self-gravity wakes.

4.4 Final Conclusions

This discussion gives a concrete example of the role of models in science, and how abstractions can be used to produce an understanding that "perfectly" detailed models may fail to do. Nancy Cartwright's point in The Truth Doesn't Explain Much, is that in the case of explanation, too complicated of a model may obfuscate the explanatorily relevant factors in the system. Due to the explanatory nature of models, hence, one-to-one, part-by-part representation is not often what we are after when modeling.

Abstractions like the rigid-bar assumption are present in many instances of science. This is the reason why Margaret Morrison reminds us that the issue of representation "is not simply one of picturing." In the case of quantum field theory we model the field as a collection of harmonic oscillators in order to get a Hamiltonian that give the correct structure to the allowed energies. But, Cartwright points out, this does not commit us to the existence of a set of objects behaving like springs. (Morrison, 2009b)

Harmonic oscillators are a powerful tool in modeling quantum systems, due to being one of the few problems we have solved analytically in its entirety and given that many Hamiltonians can be constructed with it. Using these models doesn't commit us to believe that what's really going on in these quantum systems is that there are quantum harmonic oscillators everywhere in the quantum field. In the same way, our rigid-bar model does not commit us to the rigidity of the self-gravity wakes.

At first, one may believe that there are only two questions one may ask of a model: Is the model getting all parts of the system at least approximately right? Is it consistent with the data? While asking these questions is useful when evaluating the model, one must understand what the main purpose of the model is. Or, in the language of Reviewer 1, we must always ask: "what is the basic result of the paper?" And then ask: "and how does the model serve this result?" Models should not be simply evaluated by whether they

accurately, one-to-one, mirror the targeted system. If we think of models as an image, as we did at the start of the introduction, then this point was made twenty-five hundred years ago by Plato (Plato, ca. 390 B.C).

Speaking of representation, Socrates attempts to rebut Cratylus' notion that representation must be one-to-one in order to be an image of the real object at all. Socrates answers:

> SOCRATES: Let us suppose the existence of two objects: one of them shall be Cratylus, and the other the image of Cratylus; and we will suppose, further, that some God makes not only a representation such as a painter would make of your outward form and colour, but also creates an inward organization like yours, having the same warmth and softness; and into this infuses motion, and soul, and mind, such as you have, and in a word copies all your qualities, and places them by you in another form; would you say that this was Cratylus and the image of Cratylus, or that there were two Cratyluses?
>
> CRATYLUS: I should say that there were two Cratyluses.
>
> SOCRATES: Then you see, my friend, that we must find some other principle of truth in images [other than one-to-one representation], and also in names; and not insist that an image is no longer an image when something is added or subtracted. Do you not perceive that images are very far from having qualities which are the exact counterpart of the realities which they represent?
>
> CRATYLUS: Yes, I see. (*Cratylus 432a-d*)

We must, hence, find some other "principle of truth" of models other than one-to-one representation, and not insist that a model is bad just because it lacks certain components we know to be there in the real world, or because it is unrealistic in a particular way. The goodness and badness of a model must always be evaluated relative to its purpose and the context in which it was created.

Bibliography

Acton, C., Bachman, N., Semenov, B., & Wright, E., 2018, A look towards the future in the handling of space science mission geometry, *Planetary and Space Science*, 150, 9–12. Enabling Open and Interoperable Access to Planetary Science and Heliophysics Databases and Tools.
URL: *https://www.sciencedirect.com/science/article/pii/S0032063316303129*

Acton, C. H., 1996, Ancillary data services of nasa's navigation and ancillary information facility, *Planetary and Space Science*, 44, 65–70.

Angelopoulos, V., Kennel, C. F., Coroniti, F. V., Pellat, R., Kivelson, M. G., Walker, R. J., Russell, C. T., Baumjohann, W., Feldman, W. C., & Gosling, J. T., 1994, Statistical characteristics of bursty bulk flow events, *J. Geophys. Res.*, 99(A11), 21257–21280.

Arfken, G. B. & Weber, H. J., 2005, *Mathematical methods for physicists 6th ed.*

Armitage, P. J., 2020, *Astrophysics of Planet Formation*, 2 edn, Cambridge University Press.

Artemyev, A. V., Petrukovich, A. A., Nakamura, R., & Zelenyi, L. M., 2010, Proton velocity distribution in thin current sheets: Cluster observations and theory of transient trajectories, *Journal of Geophysical Research: Space Physics*, 115(A12).
URL: *https://agupubs.onlinelibrary.wiley.com/doi/abs/10.1029/2010JA015702*

Artemyev, A. V., Zelenyi, L. M., Malova, H. V., Zimbardo, G., & Delcourt, D., 2009, Acceleration and transport of ions in turbulent current sheets: formation of non-maxwelian energy distribution, *Nonlinear*

Processes in Geophysics, 16(6), 631–639.

URL: *https://npg.copernicus.org/articles/16/631/2009/*

Baumjohann, W., Paschmann, G., & Cattell, C. A., 1989, Average plasma properties in the central plasma sheet, *J. Geophys. Res.*, 94(A6), 6597–6606.

Bertin, G. & Mark, J. W. K., 1980, On the excitation of WARPS in galaxy disks, *A&A*, 88(3), 289–297.

Binney, J. & Tremaine, S., 2008, *Galactic Dynamics: Second Edition*, Princeton University Press.

Blake, J. B., Mauk, B. H., Baker, D. N., Carranza, P., Clemmons, J. H., Craft, J., Crain, W. R., Crew, A., Dotan, Y., Fennell, J. F., Friedel, R. H., Friesen, L. M., Fuentes, F., Galvan, R., Ibscher, C., Jaynes, A., Katz, N., Lalic, M., Lin, A. Y., Mabry, D. M., Nguyen, T., Pancratz, C., Redding, M., Reeves, G. D., Smith, S., Spence, H. E., & Westlake, J., 2016, The fly's eye energetic particle spectrometer (feeps) sensors for the magnetospheric multiscale (mms) mission, *Space Science Reviews*, 199(1), 309–329.

URL: *https://doi.org/10.1007/s11214-015-0163-x*

Blandford, R. & Eichler, D., 1987, Particle acceleration at astrophysical shocks: A theory of cosmic ray origin, *Phys. Rep.*, 154(1), 1–75.

Bodrova, A., Schmidt, J., Spahn, F., & Brilliantov, N., 2012, Adhesion and collisional release of particles in dense planetary rings, *Icarus*, 218(1), 60–68.

Borderies, N., Goldreich, P., & Tremaine, S., 1986, Nonlinear density waves in planetary rings, *Icarus*, 68(3), 522–533.

URL: *https://www.sciencedirect.com/science/article/pii/0019103586900540*

Borges, J. L., 2018, *Del Rigor en La Ciencia. Retrieved from Ciudad Seva*, Ciudad Seva, Del Rigor en La Ciencia.

URL: *http://ciudadseva.com/texto/del-rigor-en-la-ciencia/*

Boris, J. P., 1970, *The Acceleration Calculation from a Scalar Potential*, Plasma Physics Laboratory Report

MATT-769, 1st edn, Princeton University Press.

URL: *https://www.osti.gov/biblio/4168374*

Borovsky, J. E., Elphic, R. C., Funsten, H. O., & Thomsen, M. F., 1997, The Earth's plasma sheet as a laboratory for flow turbulence in high-[beta] MHD, *Journal of Plasma Physics*, 57(1), 1–34.

Brisset, J., Colwell, J., Dove, A., Abukhalil, S., Cox, C., & Mohammed, N., 2018, Regolith behavior under asteroid-level gravity conditions: low-velocity impact experiments, *Progress in Earth and Planetary Science*, 5(1), 73.

Brouwer, D. & Clemence, G., 1961, *Methods of Celestial Mechanics*, Academic Press.

URL: *http://www.sciencedirect.com/science/article/pii/B9781483200750500034*

Cartwright, N., 1980, The truth doesn't explain much, *American Philosophical Quartly*, pp. 159–163.

Cartwright, N., 1983, 143The Simulacrum Account of Explanation, *How the Laws of Physics Lie*, Oxford University Press.

URL: *https://doi.org/10.1093/0198247044.003.0009*

Cartwright, N., 1999, *The Dappled World: A Study of the Boundaries of Science*, Cambridge University Press.

Chakrabarti, S. K., 1988, On the damping of the bending waves in saturn's ring, *Journal of Astrophysics and Astronomy*, 9(4), 243–248.

URL: *https://doi.org/10.1007/BF02715070*

Chakrabarti, S. K., 1989, The dynamics of particles in the bending waves of planetary rings, *MNRAS*, 238, 1381–1394.

Chandrasekhar, S., 1942, *Principles of stellar dynamics.*

Christon, S. P., Williams, D. J., Mitchell, D. G., Huang, C. Y., & Frank, L. A., 1991, Spectral characteristics of plasma sheet ion and electron populations during disturbed geomagnetic conditions, *Journal of Geo-*

physical Research: Space Physics, 96(A1), 1–22.

URL: *https://agupubs.onlinelibrary.wiley.com/doi/abs/10.1029/90JA01633*

Cohen, I. J., Mitchell, D. G., Kistler, L. M., Mauk, B. H., Anderson, B. J., Westlake, J. H., Ohtani, S., Hamilton, D. C., Turner, D. L., Blake, J. B., Fennell, J. F., Jaynes, A. N., Leonard, T. W., Gerrard, A. J., Lanzerotti, L. J., Allen, R. C., & Burch, J. L., 2017, Dominance of high-energy (¿150 kev) heavy ion intensities in earth's middle to outer magnetosphere, *Journal of Geophysical Research: Space Physics*, 122(9), 9282–9293.

URL: *https://agupubs.onlinelibrary.wiley.com/doi/abs/10.1002/2017JA024351*

Colombo, G., Goldreich, P., & Harris, A. W., 1976, Spiral structure as an explanation for the asymmetric brightness of Saturn's A ring, *Nature*, 264, 344.

Colwell, J. E., Esposito, L. W., & Sremčević, M., 2006, Self-gravity wakes in saturn's a ring measured by stellar occultations from cassini, *Geophysical Research Letters*, 33(7).

URL: *https://agupubs.onlinelibrary.wiley.com/doi/abs/10.1029/2005GL025163*

Colwell, J. E., Esposito, L. W., Jerousek, R. G., Sremčević, M., Pettis, D., & Bradley, E. T., 2010, Cassini UVIS Stellar Occultation Observations of Saturn's Rings, *AJ*, 140(6), 1569–1578.

Colwell, J., Sture, S., Cintala, M., Durda, D., Hendrix, A., Goudie, T., Curtis, D., Ashcom, D., Kanter, M., Keohane, T., Lemos, A., Lupton, M., & Route, M., 2008, Ejecta from impacts at 0.2–2.3 m/s in low gravity, *Icarus*, 195, 908–917.

Cook, A. F. & Franklin, F. A., 1964, Rediscussion of Maxwell's ADAMS Prize Essay on the stability of Saturn S rings, *AJ*, 69, 173.

Cuzzi, J. N., Durisen, R. H., Burns, J. A., & Hamill, P., 1979, The Vertical Structure and Thickness of Saturn's Rings, *Icarus*, 38(1), 54–68.

Daisaka, H. & Ida, S., 1999, Spatial structure and coherent motion in dense planetary rings induced by self-

gravitational instability, *Earth, Planets and Space*, 51(11), 1195–1213.

URL: *https://doi.org/10.1186/BF03351594*

Davis, L., 1956, Modified fermi mechanism for the acceleration of cosmic rays, *Phys. Rev.*, 101, 351–358.

URL: *https://link.aps.org/doi/10.1103/PhysRev.101.351*

DeCoster, R. & Frank, L., 1979, Observations pertaining to the dynamics of the plasma sheet, *Journal of Geophysical Research: Space Physics*, 84(A9), 5099–5121.

URL: *https://agupubs.onlinelibrary.wiley.com/doi/abs/10.1029/JA084iA09p05099*

Dolgonosov, M. S., Zimbardo, G., Perri, S., & Greco, A., 2013, On the generation of ion beamlets in the magnetotail: Resonant acceleration versus stochastic acceleration, *Journal of Geophysical Research: Space Physics*, 118(9), 5445–5453.

URL: *https://agupubs.onlinelibrary.wiley.com/doi/abs/10.1002/jgra.50490*

Dones, L. & Porco, C. C., 1989, Spiral Density Wakes in Saturn's A Ring?, *Bulletin of the American Astronomical Society*, Vol. 21, p. 929.

Drake, J. F., Swisdak, M., Che, H., & Shay, M. A., 2006, Electron acceleration from contracting magnetic islands during reconnection, *Nature*, 443(7111), 553–556.

URL: *https://doi.org/10.1038/nature05116*

Dunn, D. E., Molnar, L. A., Niehof, J. T., de Pater, I., & Lissauer, J. J., 2004, Microwave observations of saturn's rings: anisotropy in directly transmitted and scattered saturnian thermal emission, *Icarus*, 171(1), 183–198.

URL: *https://www.sciencedirect.com/science/article/pii/S0019103504001356*

Epstein-Martin, M., Becker, J., & Batygin, K., 2022, Generating stellar obliquity in systems with broken protoplanetary disks, *The Astrophysical Journal*, 931(1), 42.

URL: *https://dx.doi.org/10.3847/1538-4357/ac5b79*

Ergun, R. E., Ahmadi, N., Kromyda, L., Schwartz, S. J., Chasapis, A., Hoilijoki, S., Wilder, F. D., Cassak,

P. A., Stawarz, J. E., Goodrich, K. A., Turner, D. L., Pucci, F., Pouquet, A., Matthaeus, W. H., Drake, J. F., Hesse, M., Shay, M. A., Torbert, R. B., & Burch, J. L., 2020a, Particle acceleration in strong turbulence in the earth's magnetotail, *The Astrophysical Journal*, 898(2), 153.

URL: *https://dx.doi.org/10.3847/1538-4357/ab9ab5*

Ergun, R. E., Ahmadi, N., Kromyda, L., Schwartz, S. J., Chasapis, A., Hoilijoki, S., Wilder, F. D., Stawarz, J. E., Goodrich, K. A., Turner, D. L., Cohen, I. J., Bingham, S. T., Holmes, J. C., Nakamura, R., Pucci, F., Torbert, R. B., Burch, J. L., Lindqvist, P.-A., Strangeway, R. J., Contel, O. L., & Giles, B. L., 2020b, Observations of particle acceleration in magnetic reconnection–driven turbulence, *The Astrophysical Journal*, 898(2), 154.

URL: *https://dx.doi.org/10.3847/1538-4357/ab9ab6*

Ergun, R. E., Andersson, L. A., Fowler, C. M., & Thaller, S. A., 2021, Kinetic modeling of langmuir probes in space and application to the maven langmuir probe and waves instrument, *Journal of Geophysical Research: Space Physics*, 126(3), e2020JA028956. e2020JA028956 2020JA028956.

URL: *https://agupubs.onlinelibrary.wiley.com/doi/abs/10.1029/2020JA028956*

Ergun, R. E., Goodrich, K. A., Wilder, F. D., Ahmadi, N., Holmes, J. C., Eriksson, S., Stawarz, J. E., Nakamura, R., Genestreti, K. J., Hesse, M., Burch, J. L., Torbert, R. B., Phan, T. D., Schwartz, S. J., Eastwood, J. P., Strangeway, R. J., Le Contel, O., Russell, C. T., Argall, M. R., Lindqvist, P.-A., Chen, L. J., Cassak, P. A., Giles, B. L., Dorelli, J. C., Gershman, D., Leonard, T. W., Lavraud, B., Retino, A., Matthaeus, W., & Vaivads, A., 2018, Magnetic reconnection, turbulence, and particle acceleration: Observations in the earth's magnetotail, *Geophysical Research Letters*, 45(8), 3338–3347.

URL: *https://agupubs.onlinelibrary.wiley.com/doi/abs/10.1002/2018GL076993*

Ergun, R. E., Malaspina, D. M., Bale, S. D., Mcfadden, J. P., Larson, D. E., Mozer, F. S., Meyer-Vernet, N., Maksimović, M., Kellogg, P. J., & Wygant, J. R., 2010, Spacecraft charging and ion wake formation in the near-sun environment, *Physics of Plasmas*, 17, 072903.

Ergun, R. E., Usanova, M. E., Turner, D. L., & Stawarz, J. E., 2022, Bursty bulk flow turbulence as a source

of energetic particles to the outer radiation belt, *Geophysical Research Letters*, 49(11), e2022GL098113. e2022GL098113 2022GL098113.

URL: *https://agupubs.onlinelibrary.wiley.com/doi/abs/10.1029/2022GL098113*

Esposito, L., O'Callaghan, M., & West, R., 1983, The structure of saturn's rings: Implications from the voyager stellar occultation, *Icarus*, 56(3), 439 – 452.

URL: *http://www.sciencedirect.com/science/article/pii/0019103583901653*

Esposito, L. W., Barth, C. A., Colwell, J. E., Lawrence, G. M., McClintock, W. E., Stewart, A. I. F., Keller, H. U., Korth, A., Lauche, H., Festou, M. C., Lane, A. L., Hansen, C. J., Maki, J. N., West, R. A., Jahn, H., Reulke, R., Warlich, K., Shemansky, D. E., & Yung, Y. L., 2004, The Cassini Ultraviolet Imaging Spectrograph Investigation, *Space Sci. Rev.*, 115(1-4), 299–361.

Fermi, E., 1949, On the origin of the cosmic radiation, *Phys. Rev.*, 75, 1169–1174.

URL: *https://link.aps.org/doi/10.1103/PhysRev.75.1169*

Greco, A., Perri, S., Zimbardo, G., & Zelenyi, L., 2009, Particle acceleration by stochastic fluctuations and dawn-dusk electric field in the earth's magnetotail, *Advances in Space Research*, 44(4), 528–533.

URL: *https://www.sciencedirect.com/science/article/pii/S0273117709003524*

Greco, A., Taktakishvili, A. L., Zimbardo, G., Veltri, P., & Zelenyi, L. M., 2002, Ion dynamics in the near-earth magnetotail: Magnetic turbulence versus normal component of the average magnetic field, *Journal of Geophysical Research: Space Physics*, 107(A10), SMP 1–1–SMP 1–16.

URL: *https://agupubs.onlinelibrary.wiley.com/doi/abs/10.1029/2002JA009270*

Greenberg, R., Bottke, W. F., Carusi, A., & Valsecchi, G. B., 1991, Planetary accretion rates: Analytical derivation, *Icarus*, 94(1), 98–111.

Gresh, D. L., Rosen, P. A., Leonard Tyler, G., & Lissauer, J. J., 1986, An analysis of bending waves in saturn's rings using voyager radio occultation data, *Icarus*, 68(3), 481 – 502.

URL: *http://www.sciencedirect.com/science/article/pii/0019103586900527*

Griffiths, D. J., 2013, *Introduction to electrodynamics; 4th ed.*, Pearson, Boston, MA. Re-published by Cambridge University Press in 2017.

URL: *https://cds.cern.ch/record/1492149*

Grigorenko, E. E., Hoshino, M., Hirai, M., Mukai, T., & Zelenyi, L. M., 2009, "geography" of ion acceleration in the magnetotail: X-line versus current sheet effects, *Journal of Geophysical Research: Space Physics*, 114(A3).

URL: *https://agupubs.onlinelibrary.wiley.com/doi/abs/10.1029/2008JA013811*

Haaland, S., Kronberg, E. A., Daly, P. W., Fränz, M., Degener, L., Georgescu, E., & Dandouras, I., 2010, Spectral characteristics of protons in the earth's plasmasheet: statistical results from cluster cis and rapid, *Annales Geophysicae*, 28(8), 1483–1498.

URL: *https://angeo.copernicus.org/articles/28/1483/2010/*

Harbison, R. A., Nicholson, P. D., & Hedman, M. M., 2013, The smallest particles in saturn's a and c rings, *Icarus*, 226(2), 1225–1240.

URL: *https://www.sciencedirect.com/science/article/pii/S0019103513003539*

Hedman, M. M., Nicholson, P. D., Salo, H., Wallis, B. D., Buratti, B. J., Baines, K. H., Brown, R. H., & Clark, R. N., 2007, Self-Gravity Wake Structures in Saturn's A Ring Revealed by Cassini VIMS, *AJ*, 133(6), 2624–2629.

Hill, G. W., 1878, Researches in the lunar theory, *American Journal of Mathematics*, 1(1), 5–26.

URL: *http://www.jstor.org/stable/2369430*

Husserl, E., 1913, Counsciosness as intentional experience, *Logical Investigations*, Routletdge, p. 578.

Iess, L., Militzer, B., Kaspi, Y., Nicholson, P., Durante, D., Racioppa, P., Anabtawi, A., Galanti, E., Hubbard, W., Mariani, M. J., Tortora, P., Wahl, S., & Zannoni, M., 2019, Measurement and implications of saturn’s gravity field and ring mass, *Science*, 364(6445), eaat2965.

URL: *https://www.science.org/doi/abs/10.1126/science.aat2965*

Jacobson, R., 2010, Jpl satellite ephemeris sat 339, , .

URL: *http://ssd.jpl.nasa.gov*

Jacobson, R. A., Antreasian, P. G., Bordi, J. J., Criddle, K. E., Ionasescu, R., Jones, J. B., Mackenzie, R. A., Meek, M. C., Parcher, D., Pelletier, F. J., Owen, W. M., J., Roth, D. C., Roundhill, I. M., & Stauch, J. R., 2006, The Gravity Field of the Saturnian System from Satellite Observations and Spacecraft Tracking Data, *AJ*, 132(6), 2520–2526.

Jerousek, R., 2018, *Determining the Small-scale Structure and Particle Properties in Saturn's Rings from Stellar and Radio Occultations*, PhD thesis, University of Central Florida.

URL: *https://stars.library.ucf.edu/etd/5840*

Jerousek, R. G., Colwell, J. E., Esposito, L. W., Nicholson, P. D., & Hedman, M. M., 2016, Small particles and self-gravity wakes in Saturn's rings from UVIS and VIMS stellar occultations, *Icarus*, 279, 36–50.

Karjalainen, R. & Salo, H., 2004, Gravitational accretion of particles in saturn's rings, *Icarus*, 172(2), 328–348.

URL: *https://www.sciencedirect.com/science/article/pii/S0019103504002052*

Keiling, A., Rème, H., Dandouras, I., Bosqued, J. M., Sergeev, V., Sauvaud, J.-A., Jacquey, C., Lavraud, B., Louarn, P., Moreau, T., Vallat, C., Escoubet, C. P., Parks, G. K., McCarthy, M., Möbius, E., Amata, E., Klecker, B., Korth, A., Lundin, R., Daly, P., & Zong, Q.-G., 2004, New properties of energy-dispersed ions in the plasma sheet boundary layer observed by cluster, *Journal of Geophysical Research: Space Physics*, 109(A5).

URL: *https://agupubs.onlinelibrary.wiley.com/doi/abs/10.1029/2003JA010277*

Kolmogorov, A. N., 1991, The local structure of turbulence in incompressible viscous fluid for very large reynolds numbers, *Proceedings: Mathematical and Physical Sciences*, 434(1890), 9–13.

URL: *http://www.jstor.org/stable/51980*

Lewis, D., 1973, Causation, *Journal of Philosophy*, pp. 556–567.

Lissauer, J. J., Shu, F. H., & Cuzzi, J. N., 1984, Viscosity in Saturn's Rings, *in* Brahic, A. (ed.), *Planetary Rings*, p. 385.

Litvinenko, Y. E. & Somov, B. V., 1993, Particle acceleration in reconnecting current sheets, *Solar Physics*, 146(1), 127–133.
URL: *https://doi.org/10.1007/BF00662174*

Lu, Y., Ballouz, R.-L., & Richardson, D. C., 2018, Exploring shear-free ringlet formation with direct simulations of saturn's b rings, *The Astronomical Journal*, 156(3), 129.

Lynden-Bell, D. & Pringle, J. E., 1974, The evolution of viscous discs and the origin of the nebular variables., *MNRAS*, 168, 603–637.

Lyra, W., Turner, N. J., & McNally, C. P., 2015, Rossby wave instability does not require sharp resistivity gradients, *A&A*, 574, A10.
URL: *https://doi.org/10.1051/0004-6361/201424919*

Marchand, R., Miyake, Y., Usui, H., Deca, J., Lapenta, G., Matéo-Vélez, J. C., Ergun, R. E., Sturner, A., Génot, V., Hilgers, A., & Markidis, S., 2014, Cross-comparison of spacecraft-environment interaction model predictions applied to solar probe plus near perihelion, *Physics of Plasmas*, 21(6), 062901.
URL: *https://doi.org/10.1063/1.4882439*

Michikoshi, S., Fujii, A., Kokubo, E., & Salo, H., 2015, Dynamics of Self-gravity Wakes in Dense Planetary Rings. I. Pitch Angle, *ApJ*, 812(2), 151.

Miller, J. A., Larosa, T. N., & Moore, R. L., 1996, Stochastic Electron Acceleration by Cascading Fast Mode Waves in Impulsive Solar Flares, *ApJ*, 461, 445.

Morishima, R. & Salo, H., 2004, Spin rates of small moonlets embedded in planetary rings: I. three-body calculations, *Icarus*, 167(2), 330–346.
URL: *https://www.sciencedirect.com/science/article/pii/S0019103503003294*

Morrison, M., 2009a, Fictions, representations, and reality, *in* Suárez, M. (ed.), *Fictions in Science: Philosophical Essays on Modeling and Idealization*, Routledge, pp. 4–110.

Morrison, M., 2009b, Models as representational structures, *Nancy Cartwright's Philosophy of Science*, Routledge.

Murray, C. D. & Dermott, S. F., 2000, *Solar System Dynamics*, Cambridge University Press.

Nakamura, R., Baumjohann, W., Mouikis, C., Kistler, L. M., Runov, A., Volwerk, M., Asano, Y., Vörös, Z., Zhang, T. L., Klecker, B., Rème, H., & Balogh, A., 2004, Spatial scale of high-speed flows in the plasma sheet observed by Cluster, *Geophys. Res. Lett.*, 31(9), L09804.

Nelson, R. W. & Tremaine, S., 1995, The damping and excitation of galactic warps by dynamical friction, *MNRAS*, 275(4), 897–920.

Nicholson, P. D. & Hedman, M. M., 2016, A vertical rift in Saturn's inner C ring, *Icarus*, 279, 78–99.

Papaloizou, J. C. B. & Pringle, J. E., 1985, The dynamical stability of differentially rotating discs â€“ II, *Monthly Notices of the Royal Astronomical Society*, 213(4), 799–820.
URL: *https://doi.org/10.1093/mnras/213.4.799*

Perri, S., Zimbardo, G., & Greco, A., 2011, On the energization of protons interacting with 3-d time-dependent electromagnetic fields in the earth's magnetotail, *Journal of Geophysical Research: Space Physics*, 116(A5).
URL: *https://agupubs.onlinelibrary.wiley.com/doi/abs/10.1029/2010JA016328*

Peters, M. & Babee, H., 2020, Counterfactual theories of causation, *Stanford Encyclopedia of Philosophy*, Stanford.

Plato, ca. 390 B.C, *Cratylus*, Jeffferson Publication.

Pollock, C., Moore, T., Jacques, A., Burch, J., Gliese, U., Saito, Y., Omoto, T., Avanov, L., Barrie, A., Coffey, V., Dorelli, J., Gershman, D., Giles, B., Rosnack, T., Salo, C., Yokota, S., Adrian, M., Aoustin, C.,

Auletti, C., Aung, S., Bigio, V., Cao, N., Chandler, M., Chornay, D., Christian, K., Clark, G., Collinson, G., Corris, T., De Los Santos, A., Devlin, R., Diaz, T., Dickerson, T., Dickson, C., Diekmann, A., Diggs, F., Duncan, C., Figueroa-Vinas, A., Firman, C., Freeman, M., Galassi, N., Garcia, K., Goodhart, G., Guererro, D., Hageman, J., Hanley, J., Hemminger, E., Holland, M., Hutchins, M., James, T., Jones, W., Kreisler, S., Kujawski, J., Lavu, V., Lobell, J., LeCompte, E., Lukemire, A., MacDonald, E., Mariano, A., Mukai, T., Narayanan, K., Nguyan, Q., Onizuka, M., Paterson, W., Persyn, S., Piepgrass, B., Cheney, F., Rager, A., Raghuram, T., Ramil, A., Reichenthal, L., Rodriguez, H., Rouzaud, J., Rucker, A., Samara, M., Sauvaud, J.-A., Schuster, D., Shappirio, M., Shelton, K., Sher, D., Smith, D., Smith, K., Smith, S., Steinfeld, D., Szymkiewicz, R., Tanimoto, K., Taylor, J., Tucker, C., Tull, K., Uhl, A., Vloet, J., Walpole, P., Weidner, S., White, D., Winkert, G., Yeh, P.-S., & Zeuch, M., 2016, Fast plasma investigation for magnetospheric multiscale, *Space Science Reviews*, 199(1), 331–406.

URL: *https://doi.org/10.1007/s11214-016-0245-4*

Porco, C. C., Thomas, P. C., Weiss, J. W., & Richardson, D. C., 2007, Saturn's Small Inner Satellites: Clues to Their Origins, *Science*, 318(5856), 1602.

Press, W. H., Teukolsky, S. A., Vetterling, W. T., & Flannery, B. P., 2007, *Numerical Recipes: The Art of Scientific Computing*, 3 edn, Cambridge University Press.

Rafikov, R. R., 2004, Fast accretion of small planetesimals by protoplanetary cores, *The Astronomical Journal*, 128(3), 1348–1363.

URL: *https://doi.org/10.1086/423216*

Rehnberg, M. E., Brown, Z. L., Esposito, L. W., & Albers, N., 2017, Direct detection of gaps in saturn's a ring, *Icarus*, 297, 110–118.

URL: *https://www.sciencedirect.com/science/article/pii/S0019103516306923*

Rein, H. & Liu, S. F., 2012, REBOUND: an open-source multi-purpose N-body code for collisional dynamics, *A&A*, 537, A128.

Rowther, S., Nealon, R., & Meru, F., 2022, Warping away gravitational instabilities in protoplanetary discs,

The Astrophysical Journal, 925(2), 163.

URL: *https://doi.org/10.3847/1538-4357/ac3975*

Russell, C., Luhmann, J., & Strangeway, R., 2016, *Space Physics: An Introduction*, Cambridge University Press.

Salmon, W. C., 1984, *Scientific Explanation and the Causal Structure of the World*, Princeton University Press.

URL: *http://www.jstor.org/stable/j.ctv173f2gh*

Salo, H., 1992, Gravitational wakes in saturn's rings, *Nature*, 359(6396), 619–621.

URL: *https://doi.org/10.1038/359619a0*

Salo, H., Ohtsuki, K., & Lewis, M. C., 2018, *Computer Simulations of Planetary Rings*, Cambridge Planetary Science, Cambridge University Press, p. 434–493.

Scholer, M., Sidorenko, I., Jaroschek, C. H., Treumann, R. A., & Zeiler, A., 2003, Onset of collisionless magnetic reconnection in thin current sheets: Three-dimensional particle simulations, *Physics of Plasmas*, 10(9), 3521–3527.

URL: *https://doi.org/10.1063/1.1597494*

Sega Neuman, D. D., Esposito, L. W., & Colwell, J. E., 2019, A Non-linear Model for the Mimas 5:3 Bending Wave Including Self-gravity Wakes., *AGU Fall Meeting Abstracts*, Vol. 2019, pp. P23C–3506.

Shu, F. H., 1984a, Waves in planetary rings, *in* Greenberg, R. & Brahic, A. (eds), *IAU Colloq. 75: Planetary Rings*, pp. 513–561.

Shu, F. H., 1984b, Waves in planetary rings, *in* Greenberg, R. & Brahic, A. (eds), *IAU Colloq. 75: Planetary Rings*, pp. 513–561.

Shu, F. H., Cuzzi, J. N., & Lissauer, J. J., 1983, Bending waves in saturn's rings, *Icarus*, 53(2), 185 – 206.

URL: *http://www.sciencedirect.com/science/article/pii/0019103583901410*

Somov, B. V., 2013, *Chapter 11: Particle Acceleration in Current Layers*, Astrophysics and Space Science Library, 2nd edn, Springer.

Speiser, T. W., 1965, Particle trajectories in model current sheets: 1. analytical solutions, *Journal of Geophysical Research (1896-1977)*, 70(17), 4219–4226.
URL: *https://agupubs.onlinelibrary.wiley.com/doi/abs/10.1029/JZ070i017p04219*

Stewart, S. T. & Leinhardt, Z. M., 2009, Velocity-Dependent Catastrophic Disruption Criteria for Planetesimals, *ApJ*, 691(2), L133–L137.

Tajeddine, R., Nicholson, P. D., Longaretti, P.-Y., Moutamid, M. E., & Burns, J. A., 2017, What confines the rings of saturn?, *The Astrophysical Journal Supplement Series*, 232(2), 28.
URL: *https://dx.doi.org/10.3847/1538-4365/aa8c09*

Takeda, T. & Ida, S., 2001, Angular Momentum Transfer in a Protolunar Disk, *ApJ*, 560(1), 514–533.

Taktakishvili, A., Lopez, R., Zelenyi, L., Greco, A., Zimbardo, G., & Veltri, P., 2003, Ion dynamics in the magnetotail current sheet: opposite effects of magnetic turbulence and normal component, *Journal of Atmospheric and Solar-Terrestrial Physics*, 65(3), 315–322.
URL: *https://www.sciencedirect.com/science/article/pii/S1364682602002961*

Thomas, J. K., Charles, P. A., Buckley, D. A. H., Kotze, M. M., Lasota, J.-P., Potter, S. B., Steiner, J. F., & Paice, J. A., 2021, Large optical modulations during 2018 outburst of MAXIÂ J1820Â +Â 070 reveal evolution of warped accretion disc through X-ray state change, *Monthly Notices of the Royal Astronomical Society*, 509(1), 1062–1074.
URL: *https://doi.org/10.1093/mnras/stab3033*

Tiscareno, M., Perrine, R., Richardson, D., Hedman, M., Weiss, J., Porco, C., & Burns, J., 2010, An analytic parameterization of self-gravity wakes in saturn's rings, with application to occultations and propellers, *The Astronomical Journal*, 139, 492.

Tiscareno, M. S., Burns, J. A., Nicholson, P. D., Hedman, M. M., & Porco, C. C., 2007, Cassini imaging

of Saturn's rings. II. A wavelet technique for analysis of density waves and other radial structure in the rings, *Icarus*, 189(1), 14–34.

Tiscareno, M. S., Hedman, M. M., Burns, J. A., & Castillo-Rogez, J., 2013, COMPOSITIONS AND ORIGINS OF OUTER PLANET SYSTEMS: INSIGHTS FROM THE ROCHE CRITICAL DENSITY, *The Astrophysical Journal*, 765(2), L28.
URL: *https://doi.org/10.1088/2041-8205/765/2/l28*

Toomre, A., 1964, On the gravitational stability of a disk of stars., *ApJ*, 139, 1217–1238.

Usanova, M. E. & Ergun, R. E., 2022, Electron energization by high-amplitude turbulent electric fields: A possible source of the outer radiation belt, *Journal of Geophysical Research: Space Physics*, 127(7), e2022JA030336. e2022JA030336 2022JA030336.
URL: *https://agupubs.onlinelibrary.wiley.com/doi/abs/10.1029/2022JA030336*

Van Fraassen, B., 2008, *Scientific Representation*, Oxford University Press, Oxford.

Veltri, P., Zimbardo, G., Taktakishvili, A. L., & Zelenyi, L. M., 1998, Effect of magnetic turbulence on the ion dynamics in the distant magnetotail, *Journal of Geophysical Research: Space Physics*, 103(A7), 14897–14910.
URL: *https://agupubs.onlinelibrary.wiley.com/doi/abs/10.1029/98JA00211*

Yasui, Y., Ohtsuki, K., & Daisaka, H., 2014, GRAVITATIONAL ACCRETION OF PARTICLES ONTO MOONLETS EMBEDDED IN SATURN's RINGS, *The Astrophysical Journal*, 797(2), 93.
URL: *https://doi.org/10.1088/0004-637x/797/2/93*

Zelenyi, L. M., Dolgonosov, M. S., Grigorenko, E. E., & Sauvaud, J.-A., 2007, Universal properties of the nonadiabatic acceleration of ions in current sheets, *JETP Letters*, 85(4), 187–193.
URL: *https://doi.org/10.1134/S0021364007040017*

Zelenyi, L. M., Grigorenko, E. E., & Fedorov, A. O., 2004, Spatial-temporal ion structures in the earth's magnetotail: Beamlets as a result of nonadiabatic impulse acceleration of the plasma, *Journal of Experi-*

mental and Theoretical Physics Letters, 80(10), 663–673.

URL: *https://doi.org/10.1134/1.1857276*

Zhang, H., Gao, Y., & Law, C. K., 2018, Magnetic reconnection detonation in supernova remnants, *The Astrophysical Journal*, 864(2), 167.

URL: *https://dx.doi.org/10.3847/1538-4357/aad819*

Zhang, H., Sironi, L., & Giannios, D., 2021, Fast particle acceleration in three-dimensional relativistic reconnection, *The Astrophysical Journal*, 922(2), 261.

URL: *https://dx.doi.org/10.3847/1538-4357/ac2e08*

Zharkova, V. V. & Gordovskyy, M., 2004, Particle acceleration asymmetry in a reconnecting nonneutral current sheet, *The Astrophysical Journal*, 604(2), 884.

URL: *https://dx.doi.org/10.1086/381966*

Appendix A

Full form of the Torques and Complete set of Occultations for the Mimas 5:3 Bending Wave

A.1 Complete Form of the Torques on Self-gravity Wakes

Let $\mu_G = \frac{GM_S}{r^3}$ where r is the radial distance from Saturn, $M_S n$ is the mass of Saturn and G the gravitational constant.

$$\begin{aligned}
\tau_{\text{tidal+wake};x'} &= 4\big(\overbrace{\mu_G}^{\text{tidal}} - \overbrace{\pi G\sigma k^2 \cos^2\theta_w}^{\text{wake}}\big)\tfrac{L^3}{24} W H \rho_H \,(\hat{z}'\cdot\hat{x})\,(\hat{y}'\cdot\hat{x}) \\
&-2\big(\overbrace{\mu_G}^{\text{tidal}} + \overbrace{2\pi G\sigma k^2 \sin^2\theta_w}^{\text{wake}}\big)\tfrac{L^3}{24} W H \rho_H \,(\hat{z}'\cdot\hat{y})\,(\hat{y}'\cdot\hat{y}) \\
&\overbrace{-4\pi G\sigma k \cos\theta_w \sin\theta_w}^{\text{wake}}\,\tfrac{L^3}{24} W H \rho_H \Big[(\hat{z}'\cdot\hat{y})(\hat{y}'\cdot\hat{x}) + (\hat{z}'\cdot\hat{x})\,(\hat{y}'\cdot\hat{y})\Big]
\end{aligned} \tag{A.1}$$

$$\begin{aligned}
\tau_{\text{tidal+wake};y'} &= -4\big(\overbrace{\mu_G}^{\text{tidal}} - \overbrace{\pi G\sigma k^2 \cos^2\theta_w}^{\text{wake}}\big)\tfrac{W^3}{24} L H \rho_H \,(\hat{z}'\cdot\dot{x})\,(\hat{x}'\cdot\hat{x}) \\
&+2\big(\overbrace{\mu_G}^{\text{tidal}} + \overbrace{2\pi G\sigma k^2 \sin^2\theta_w}^{\text{wake}}\big)\tfrac{W^3}{24} L H \rho_H \,(\hat{z}'\cdot\dot{y})\,(\hat{x}'\cdot\hat{y}) \\
&+\overbrace{4\pi G\sigma k \cos\theta_w \sin\theta_w}^{\text{wake}}\,\tfrac{W^3}{24}\rho_H L H \left[(\hat{z}'\cdot\hat{y})\,(\hat{x}\cdot\hat{x}) + (\hat{z}'\cdot\hat{x})\,(\hat{x}'\cdot y')\right]
\end{aligned} \tag{A.2}$$

$$\begin{aligned}
\tau_{\text{tidal+wake};z'} &= 4\big(\overbrace{\mu_G}^{\text{tidal}} - \overbrace{\pi G\sigma \cos^2\theta_w}^{\text{wake}}\big)\tfrac{L^3}{24}\rho_H H W \left(\hat{x}'\cdot\hat{x}\right)(\hat{y}'\cdot\hat{x}) \\
&+2\big(\overbrace{\mu_G}^{\text{tidal}} + \overbrace{2\pi G\sigma \sin^2\theta_w}^{\text{wake}}\big)\tfrac{L^3}{24}\rho_H H W \left(\hat{x}'\cdot\hat{y}\right)(\hat{y}'\cdot\hat{y}) \\
&+\overbrace{4\pi G\sigma k \cos\theta_w \sin\theta_w}^{\text{wake}}\,\tfrac{L^3}{24}\rho_H H W \left[(\hat{x}\cdot\hat{y})\,(\hat{y}'\cdot\hat{x}) + (\hat{x}\cdot\hat{x})\,(\hat{y}'\cdot\hat{y})\right]
\end{aligned} \tag{A.3}$$

Where W, H and L are the length of the principal axis of the wake. Centered on the center of the wake we set a coordinate systems along these axis which are x', y', z' respectively. k is the wavenumber of

the self-gravity wakes which are treated as a plane-wave field. ρ_H is the density of the self-gravity wake and σ is its surface density. θ_w is the angle with respect to the azimuthal of the long axis L of the oriented wake field.

Consider the direction $\hat{\theta}$, which is the direction of the velocity of a particle colliding using the Hill equations (see Figure 2.6). Consider moreover, that the space density of colliding particles is given by $\rho(z) = e^{-(\frac{z}{z_0})^2}$ where z_0 is the rings' half-thickness, and note that the z coordinate can be written in terms of (x', y', z'). We can then write the torques due to collisions of particles with a space density ρ_s, both due to the BW shear (caused by the slope of the bending wave $\frac{dz}{dx}$) and due to the Keplerian shear, as:

$$\begin{aligned}\tau_{\mathrm{Kep+BWsh};x'} =& 2*(1+\epsilon)\int_{b_{\min}}^{b_{\max}}\left|\overbrace{\boldsymbol{v}_\theta\cdot\hat{z}'}^{\text{Keplerian}}+(\overbrace{\frac{dz}{dx}(\hat{y}'\cdot\hat{x})(\hat{z}'\cdot\hat{z})}^{\text{BW shear}}-\omega_{x'})y'(b)\right| \\ &+\left[\overbrace{\boldsymbol{v}_\theta\cdot\hat{z}'}^{\text{Keplerian}}+(\overbrace{\frac{dz}{dx}(\hat{y}'\cdot\hat{x})(\hat{z}'\cdot\hat{z})}^{\text{BW shear}}+\omega_{y'})y'(b)\right]y'(b)\int_{-W/2}^{W/2}\rho_s(z(x',y'(b)))dbdx'\end{aligned} \tag{A.4}$$

$$\begin{aligned}\tau_{\mathrm{Kep+BWsh};y'} =& -2*(1+\epsilon)\int_{b_{\min}}^{b_{\max}}\left|\overbrace{\boldsymbol{v}_\theta\cdot\hat{z}'}^{\text{Keplerian}}+(\overbrace{\frac{dz}{dx}(\hat{x}'\cdot\hat{x})(\hat{z}'\cdot\hat{z})}^{\text{BW shear}}+\omega_{y'})x'(b)\right| \\ &+\left[\overbrace{\boldsymbol{v}_\theta\cdot\hat{z}'}^{\text{Keplerian}}+(\overbrace{\frac{dz}{dx}(\hat{x}'\cdot\hat{x})(\hat{z}'\cdot\hat{z})}^{\text{BW shear}}+\omega_{y'})x'(b)\right]x'(b)\int_{-L/2}^{L/2}\rho_s(z(x'(b),y'))dbdy'\end{aligned} \tag{A.5}$$

$$\begin{aligned}\tau_{\mathrm{Kep+BWsh};z'} =& -2*(1+\epsilon)\int_{b_{\min}}^{b_{\max}}\left|\overbrace{\boldsymbol{v}_\theta\cdot\hat{x}'}^{\text{Keplerian}}+(\overbrace{\frac{dz}{dx}(\hat{y}'\cdot\hat{x})(\hat{z}'\cdot\hat{z})}^{\text{BW shear}}+\omega_{z'})y'(b)\right| \\ &+\left[\overbrace{\boldsymbol{v}_\theta\cdot\hat{z}'}^{\text{Keplerian}}+(\overbrace{\frac{dz}{dx}(\hat{y}'\cdot\hat{x})(\hat{z}'\cdot\hat{z})}^{\text{BW shear}}+\omega_{z'})y'(b)\right]y'(b)\int_{-H/2}^{H/2}\rho_s(z(y'(b),z'))dbdz'\end{aligned} \tag{A.6}$$

Finally the torque caused by the radial gradient of the vertical acceleration due to the bending wave:

$$\boldsymbol{\tau}_{\mathrm{BWg},x'} = -\frac{2}{3}\omega'^2\frac{\partial z}{\partial y'}(\hat{z}\cdot\hat{z}')(\hat{y}'\times\hat{z}')\rho_H HW\left(\frac{L}{2}\right)^3 \tag{A.7}$$

$$\boldsymbol{\tau}_{\mathrm{BWg},y'} = -\frac{2}{3}\omega'^2\frac{\partial z}{\partial x'}(\hat{z}\cdot\hat{z}')(\hat{x}'\times\hat{z}')\rho_H HL\left(\frac{W}{2}\right)^3 \tag{A.8}$$

$$\boldsymbol{\tau}_{\mathrm{BWg},z'} = -\frac{2}{3}\omega'^2 \frac{\partial z}{\partial y'}(\hat{z}\cdot\hat{x}')(\hat{y}'\times\hat{x}')\rho_H HW\left(\frac{L}{2}\right)^3 \tag{A.9}$$

A.2 Table with the UVIS Occultations of the Mimas 5:3 Bending Wave and their Geometry

The below table collects all UVIS occultations with $\tau_{\max} > 1.5$ for the Mimas 5:3 bending wave region.

Occultation	B [deg]	ϕ [deg]	$B_{\rm eff}$ [deg]	Lon. [deg]	Z	sign($\dot{Z}$)	b	I_0	$\tau_{\rm max}$	$\Phi_{\rm theory}$[deg]
AlpAra(105)E	54.4	77.1	80.9	125.7	-4046	-1	9950	16.94937	3.2	224
AlpAra(105)I	54.4	355.8	54.5	314.9	4072	-1	11381	18.1537	3.5	83
AlpAra(32)I	54.4	277.9	84.4	258.6	3837.8	-1	38303	75.4764	6.1	312
AlpAra(33)I	54.4	278	84.3	12.4	2512	1	36362	84.57951	5.5	115
AlpAra(35)E	54.4	116.1	72.6	343.7	-4739.8	-1	36982	75.47634	3.8	268
AlpAra(63)E	54.4	106.8	78.3	221.1	3969.2	-1	28626	38.80406	5.5	280
AlpAra(79)I	54.4	6.5	54.6	207.1	688.9	1	24713	32.6135	3.6	34
AlpAra(85)E	54.4	93.4	87.6	85.8	5119.7	1	24444	24.13635	3.5	61
AlpAra(85)I	54.4	5.7	54.6	233.9	2256.6	1	24897	28.06419	3.5	306
AlpAra(86)E	54.4	94.1	87	147.2	2714.7	1	21499	26.68124	3.5	118
AlpAra(86)I	54.4	5	54.5	299.1	-2625.6	1	22373	28.52165	3.5	348
AlpAra(90)E	54.4	93.7	87.3	103	4970.2	-1	20224	21.15087	3.6	7
AlpAra(90)I	54.4	5.2	54.5	252.2	3600.4	1	20057	27.9169	3.5	251
AlpAra(96)E	54.4	82.6	84.7	124.1	3156.1	-1	19349	19.06265	3.5	141
AlpAra(96)I	54.4	12.8	55.1	254.8	4942.7	1	19563	41.38505	3.6	271
AlpAra(98)E	54.4	75.4	79.8	110.7	131.2	-1	17371	56.24169	3.6	231
AlpAra(98)I	54.4	8.4	54.7	250.9	4825.8	-1	17202	65.79578	3.6	321
AlpCMa(274)E	13.5	40.4	17.5	188.9	2833.2	-1	23747	68.66385	1.7	246
AlpCMa(281)I	13.5	230.1	20.5	144.3	3652.3	1	27911	57.7524	1.7	143
AlpCru(100)E	68.2	93.9	88.5	188.8	807.8	1	428757	501.3685	5.8	289
AlpCru(100)I	68.2	154.5	70.1	213.6	-5016.5	1	434175	501.3685	6	102
AlpCru(92)I	68.2	169.6	68.5	114.7	-4232.1	1	518555	501.3384	6.3	160
AlpLup(248)E	53.9	111.4	75.1	73.2	4024.3	-1	16967	223.1837	4.8	150
AlpLyr(175)I	-35.2	233.8	50.1	318.5	1522.8	-1	8139	21.61554	4	104
AlpLyr(202)E	-35.2	35	40.7	191.8	-4393	-1	8139	21.61554	3.7	147
AlpLyr(202)I	-35.2	236	51.6	90.2	3092.6	-1	6485	19.1991	2.9	277
AlpLyr(206)I	-35.2	252.9	67.4	151.7	-1264.5	-1	6801	17.57583	3.5	82
AlpScoB(13)E	32.2	117.8	53.4	255.1	-831.6	-1	3409	104.8678	1.8	204
AlpScoB(13)I	32.2	195.6	33.1	216.3	2447	-1	3499	123.7631	1.8	321
AlpScoB(29)I	32.2	286.5	65.7	343.9	-2274.3	1	3452	62.04907	2.3	173
AlpVir(116)I	17.3	243.3	34.7	188.8	5001	-1	161196	55.39598	1.7	22
AlpVir(124)E	17.3	123.3	29.5	218.4	-2033.2	1	153398	203.5833	2.2	138
AlpVir(134)I	17.3	284.9	50.4	215.4	-637.2	1	158112	311.6297	2.2	346
AlpVir(173)E	17.3	93	80.4	329.3	-666.8	-1	124007	200.0026	1.7	265
AlpVir(173)I	17.3	31.2	20	71.1	2787.3	-1	124993	200.0026	1.7	358
AlpVir(210)I	17.3	311.5	25.1	46	-4015.8	1	138215	43.22061	2.5	259
AlpVir(211)I	17.3	267.2	81.2	103.3	-2632.7	1	132499	469.4783	1.8	231
AlpVir(232)E	17.3	89.3	87.8	316.7	-2068.6	1	125750	455.5824	2.3	284
AlpVir(30)I	17.3	230.4	26	6.9	-2187.3	1	532397	177.7105	2.5	262
AlpVir(34)E	17.3	332.9	19.2	259.5	2584	1	489542	247.7773	1.7	207
AlpVir(34)I	17.3	232.8	27.2	24	579.6	1	510631	145.8352	2.2	225
AlpVir(8)E	17.3	91.3	85.9	197.2	3679.9	-1	526802	2500.032	1.7	20
AlpVir(8)I	17.3	141.1	21.8	162.3	4488.6	-1	500231	2499.995	1.8	145
BetCen(102)I	66.7	249.1	81.3	0.9	4984.3	-1	370169	329.3598	7.3	55
BetCen(104)E	66.7	105.5	83.5	299.7	-3402.1	1	342974	288.9692	8.6	155
BetCen(104)I	66.7	209.3	69.4	321	-1126.9	-1	357501	312.9495	6.7	304
BetCen(105)E	66.7	100.5	85.5	47	-3710.5	-1	287316	145.6972	6.3	353
BetCen(105)I	66.7	212.9	70.1	83.1	5023	1	313435	151.4026	5.2	61
BetCen(64)E	66.7	101.7	85	282.5	1854.5	1	619944	469.1418	5.6	286
BetCen(75)I	66.7	270.5	89.8	232.9	-934	1	594336	465.1562	7.6	273
BetCen(77)E	66.7	47.5	73.8	12.6	4961	1	593240	336.3192	7.4	160
BetCen(77)I	66.7	270.4	89.8	257.3	-1823.4	1	587228	252.7589	7.7	165
BetCen(78)E	66.7	45.9	73.3	206.5	-5087.4	-1	564075	375.1392	7	293
BetCen(81)I	66.7	275.6	87.6	147.8	4636	-1	550954	281.519	7.1	19
BetCen(85)I	66.7	277.5	86.8	41.8	-4526.9	-1	533158	354.402	7.6	210
BetCen(89)I	66.7	278	86.6	322.8	-572.3	1	498234	330.1721	7.7	277
BetCen(92)E	66.7	55	76.2	75.5	4143.3	-1	452618	230.9221	6.2	319
BetCen(96)I	66.7	271.9	89.2	126.3	-4796.6	-1	444264	229.5003	6.3	239
BetCMa(211)I	14.2	223.4	19.2	67.1	-3637.3	1	43518	50.86847	1.8	1
BetCru(253)I	65.2	255.6	83.4	187.3	-4002.7	-1	106166	202.3216	6.5	157
BetCru(262)I	65.2	257.3	84.2	18	5014.2	-1	109532	185.7413	6.4	345
BetCru(98)I	65.2	192.7	65.7	319	3954.6	-1	274051	232.4198	7.1	248
BetPer(116)E	-47.4	143	53.7	216.7	1129.6	1	2135	43.00056	2.7	1
BetPer(116)I	-47.4	165.1	48.4	208.1	-79.3	1	2130	43.00056	2.8	22
BetPer(42)I	-47.4	229.7	59.2	122.9	-4479.8	-1	20003	43.61236	3	244
ChiCen(39)I	47.6	175.5	47.6	101.6	4977.8	1	13121	59.66402	3.8	345
DelCen(183)E	55.6	149.3	59.5	177.7	3370.9	1	11397	217.076	4.6	5
DelCen(185)E	55.6	150	59.3	44.2	-1532	-1	10924	200.8173	4.5	336
DelCen(191)E	55.6	138.4	62.9	335.4	-1934.9	1	10932	211.6986	4.6	31
DelCen(194)I	55.6	294.7	74	270.1	-5045.4	1	11891	22.14481	4.1	54
DelCen(64)E	55.6	110.6	76.4	194.3	4773.2	1	52909	90.11278	5	327
DelCen(64)I	55.6	124.8	68.6	210.7	3089.3	1	53150	90.11546	4.9	229
DelCen(66)I	55.6	135.4	64	124	3831.5	-1	58632	45.05706	4.7	311
DelCen(98)I	55.6	211.3	59.6	54.8	402.3	1	34467	90.11549	5.8	100

Table A1

Occultation	B [deg]	ϕ [deg]	$B_{\rm eff}$ [deg]	Lon. [deg]	Z	sign($\dot{Z}$)	b	I_0	$\tau_{\rm max}$	$\Phi_{\rm theory}$[deg]
DelPer(36)E	-54	66.5	73.9	296	2858.5	-1	13677	376.012	3.9	357
DelPer(37)I	-54	264.5	86	145.7	4558.5	-1	13632	37.60231	5	29
DelPer(39)I	-54	264.6	86.1	45	-4744	-1	12741	38.59457	4.2	203
DelPer(41)I	-54	238.6	69.3	166.7	-496	-1	12185	63.56438	3.6	14
DelPer(60)I	-54	277.2	84.8	192.3	4814.5	-1	11711	20.13449	3.6	16
DelSco(236)I	28.7	263.2	77.9	10.8	-5022.7	-1	22981	647.6574	2.8	171
EpsCas(104)E	-70	122.3	79	123.6	-4468.4	1	4557	37.14048	3.6	300
EpsCas(104)I	-70	187.8	70.1	152.8	-2034.7	-1	4586	37.14048	3.8	87
EpsCen(65)I	59.6	226.6	68.1	343.1	-1573.5	-1	129715	127.6824	6.6	220
EpsCMa(173)I	26	267	84	187.1	4165.8	1	40005	13.82051	2.8	341
EpsCMa(174)I	26	267.1	84	47.5	-3225.3	-1	44805	15.57652	2.8	344
EpsCMa(276)E	26	50.6	37.5	217.7	4192	-1	69532	117.8264	2.6	109
EpsLup(36)E	51	44.9	60.2	135.3	2840.1	-1	32671	71.62883	5.7	100
EpsLup(37)E	51	359.8	51	356.7	-1132.5	1	31958	72.21977	3.7	135
EtaLup(34)E	44.5	357.1	44.5	90	-3167.9	-1	46980	82.68831	4.2	353
EtaLup(34)I	44.5	296.2	65.7	218.8	2575.6	-1	47613	83.364	3.4	130
GamAra(37)I	61	248.7	78.6	62.1	4684.1	1	26751	58.10375	4.2	133
GamCas(100)E	-66.3	72.5	82.5	93.5	-3408.3	1	54160	93.44911	6.1	259
GamCol(173)E	-39.9	73.9	71.7	317.7	5020.4	-1	1097	57.81785	1.9	226
GamCol(205)I	-42.6	260.4	79.7	269.1	-2977.3	-1	843	44.80865	2	354
GamGru(40)E	35.1	193.1	35.8	187.8	4856.5	-1	7292	122.9506	3.2	32
GamGru(41)E	35.1	204.5	37.7	98.5	-1794.7	-1	7579	158.2192	2.6	122
GamGru(41)I	35.1	282.7	72.6	98.2	4282.8	-1	8154	166.3223	2.2	225
GamLup(30)E	47.4	114.6	69	173.1	-3263.2	1	77667	59.06165	4.6	303
GamLup(32)E	47.4	33.8	52.6	158.4	5097.4	1	72586	72.70017	5.4	306
GamPeg(172)E	-20.3	74.1	53.5	209.7	5059.2	-1	12683	12.42252	1.8	295
GamPeg(172)I	-20.3	36.7	24.7	283.4	4683.3	1	11491	12.42252	1.7	328
GamPeg(211)E	-20.3	122.5	34.6	207.2	518.8	-1	13192	16.91014	1.8	200
GamPeg(32)I	-20.3	138.6	26.2	226.6	2857.3	1	74756	265.8262	1.8	343
GamPeg(36)E	-20.3	66.8	43.2	343.5	3206.1	1	70975	225.4201	1.8	60
KapCen(35)E	48.5	85.5	86.1	302.8	-5074.8	1	46015	57.75644	5.8	281
KapCen(36)I	48.5	241.2	67	228.6	-2480.8	-1	44129	119.2304	5	330
KapCen(42)I	48.5	168.5	49.1	237.3	228.4	1	41129	119.2288	4.1	88
KapCMa(168)E	29.3	127.3	42.8	286.8	-1613.5	1	6193	43.59726	1.7	229
KapCMa(168)I	29.3	175.9	29.4	268.8	-3886.5	1	6062	43.59726	1.7	270
KapSco(247)I	43.4	273.4	86.4	326.7	4703.2	-1	21356	409.719	3	21
LamSco(248)I	41.7	283.9	75	261.3	585.4	-1	58157	433.8854	3.7	343
LamSco(29)E	41.7	148.3	46.3	222.1	-4753.7	-1	283952	159.058	4.6	35
LamSco(44)I	41.7	235	57.2	62.7	-841.5	-1	252102	136.4883	6.1	254
MuCen(113)I	48.7	239.1	65.8	24.1	-3432.9	-1	9633	23.36014	3.7	81
MuSco(43)E	43.4	27	46.7	303.3	4005.9	-1	86896	441.6879	4	130
PsiCen(38)I	44.3	249.9	70.6	54.2	3180.3	1	1110	58.71554	2.2	137
SigSgr(11)I	29.1	239.5	47.6	111	-2828	-1	118989	995.783	3.4	85
SigSgr(114)I	29.1	330.2	32.6	262.3	-492.7	1	33500	40.79908	2.7	160
SigSgr(244)E	29.1	234.2	43.5	103.7	204.5	1	19555	40.79669	1.9	262
SigSgr(244)I	29.1	269.3	88.8	86.6	-1341.1	1	16595	40.79913	2.1	313
TheAra(40)E	53.9	28.6	57.3	197.2	-2036.3	-1	12489	46.22136	4.1	270
TheAra(40)I	53.9	356.2	53.9	317	4476.6	-1	12490	46.22205	3.7	66
TheAra(41)E	53.9	82.4	84.5	205.4	1720.2	-1	11762	46.22204	5.5	194
TheCar(190)I	-43.3	252.4	72.2	219.3	-4463.7	1	25334	159.9588	5.7	277
ZetCen(112)I	53.6	239.7	69.6	112.5	4393.8	-1	37307	34.73377	6.4	346
ZetCen(246)E	53.6	79.3	82.2	254.4	-4100.4	1	22256	232.1636	5.1	144
ZetCen(60)I	53.6	228.1	63.8	258.7	-4185.7	-1	107181	113.7307	6.6	235
ZetCen(62)E	53.6	70.1	75.9	8.9	-4066	1	106091	96.60519	5.5	47
ZetPup(171)E	38.6	117.3	60.1	154.4	-2266.7	-1	46835	141.573	4.5	264
ZetPup(171)I	38.6	202.1	40.8	120.2	2022.7	-1	49506	122.4082	4.3	351

Table A1 (continued): Complete UVIS dataset for occultations with $\tau_{\rm max} > 1.5$ in the Mimas 5:3 bending wave region.

Appendix B

Description of 3D Test-Particle Simulation and the field reconstruction

We designed the test-particle simulation to recreate an event in the magnetotail of the Earth by imposing observed conditions and tacking ions as they pass through the domain. Importantly, ions can enter and exit the domain as they would in the magnetotail (fully open boundaries). In treating acceleration, escape is critical (Blandford & Eichler, 1987). The 3D test-particle code used in this study was based on a 3D quasi-self-consistent simulation of the Parker Solar Probe interaction with the solar wind done by Ergun et al. (2010), whose major results were ultimately verified with fully self-consistent simulations (Marchand et al., 2014). The quasi-self-consistent code also was used to characterize a Maven instrument (Ergun et al., 2021). As done in this work, Ergun et al. (2020a) and Ergun et al. (2022) employed realistic $\delta\boldsymbol{B}$ and $\delta\boldsymbol{E}$ signals (in 1D and 3D) to study electron acceleration in Earth's magnetosphere. The heart of the code has a relativistic Boris advancement algorithm (Boris, 1970) that has excellent energy conservation and can accept input of realistic $\boldsymbol{B}$ and $\boldsymbol{E}$ signals. The code in this article was tested for long simulation periods and displayed less than a few percent energy change.

B.1 Simulation Domain, Boundary Conditions, and Background Magnetic Field

The simulation domain is shown in Figure 3.2. The conditions at the boundaries, $T_i = 4\,\mathrm{keV}$, $n_i = 0.1\,\mathrm{cm}^{-3}$, and $|\boldsymbol{B}_{\mathrm{Lobe}}| = 20\,\mathrm{nT}$ are based on observations ($d_i \sim 1000\,\mathrm{km}$; $\rho_i \sim 320\,\mathrm{km}$). The domain includes a magnetic reconnection plane that extends $16R_E\,(\sim 120d_i; \sim 400\rho_i)$ in the x direction (the direction of the reconnecting magnetic field) and $4R_E\,(\sim 25d_i; \sim 80\rho_i)$in the z direction (current sheet normal). The y direction along the nominal magnetic reconnection x-line is adjusted to $2R_E$; the simulation

domain extends $4R_E$.

The simulation contains a background B_x that varies as $\tanh(z/\lambda_z)$ and B_z that varies as $\tanh(x/\lambda_x)$ (Eqn. 3.4). The asymptotic value of $|B_x|$ is $20\,\mathrm{nT}$ and of $|B_z|$ is $2.5\,\mathrm{nT}$, matching the observations. $B_y = 0$ and there is no change in the background $\boldsymbol{B}$ as a function of y. This background $\boldsymbol{B}$ mimics that of magnetic reconnection (shown in Figure 3.2). The background electric field, E_y, is set to $2.7\,\mathrm{mVm}^{-1}$ in the turbulent region to match observations (Ergun et al., 2022). It is reduced by a factor of two outside of the turbulent region.

The simulation has open boundaries. Ions routinely enter from all boundaries with fluxes of a $4\,\mathrm{keV}$ Maxwellian distribution with a density of $0.1\,\mathrm{cm}^{-3}$ at $z = 0$ (n_{sheet}). The density varies as a function of z (shown in Figure 3.2) so that it lowers to $0.025\,\mathrm{cm}^{-3}$ (n_{lobe}) at $z = \pm 2R_E$ as described in Eqn. 3.6. The values of n_{sheet} and n_{lobe} are based on observations.

B.2 Turbulent Electromagnetic Fields

The turbulent region is confined in x at $\pm 7R_E$, in y at $\pm 2R_E$, and in z at $\pm 0.75R_E$. The boundaries of the turbulence region are not abrupt. The turbulence is ramped to full amplitude following a cos2 shape starting with no turbulence at $0.25R_E$ outside of the turbulent region, reaching full strength $0.25R_E$ inside of the turbulent region. This sub-domain in the simulation allows for a buffer zone between the simulation boundaries and the turbulent region of $\sim 1R_E$.

A chief aspect of the test-particle simulation is that the turbulent electromagnetic fields, $\delta\boldsymbol{B}$ and $\delta\boldsymbol{E}$ are designed to mimic those in observations. As described in Eqn 3.3, we employ a set of pseudo-randomized electromagnetic and electrostatic waves designed to match the measured properties of $\delta\boldsymbol{B}$ and $\delta\boldsymbol{E}$ including amplitude, spectra (Figures B.1a and B.1b), wave speeds (Figure B.1c), coherence time (Figure B.1c), and coherence scales (see Ergun et al. 2020a. Wave speeds and correlation times are determined using the four MMS spacecraft.

Three sets of 200 waves are imposed in the simulation domain. Initially, the wave's frequencies are logarithmically spaced (0.01 Hz to 50 Hz), then randomly varied by 0.25 (1 sigma) of the frequency spacing. The wave amplitudes, A_n, are initially assigned to match the measured spectrum (Figure B.1a),

then randomly varied by up to a factor of 2 from the initial value. The directions are random. The wave numbers, k_n, are initially assigned such that $\frac{\omega}{|k_n|}$ matches the measured wave speed (red line in Figure B.1c) then randomly varied by up to a factor of 3. The directions of k_n are randomly assigned in a plane normal to A_n. The phase ϕ_n is randomly assigned from 0 to 2π, As the simulation progresses, the phase is varied as a function of time and position to mimic the observed correlation time (redline in Figure B.1d). The phase also varies in position to mimic the observed correlation distance (not shown).

Once A_n, ω_n, k_n, and ϕ_n are determined for $\delta\boldsymbol{B}$, we derive the electromagnetic part of $\delta\boldsymbol{E}$ directly from Faraday's law. We create the electrostatic part of $\delta\$\boldsymbol{E}$ using the same formula (Eqn. 3.3) to match the measured perpendicular spectrum (Figure B.1b) when summed with the electromagnetic part of $\delta\boldsymbol{E}$. The directions of the individual waves are randomly assigned in a plane perpendicular to the background $\boldsymbol{B}$, but, because of the dramatic changes in the direction of $\delta\boldsymbol{B}$, a small $E_{||}$ can develop. We inject a small correction using Eqn. (3.3) to better recreate the high-frequency part of the $E_{||}$ spectrum (Figure B.1b). The electrostatic part dominates the $\delta\boldsymbol{E}$ spectrum. The evaluation of the coherence lengths and time of $\delta\boldsymbol{E}$ from MMS data was done as described in (Ergun et al., 2020b).

As an additional test, we directly applied the measured $\delta\boldsymbol{B}$ and $\delta\boldsymbol{E}$ signals to particles in the simulation domain. Under this method, $\delta\boldsymbol{B}$ and $\delta\boldsymbol{E}$ vary in time but not as a function of position. To each particle, we randomly assign a different position in the measured $\delta\boldsymbol{B}$ and $\delta\boldsymbol{E}$ vectors (which are filtered from 0.01 Hz to 50 kHz). Ions dwell in the simulation domain for an average of $\sim$ 30 s whereas MMS data endure for $\sim$ 1000 s. The two methods of reconstructing $\delta\boldsymbol{B}$ and $\delta\boldsymbol{E}$ render comparable energization rates and flux distributions, which lends confidence to the subsequent analysis.

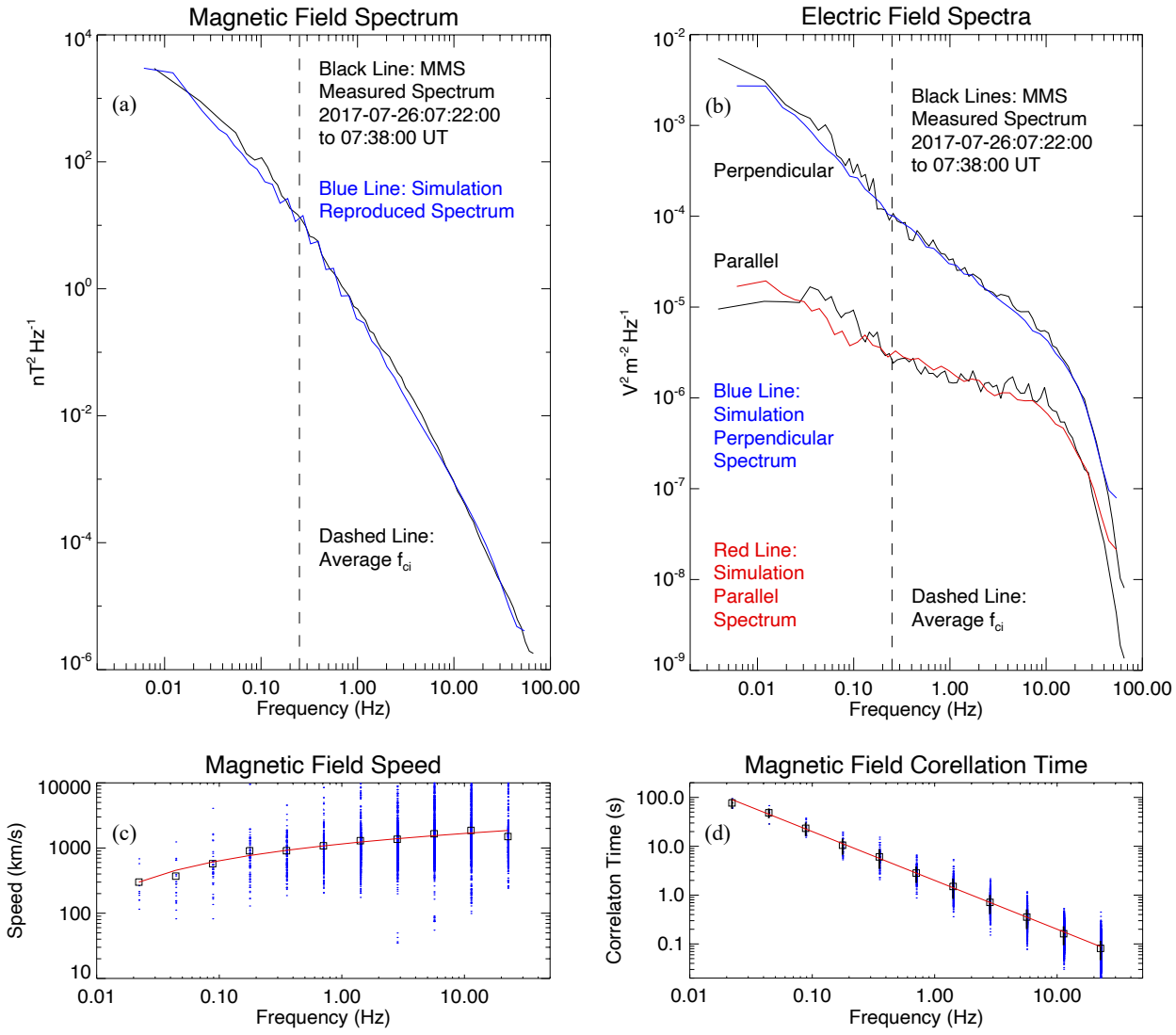

Figure B.1: (a) The measured (black line) and the reproduced (blue line) $\delta \boldsymbol{B}$ spectra. (b) The measured (black line) and the reproduced (red and blue lines) $\delta \boldsymbol{E}$ spectra. (c) The measured speeds of $\delta \boldsymbol{B}$ signals versus frequency derived from time delays from the 4 MMS spacecraft. The blue dots are measurements. The black squares are the averages; the red line a fit of these averages. The red line's formula is used in the simulation. (d) The measured correlation times of $\delta \boldsymbol{B}$ signals versus frequency derived from the 4 MMS spacecraft (same legend as in the $\delta \boldsymbol{E}$ case).

Appendix C

Derivation of Linear Bending Wave Theory for Thin Disks

C.1 Equation of Motion for a Ring Particle

We'll skip here the derivation of the motion of a particle subjected to the force of a central body, and its resulting elliptical trajectory. This is the two body problem that can be reviewed in Murray & Dermott (2000) or any Classical Mechanics textbook. The trajectories considered will be perturbations of this elliptical motion.

C.1.1 Dynamics: Three Body Problem and the Perturbing Function

From Figure C.1 and Newton's laws we can get the differential equation of motion for all three bodies. Here, $\ddot{\boldsymbol{\mathcal{R}}}_{\boldsymbol{S}}$, $\ddot{\boldsymbol{\mathcal{R}}}_{\boldsymbol{i}}$, and $\ddot{\boldsymbol{\mathcal{R}}}_{\boldsymbol{M}}$ are position vectors from an inertial frame, and $\boldsymbol{r}_i$, and $\boldsymbol{r}_M$ are position vectors relative to the center of Saturn. The equations of motion are then written as:

$$M_S \ddot{\boldsymbol{\mathcal{R}}}_{\boldsymbol{S}} = G\frac{M_S m_i}{r_i^3}\boldsymbol{r}_i + \frac{GM_S M_M}{r_M^3}\boldsymbol{r}_M$$

$$m_i \ddot{\boldsymbol{\mathcal{R}}}_{\boldsymbol{i}} = \frac{Gm_i M_M}{|\boldsymbol{r}_i - \boldsymbol{r}_M|^3}(\boldsymbol{r}_i - \boldsymbol{r}_M) - \frac{GM_S m_i}{r_i^3}\boldsymbol{r}_i$$

$$M_M \ddot{\boldsymbol{\mathcal{R}}}_{\boldsymbol{M}} = \frac{Gm_i M_M}{|\boldsymbol{r}_M - \boldsymbol{r}_i|^3}(\boldsymbol{r}_M - \boldsymbol{r}_i) - \frac{GM_S M_M}{r_M^3}\boldsymbol{r}_M$$

where the M and S subscripts represent Mimas and Saturn. We want to write the interactions in terms of $\ddot{\boldsymbol{r}}_i$, which is the acceleration of a ring particle relative to Saturn. So this is a relative coordinate system, but

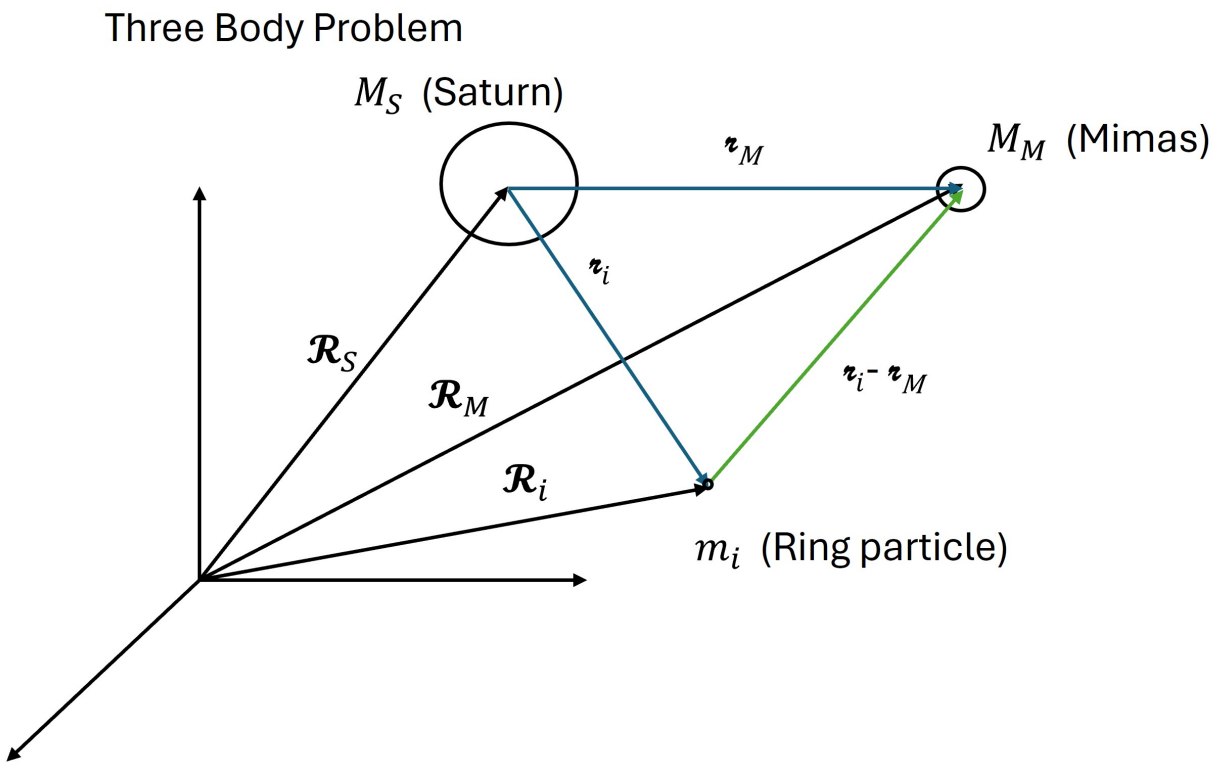

Figure C.1: We begin our treatment by considering the three body problem represented here. m_i represents the ring particle for which we want to know the motion.

it is for all intent and purposes inertial.

$$\ddot{\boldsymbol{\imath}}_i = \ddot{\boldsymbol{\mathcal{R}}}_{\boldsymbol{i}} - \ddot{\boldsymbol{\mathcal{R}}}_{\boldsymbol{S}} = \frac{GM_M}{|\boldsymbol{\imath}_M - \boldsymbol{\imath}_i|^3}(\boldsymbol{\imath} - \boldsymbol{\imath}_M) - \frac{G(M_S + m_i)}{\imath_i^3}\boldsymbol{\imath}_i - \frac{GM_M}{\imath_M^3}\boldsymbol{\imath}_M \tag{C.1}$$

The first term from the right hand side of Eqn. (C.1) is the relative acceleration of the ring's particle due to the satellite (note that the direction of the force is outward). The second represents the acceleration due to the central body and the third term is the correction concerning the acceleration of the central body due to the third body. This last term is dropped as Saturn is much more massive than Mimas. The first term of the right hand side of Eqn. (C.1) is known as the perturbing acceleration.

In this work we mostly use the gravitational acceleration. $g = \frac{F}{m}$

$$\boldsymbol{g}_M = \frac{GM_M}{|\boldsymbol{\imath}_M - \boldsymbol{\imath}_i|^3}(\boldsymbol{\imath}_i - \boldsymbol{\imath}_M) \tag{C.2}$$

$$\boldsymbol{g}_S = -\frac{G(M_S + m_i)}{\imath_i^3}\boldsymbol{\imath}_i \approx -\frac{G(M_S)}{\imath_i^3}\boldsymbol{\imath}_i \tag{C.3}$$

where i represents the ith ring particle, and where M and S subscripts represent Mimas and Saturn, respectively. We will also use the gravitational potential of Saturn when convenient

$$\Phi_S = -\frac{GM_S}{\imath_i} \tag{C.4}$$

There is an extra term that we have omitted in the equations of motion, and this is the effect of the ring itself on the ring particle. If we consider the ring as a body, then this would be a 4 body problem. Dealing with the term is probably the most convoluted aspect of the equation of the bending wave and I'll do so in detail later. For the sake of the completeness of the equations of motion presented in this section, however, we introduce here the expression for the self-gravity of a mass element dm', located at a $\boldsymbol{\imath}'$ exerted at a point on the ith particle at a point $\boldsymbol{\imath}_i$:

$$\boldsymbol{g}_R = -G\int dm' \frac{\boldsymbol{\imath}' - \boldsymbol{\imath}_i}{|\boldsymbol{\imath}' - \boldsymbol{\imath}_i|^3} \tag{C.5}$$

where we are integrating all the differential mass elements dm' that form the rings to find their influence on the ring particle at $\boldsymbol{\imath}_i$. We now write the equation of motion for the ith ring particle, relative to Saturn's center:

$$\ddot{\boldsymbol{\imath}}_i = \boldsymbol{g}_M + \boldsymbol{g}_S + \boldsymbol{g}_R \tag{C.6}$$

In the case of bending waves, we are interested in the vertical acceleration. We use cylindrical coordinates (r, θ, z) centered at Saturn, where the z-axis is perpendicular to the ring's mean plane. The vertical acceleration in then:

$$\frac{d^2 z_i}{dt^2} = \boldsymbol{g}_M \cdot \hat{\boldsymbol{k}} + \boldsymbol{g}_S \cdot \hat{\boldsymbol{k}} + \boldsymbol{g}_R \cdot \hat{\boldsymbol{k}}$$

where $\hat{\boldsymbol{k}}$ is the unit vector in the vertical direction. Finally, we wish to change this inertial coordinate system by a system that is corotating with the ring of Saturn. Let Ω be the mean motion frequency of the ring at a position $\boldsymbol{\imath}_i$ from Saturn. We can transform into a rotating frame by taking a material derivative instead of the time derivative. This will describe the kinematic effects seen as we ride with the particle's (circular) mean motion.

$$\frac{Dz_i}{Dt} = \frac{dz_i}{dt} + (\boldsymbol{v}_i \cdot \nabla) z_i = [(r_i \Omega \hat{\boldsymbol{\theta}} + \dot{r}_i \hat{\boldsymbol{r}} + \dot{z}_i \hat{\boldsymbol{k}}) \cdot \nabla] z_i$$

where θ is the azimuthal coordinate. Since the frame in question is the mean motion of the particle, $\dot{r} = 0$ and $\dot{z}$ vanish. Moreover, the azimuthal component of ∇ is $\frac{1}{r}\frac{d}{d\theta}$

$$\frac{Dz}{Dt} = (\frac{d}{dt} + r\Omega \frac{1}{r}\frac{d}{d\theta}) z$$

where we have dropped the subscript from i and it is implicit that the coordinates refer to a ring particles, unless it is stated otherwise. Finally we get the equation of motion for the vertical coordinate:

$$(\frac{d}{dt} + \Omega \frac{d}{d\theta})^2 z = g_{Mz}(r, \theta, z, r_M, \theta_M, z_M) + g_{Sz}(r, \theta, z) + g_{Rz}(r, \theta, z) \tag{C.7}$$

This is the equation for the vertical motion of a particle in the ring, described in a frame that co-rotates with this particle's unperturbed orbit. To solve this equation we need an expression for the gravitational terms in the right-hand side of Eqn. (C.7). The place to start are Eqns. (C.2), (C.3), (C.4), and (C.5). The rest of this section will be dedicated to linearizing these term in z to then have a solvable differential equation for the vertical coordinate of a ring particle in a bending wave.

C.1.2 List of assumptions made

- The center of Saturn is an inertial frame, i.e. the force of Mimas in Saturn is negligible as well as the force of the rings on Saturn.
- The rings are smooth enough to be describable with a continuous surface mass density σ which is azimuthally symmetric.
- The mean motion angular velocity of the rings particle is close to the Keplerian frequency. i.e particles in the rings move azimuthally approximately at an uniform circular motion rate. The deviations from the Keplerian frequency of the mean motion of a particle around Saturn is due to the oblateness of Saturn (the J moments), and we will make this deviation explicit in the next section.

C.2 Derivation of the gravitational acceleration terms

C.2.1 g_{S_z}: Acceleration due to Saturn.

Saturn's potential (Φ_S) is not spherically symmetric, as Saturn significantly deviates from being a sphere (Jacobson et al., 2006). Because of this a particle that displaces from the equatorial plane will have an acceleration that differs from the centripetal acceleration of a central force. Particularly, the component of the gravitational acceleration (g_{S_z}) that brings the particle back to the plane will be stronger than that expected from an spherical body, and hence the speed at which the particle returns to the plane will be bigger than the expected value of half an orbit. These results will be derived in this section.

We start with start with Eqn. (C.4), the potential of Saturn. If Saturn were spherical:

$$\Phi_S = -\frac{GM_S}{r}$$

where M_S is the total mass of Saturn and r_i the Saturncentric distance of a ring particle. We now consider that the distribution of Saturn is not spherical, and hence we have to integrate some density function over this non-spherical but axisymmetric volume

$$\Phi_S = -G \int \frac{1}{\mathcal{R}} \rho(\boldsymbol{r}') dV' \tag{C.8}$$

where $\mathcal{R} = r^2 + r'^2 - 2rr' \cos\phi$, where ϕ is the angle between $\boldsymbol{r}$ and $\boldsymbol{r}'$ which are position vectors whose origin in the center of Saturn (for our case r' takes values less or equal to Saturn's radius and r in greater than Saturn's radius). The primed variables are the ones to be integrated over the volume V'. Note that the potential only depends on the polar angle ϕ which assumes the cylindrical symmetry of the potential Φ_S. In general, $\frac{1}{\mathcal{R}}$ can be expanded as Legendre Polynomials in the variable $\cos(\phi)$ (Griffiths, 2013).

$$\frac{1}{\mathcal{R}} = \frac{1}{r} \sum_{n=0}^{\infty} (\frac{r'}{r})^n \mathcal{P}_n(\cos\phi)$$

To write this in terms of the latitudes α and α' weJ use the addition theorem of spherical harmonics (Arfken & Weber, 2005), which implies for our axisymmetric case that:

$$\mathcal{P}_n(\cos\phi) = \mathcal{P}_n(\sin\alpha')\mathcal{P}_n(\sin\alpha)$$

The potential of Saturn (Eqn. C.8) becomes:

$$\Phi_S = -G \left[\sum_{n=0}^{\infty} \frac{1}{r^{(n+1)}} \int r'^n \mathcal{P}_n(\sin\alpha') \rho(\boldsymbol{r}') dV' \right] \mathcal{P}_n(\sin\alpha) \tag{C.9}$$

Expanding the Legendre polynomial and writing their coefficients coming from the integrals as

$$J_n \equiv -\frac{1}{M_S R_S^n} \int r'^n \mathcal{P}_n(\sin\alpha') \rho(\boldsymbol{r}') dV'$$

we get

$$\Phi_S = -\frac{GM_S}{\wr}\left[1 - \sum_{n=2}^{\infty} J_n \left(\frac{R_S}{\wr}\right)^n \mathcal{P}_n(\sin\alpha)\right]$$

where R_S is the radius of Saturn and α is the complement of the polar angle in spherical coordinates (hence $\sin\alpha = \frac{z}{\wr}$). Expanding up to J_4 and keeping terms up to $\sin^2\alpha$:

$$\Phi_S \approx -\frac{GM_S}{\wr}\left[(1 + \frac{1}{2}J_2\left(\frac{R_S}{\wr}\right)^2 - \frac{3}{8}J_4\left(\frac{R_S}{\wr}\right)^4) - \frac{3}{2}J_2\left(\frac{R_S}{\wr}\right)^2\sin^2\alpha + \frac{30}{8}J_4\left(\frac{R_S}{\wr}\right)^4\sin^2\alpha\right] \tag{C.10}$$

To this potential we must add the centrifugal force effects due to the orbiting of the ring's particle around Saturn to obtain an effective potential. Assuming centrifugal equilibrium ($\Omega^2 = -\frac{1}{\wr}\left.\frac{\partial\Phi_S}{\partial\wr}\right|_{\alpha=0}$), which is to say that the orbit around Saturn remains nearly circular, the centrifugal potential is given by:

$$\Phi_{\text{cf}} = \frac{\wr\sin^2\alpha}{2}\left(\frac{\partial\Phi_S}{\partial\wr}\right)_{\alpha=0}$$

Expanding this up to J_4 we get:

$$\Phi_{\text{cf}} \approx -\frac{GM_S\sin^2\alpha}{\wr}\left[-\frac{1}{2} - \frac{3}{4}J_2\left(\frac{R_S}{\wr}\right)^2 + \frac{15}{16}J_4\left(\frac{R_S}{\wr}\right)^4\right]$$

Adding this to the gravitational potential (Eqn .C.10) we find that:

$$\Phi_{S_{\text{eff}}} \approx -\frac{GM_S}{\wr}\left[1 + \frac{1}{2}J_2\left(\frac{R_S}{\wr}\right)^2 - \frac{3}{8}J_4\left(\frac{R_S}{\wr}\right)^4 + \sin^2\alpha\left(-\frac{1}{2} - \frac{9}{4}J_2\left(\frac{R_S}{\wr}\right)^2 + \frac{75}{16}J_4\left(\frac{R_S}{\wr}\right)^4\right)\right]$$

The acceleration in the z-axis then becomes (up to 2nd order in $\sin\alpha$):

$$\ddot{z} = -\frac{\partial\Phi_{S_{\text{eff}}}}{\partial z} = -\frac{\partial\Phi_{S_{\text{eff}}}}{\partial(\sin\alpha)}\frac{\partial(\sin\alpha)}{dz}$$

$$\ddot{z} = \frac{GM_S\sin\alpha}{\wr^2}\left[-1 - \frac{9}{2}J_2\left(\frac{R_S}{\wr}\right)^2 + \frac{75}{8}J_4\left(\frac{R_S}{\wr}\right)^4\right]$$

Now, we consider the acceleration of a particle that deviates a distance ξ from the equatorial place and expand $-\frac{\partial\Phi_{S_{\text{eff}}}}{\partial z}$ about $z = 0$

$$z = z_0 + \xi = \xi$$

$$\ddot{\xi} = -\left(\left.\frac{\partial \Phi_{S_{\text{eff}}}}{\partial z}\right|_{z=0} + \left.\frac{\partial^2 \Phi_{S_{\text{eff}}}}{\partial z^2}\right|_{z=0} \right) \xi$$

The first term in the expansion vanishes, leaving:

$$\ddot{\xi} = -\left.\frac{\partial^2 \Phi_{S_{\text{eff}}}}{\partial z^2}\right|_{z=0} \xi$$

This describes a simple harmonic oscillator with frequency:

$$\left.\frac{\partial^2 \Phi_{S_{\text{eff}}}}{\partial z^2}\right|_{z=0} \equiv \mu^2 = \frac{GM_S}{r^3}\left[1 + \frac{9}{2}J_2(\frac{R_S}{r})^2 - \frac{75}{8}J_4(\frac{R_S}{r})^4\right] \tag{C.11}$$

where μ is defined as the vertical frequency of the particle at a cylindrical radius r, R_S is the radius of Saturn, and where the J moments can be measured by observing how Cassini's trajectory differs from that caused by an spherical potential. In this work I use the values in (Jacobson et al., 2006).

Finally, we will make the assumption that the particle in question will oscillate at the forcing frequency ω provided by the moon Mimas. That is, a single particle in the ring will behave like an forced oscillator with forcing frequency ω and natural frequency μ. The forcing frequency dominates in the steady-state solution, and hence we write:

$$z = \text{Re}[h(r)e^{i(\omega t - m\theta)}] \tag{C.12}$$

So we can write g_{S_z} as:

$$g_{S_z} = \text{Re}[-\mu^2 h(r)e^{i(\omega t - m\theta)}] \tag{C.13}$$

C.2.2 g_{Mz}: Acceleration due to Mimas

We start with Eqn. (C.2) in cylindrical coordinates and dotting with $\hat{\boldsymbol{k}}$.

$$\boldsymbol{g}_M = -\frac{GM_M}{[(z-z_M)^2 + r^2 + r_M^2 - 2rr_M\cos(\theta-\theta_M)]^{\frac{3}{2}}}(\boldsymbol{r}-\boldsymbol{r}_M)\cdot\hat{\boldsymbol{k}}$$

where we have dropped the i subscript and now the particle's coordinates are represented by the variables (r, θ, z). Moreover, we want to know Mimas' force on a particle in the ring's plane, so $z = 0$:

$$g_{Mz} = \frac{GM_M}{[(z_M)^2 + r^2 + r_M^2 - 2rr_M\cos(\theta-\theta_M)]^{\frac{3}{2}}}z_M$$

We make our first assumption, which is that Mimas motion only deviates linearly from circular motion around Saturn, which corresponds to small displacements on the coordinates about a frame of reference centered at the position of the circular orbit (this is called the perturbed guiding center approximation) Eventually, we will replace the coordinates of Mimas by functions of time and hence eliminate them from Eqn. (C.7), making the equation solvable. In order to do this, we write the coordinates as:

$$r_M = a_M + \delta$$

$$\theta_M = (\Omega_M + \dot{\epsilon})t$$

$$z_M = \xi$$

where $t = 0$ at the ascending node of Mimas and the $\theta_M = 0$ at the ascending node. The acceleration up to second order terms is:

$$g_{M_z} = g_{Mz}(a_M, \Omega_M t, 0) + \left.\frac{\partial g_{Mz}}{\partial r_M}\right|_0 \delta + \left.\frac{\partial g_{Mz}}{\partial z_M}\right|_0 \xi + \left.\frac{\partial g_{Mz}}{\partial \theta_M}\right|_0 \epsilon + \left.\frac{\partial^2 g_{Mz}}{\partial z_M \partial \theta_M}\right|_0 \xi\epsilon + \left.\frac{\partial^2 g_{Mz}}{\partial z_M \partial r_M}\right|_0 \xi\delta + \mathcal{O}(3)$$

where the subscript 0 denotes the evaluation of the partial derivative at $r_M = a_M$, $\theta_M = \Omega_M t$, and $z_M = 0$, and where we have not written the terms corresponding to $\frac{\partial^2 g_{Mz}}{\partial \theta_M^2}$, $\frac{\partial^2 g_{Mz}}{\partial r_M^2}$, and $\frac{\partial^2 g_{Mz}}{\partial \theta_M r_M}$ because they are third order in smallness (since z_M is small, these derivatives are themselves one order in smallness and when multiplied by the second order displacements the terms become third order in smallness). The final expression is:

$$g_{M_z} \approx \frac{GM_M\xi}{\Delta^{3/2}} - \frac{3GM_M\xi}{\Delta^{5/2}} * [a_M - r\cos(\Omega_M t - \theta)) * \delta - a_M * r\sin(\Omega_M t - \theta) * \epsilon] \tag{C.14}$$

where $\Delta = a_M^2 + r^2 - 2a_M r\cos(\Omega_M t - \theta)$

Now we'll replace θ_M, z_M and r_M by their equations of motion, which will be sinusoidal deviations from a circular orbit similar to equation those implied by Eqn. (C.11). In fact, because the circular orbit perturbation comes from Saturn's oblateness, the equation for z_M is (Eqn. C.11).

$$\ddot{\xi} = -\mu_M^2\xi \tag{C.15}$$

With the same linearization technique used for Eqn. (C.11), we can derive the linear equations for the r_M and θ_M:

$$\frac{d^2r_M}{dt^2} - r_M\dot{\theta_M}^2 = -\frac{\partial\Phi_S}{\partial r}$$

$$\frac{d}{dt}(r_M^2\dot{\theta_M}) = 0$$

By linearizing these equation, and the radial gravitational acceleration due to Saturn as

$$\frac{\partial\Phi_S}{\partial r} = \frac{\partial\Phi_S}{\partial r}(a_M) + \left.\frac{\partial^2\Phi_S}{\partial r^2}\right|_{a_M}\delta,$$

we arrive at the equations (as done in Chandrasekhar 1942):

$$\ddot{\delta} = (-\frac{3}{a_M}\frac{\partial\Phi_S}{\partial r} + \frac{\partial^2\Phi_S}{\partial r^2})\delta \tag{C.16}$$

$$\dot{\epsilon} = -2\frac{\delta}{a_M}\Omega_M \tag{C.17}$$

Note that the first equation is a simple harmonic oscillator equation with natural frequency $\kappa_M^2 = (-\frac{3}{a_M}\frac{\partial\Phi_S}{\partial r} + \frac{\partial^2\Phi_S}{\partial r^2})$. Solving these equations we find:

$$\delta = -a_M e_M\cos(\kappa_M(t - t_o))$$

$$\epsilon = e_M 2\frac{\Omega_M}{\kappa_M}\sin(\kappa_M(t-t_o))$$

$$\xi = a_M \sin(i_M)\sin(\mu_M t)$$

where we have written μ_M instead of μ (from Eqn. C.11) to specify that we speak of Mimas's vertical frequency where t_0 is chose such that $t = 0$ at the ascending node ($\xi = 0$), and κ_M is given to the fourth multipole moment by:

$$\kappa_M = \frac{GM_S}{r^3}[1 - \frac{3}{2}J_2(\frac{R_S}{r})^2 + \frac{45}{8}J_4(\frac{R_S}{r})^4]$$

where R_S is the radius of Saturn and M_S its mass. Now we can substitute ϵ and δ in Eqn. (C.14) and finally get:

$$g_{M_z} = a_M \sin(i_M)\sin(\mu_M t)[\frac{GM_M}{\Delta^{3/2}} - \frac{3GM_M a_M^2}{\Delta^{5/2}}(-\frac{r}{a_M}\cos(\Omega_M t-\theta)+1)e_M\cos(\kappa_M(t-t_o)) + \frac{r}{a_M}\sin(\Omega_M t-\theta)e_M 2\frac{\Omega_M}{\kappa_M}\sin(\kappa_M(t-t_o))] \tag{C.18}$$

The next step is to Fourier expand these Δ denominators on $\Omega_M t - \theta$ to find the overall frequency of the force which will depend on a linear sum of the vertical, horizontal and orbital frequencies. The forcing function will then be a sum of exponentials. This will cause a periodic perturbation in the disk that will launch a wave. The coefficients of this expansion have a special name: Laplace Coefficients b_i (Brouwer & Clemence, 1961). Specifically, the Laplace coefficients we need are the coefficients of the expansion:

$$\frac{a_M^3}{\Delta^{\frac{3}{2}}} = \frac{1}{2}b_{\frac{3}{2}}^{(0)} + \sum_{m=1}^{\infty} b_{\frac{3}{2}}^{(m)}\cos[m(\Omega_M t-\theta)] \tag{C.19}$$

$$\frac{a_M^5}{\Delta^{\frac{5}{2}}} = \frac{1}{2}b_{\frac{5}{2}}^{(0)} + \sum_{m=1}^{\infty} b_{\frac{5}{2}}^{(m)}\cos[m(\Omega_M t-\theta)]$$

and they are given by the integrals:

$$b_{\gamma}^{(m)}(\beta) \equiv \frac{2}{\pi}\int_0^{\pi} \Gamma^{-\gamma}\cos(m\psi)d\psi, \quad m = 0, 1, 2\,...$$

$$\beta \equiv \frac{r}{a_M}$$

$$\Gamma \equiv 1 + \beta^2 - 2\beta\cos\psi$$

The strongest vertical resonances in Saturn's rings still keep the vertical displacements ξ small, such that keeping the forcing term to first order in smallness has the equation

$$g_{M_z} = \frac{GM_M(\xi)}{\Delta^{3/2}} - \frac{3GM_M(\xi)}{\Delta^{5/2}} * [(-a_M r\cos(\Omega_M t - \theta) + a_M^2)\delta + a_M r\sin(\Omega_M t - \theta)\epsilon]$$

become

$$g_{M_z} = \frac{GM_M\xi}{\Delta^{3/2}} + \mathcal{O}(\xi * \epsilon) + \mathcal{O}(\xi * \theta) \approx \frac{GM_M\xi}{\Delta^{3/2}} = \frac{GM_M\sin(i_M)\sin(\mu_M t)}{a_M^2}\left(\frac{a_M^3}{\Delta^{\frac{3}{2}}}\right)$$

Substituting Eqn. (C.19) for Δ we get:

$$g_{M_z} = \frac{GM_M\sin(i_M)\sin(\mu_M t)}{a_M^2}(\frac{1}{2}b_{\frac{3}{2}}^{(0)} + \sum_{m=1}^{\infty} b_{\frac{3}{2}}^{(m)}\cos[m(\Omega_M t - \theta)]) \tag{C.20}$$

This means that the overall frequency for the strongest vertical force will come from an interaction of μ_M and $m\Omega_M$. Shortly we'll see that the forcing frequency ω will be given by $\omega = m\Omega_M \pm \mu_M$.

The vertical force of the moon describe by Eqn. (C.20) will have an infinite number of frequencies, but only one will resonate with the rings at a particular radius. In particular, resonance occurs when:

$$\omega - m\Omega(r_V) = \pm\mu(r_V) \tag{C.21}$$

$$m(\Omega_M - \Omega(r_V)) + \mu_M = \pm\mu(r_V)$$

where r_V is the radius at which the resonance occurs, and it is defined by Eqn. (C.21).

Eqn. (C.21) states that the condition for resonance is that the forcing frequency ω experienced in the frame of the particle (that's why there is a subtraction of $m\Omega(r_V)$ in the LHS, it represents a coordinate transformation into the frame of the particle), has to be equal to its vertical frequency $\mu(r_V)$ (the $\pm$ sign just signifies that the subtraction in the LHS can come out negative: this happens when the particle has an orbit inside the orbit of the moon). For every m we'll have a different radius that satisfies the above equation. Only at these resonances do these forces become significant for the dynamics of the rings (Murray & Dermott, 2000). Therefore, at any given resonant radius we only care about one of the terms of the sum in Eqn. (C.20): the one with the resonant frequency. Assuming a particular m, we can then write the result of above's sum.

$$gM_z = \frac{GM_S \sin(i_M)}{(1+\delta_{m0})a_M^2} b_{\frac{3}{2}}^{(m)} * \cos(m(\Omega_M t - \theta)) \sin(\mu_M t)$$

where δ_{m0} is the Kronecker delta.

To combine the frequencies we use:

$$\cos(\alpha)\sin(\beta) = \frac{1}{2}(\sin(\alpha+\beta) - \sin(\alpha-\beta)) = \mathrm{Re}[\frac{-i}{2} e^{i[m(\Omega_M t-\theta)+\mu_M t]} - e^{i[m(\Omega_M t-\theta)-\mu_M t]}]$$

To subsequently get:

$$g_{M_z} = \mathrm{Re}[(-i)\frac{GM_M \sin(i_M)}{(1+\delta_{m0})2a_M^2} b_{\frac{3}{2}}^{(m)} e^{i[m(\Omega_M t-\theta)+\mu_M t]} - e^{i[m(\Omega_M t-\theta)]-\mu_M t}]$$

This corresponds to two frequencies: $\omega = m\Omega_M \pm \mu_M$ which in turn corresponds to two different resonances (the inner vertical resonance and the outer vertical resonance; note that μ_M and $\mu(r_V)$ must have different signature otherwise the condition for resonance becomes $r_V = r_M$). In general, we can write:

$$g_{M_z} = \mathrm{Re}[\pm e^{-i\frac{\pi}{2}} \frac{GM_M \sin(i_M)}{(1+\delta_m 0)2a_M^2} b_{\frac{3}{2}}^{(m)} e^{i[m(\Omega_M-\theta)\pm\mu_M t]}] \tag{C.22}$$

and since to solve the equation of motion of the wave we will want to write g_{M_z} in the form:

$$g_{M_z} = \mathrm{Re}[f_M e^{i(\omega t - m\theta)}] \tag{C.23}$$

we compare Eqns. C.23 and C.22 and find that:

$$f_M = \pm e^{-i\frac{\pi}{2}} \frac{GM_M \sin(i_M)}{(1+\delta_m 0)2a_M^2} b_{\frac{3}{2}}^{(m)} \tag{C.24}$$

which adds a phase of $-\frac{\pi}{2}$ to the forcing frequency with respect to the orbital frequencies. Note that m is the azimuthal wavenumber since in Eqn. (C.12) we take the response in the rings to be in phase with the forcing frequency. Apart from indicating the number of times the forcing repeats azimuthally, m also indicates then the number of times the wave-pattern repeats azimuthally or, in other words, the number of of spiral arms. Also note that if we replace θ by $\Omega(r_V)t$ and define $\omega' = \omega - m\Omega(r_V)$, which is the forcing frequency as experienced in the frame of the particle, then Eqn. (C.21) (the condition for resonance) becomes: $\omega' = \pm\mu(r_V)$.

In the Mimas 5:3 Inner Vertical Resonance (IVR) we take the minus sign for $\mu(r_V)$, the plus sign for μ_M and $m = 4$. From this and Eqn. (C.21) we can get the position of the resonance which is $r_V = 131902\,\mathrm{km}$. We then have for the Mimas 5:3 bending wave.

$$g_{M_z} = \mathrm{Re}[e^{-i\frac{\pi}{2}} \frac{GM_M \sin(i_M)}{2a_M^2} b_{\frac{3}{2}}^{(4)} e^{i(\omega - m\theta)}] \tag{C.25}$$

where $b_{\frac{3}{2}}^{(4)} = 4.12042$.

C.2.3 g_{Rz}: Acceleration due to the Rings

We begin with the equation:

$$\boldsymbol{g}_R = G \int_0 dm' \frac{\boldsymbol{r}' - \boldsymbol{r}}{|\boldsymbol{r}' - \boldsymbol{r}|^3}$$

where we are integrating all the area covered by the surface mass density σ to get its influence on the point r, and where r and r' are both in the relative coordinate system based at the center of the central body. This integral was first studied by Hunter and Toomre (Toomre, 1964) in the context of instabilities on disks and

the below result regarding bent disks was derived, by other means, by Bertin and Mark (Bertin & Mark, 1980).

Note that, on differential form, this look like:

$$d\boldsymbol{g}_R = Gdm' \frac{\boldsymbol{r}' - \boldsymbol{r}}{|\boldsymbol{r}' - \boldsymbol{r}|^3}$$

where dm' is an the accelerated differential mass; this is just Newton's law of gravitation. To find the z-component of this acceleration, we write everything in cylindrical coordinates and take the dot product with the $\boldsymbol{k}$ vector.

$$dg_{R_z} = Gdm \frac{\boldsymbol{r}' - \boldsymbol{r}}{|\boldsymbol{r}' - \boldsymbol{r}|^3} \cdot \hat{\boldsymbol{k}} = \frac{G\sigma(r')r'dr'd\theta(z'-z)}{(r^2 + r'^2 - 2rr'\cos(\theta' - \theta) + (z'-z)^2)^{\frac{3}{2}}}$$

F

We saw in the last subsection that the vertical forcing due to Mimas occurs at a temporal frequency ω and angular wave-number m. Throughout the work we'll make the linearizing assumption that the response is at the same frequency. Therefore:

$$z = \mathrm{Re}[h(r)e^{i(\omega t - m\theta)}] \tag{C.26}$$

Substituting this into the equation and further linearizing on $(z' - z)$ (neglecting the $(z' - z)^2$ term) we get:

$$dg_{R_z} = \frac{G\sigma r'dr'd\theta'(\mathrm{Re}[h(r')e^{i(\omega t - m\theta')}] - \mathrm{Re}[h(r)e^{i(\omega t - m\theta))}])}{(r^2 + r'^2 - 2rr'\cos(\theta' - \theta))^{\frac{3}{2}}}$$

Now we attempt to write this in the form:

$$g_R(r) = \mathrm{Re}[f_R(r)e^{i(\omega t - m\theta)}] \tag{C.27}$$

$$g_{R_z} = \mathrm{Re}[\int_0^\infty \int_0^{2\pi} \frac{G\sigma r'dr'd\theta'(h(r')\cos(m(\theta' - \theta)) - h(r))}{(r^2 + r'^2 - 2rr'\cos(\theta' - \theta))^{\frac{3}{2}}} e^{i(\omega t - m\theta)}]$$

We now use the simplifying substitution: $\theta' - \theta = \psi$

$$g_{R_z} = \mathrm{Re}[\int_0^\infty \int_{-\pi}^{\pi} \frac{G\sigma r' dr' d\psi (h(r')\cos(m\psi) - h(r))}{(r^2 + r'^2 - 2rr'\cos(\psi))^{\frac{3}{2}}} e^{i(\omega t - m\theta)}] \tag{C.28}$$

And hence by comparing to Eqn. (C.27) we can deduce that:

$$f_R = \int_0^\infty \int_{-\pi}^{\pi} \frac{G\sigma r' dr' d\psi (h(r')\cos(m\psi) - h(r))}{(r^2 + r'^2 - 2rr'\cos(\psi))^{\frac{3}{2}}} \tag{C.29}$$

The first approximate solution to this integral came in 1980 by Bertin and Mark (Bertin & Mark, 1980); later, Frank Shu published another way to get to the result (Shu, 1984a). The approximations done in both papers are also going to be assumed to hold in our case, although there is some observational evidence that they may be braking down on the Mimas 5:3 bending wave (Sega Neuman et al., 2019). To set up the approximations used, I start by using the identity $\cos(m\psi) = 1 - \sin(m\frac{\psi}{2})$ to separate the two integrals.

$$f_R = \int_0^\infty \int_{-\pi}^{\pi} \frac{G\sigma(r') r' dr' d\psi (h(r') - h(r) - h(r)\sin(m\frac{\psi}{2})}{(r^2 + r'^2 - 2rr'\cos(\psi))^{\frac{3}{2}}}$$

$$f_R = \int_0^\infty \int_{-\pi}^{\pi} \frac{(h(r') - h(r))G\sigma(r')r'}{(r^2 + r'^2 - 2rr'\cos(\psi))^{\frac{3}{2}}} dr' d\psi - \int_0^\infty \int_{-\pi}^{\pi} \frac{\sin(m\frac{\psi}{2})h(r)G\sigma(r')r'}{(r^2 + r'^2 - 2rr'\cos(\psi))^{\frac{3}{2}}} dr' d\psi \tag{C.30}$$

$$f_R = \int_0^\infty G\sigma(r')r'dr'(K_0(h(r') - h(r)) - h(r)N_m)$$

where

$$K_0 = \int_{-\pi}^{\pi} \frac{d\psi}{(r^2 + r'^2 - 2rr'\cos(\psi))^{\frac{3}{2}}}$$

$$N_m = \int_{-\pi}^{\pi} \frac{d\psi \sin(m\frac{\psi}{2})}{(r^2 + r'^2 - 2rr'\cos(\psi))^{\frac{3}{2}}}$$

The first approximation is to argue that $h(r)$, in its wave nature, will vary quickly with r, with equal parts negative (incursion below the ring's plane) and positive (above the rings plane). The symmetric aspect of $h(r)$ along the z and r axes then makes the second integral in Eqn. (C.30) vanish. This brakes down close to resonance where the wavelength is long, and may be responsible for the inadequacy of the dispersion

relation seen in the first three cycles of the wave (Sega Neuman et al., 2019). Nevertheless this close-to-resonance correction will not be done here because it escapes the scope of this appendix, and hence we take N_m to vanish everywhere. To solve the K_m integral we consider that most of the self-gravitating effects are local (due to nearby ring particles), such that $r \approx r'$ and $\cos(\psi) \approx 1 - \frac{\psi^2}{2}$ and the effects of integrating from π to $-\pi$ can be achieved by integrating from δ to $-\delta$, where δ is a small angle such that the $\cos(\delta) \approx 1 - \frac{\delta^2}{2}$.

$$K_0 = \frac{1}{r'^3} \int_0^{\delta} \frac{2d\psi}{(\frac{(r-r')^2}{r'^2} + \frac{r}{r'}\psi^2)^{\frac{3}{2}}}$$

where we have used the fact that the integrand is symmetric. We can find this integral in tables. $\int \frac{dx}{(a+bx^2)^{\frac{3}{2}}} = \frac{x}{a\sqrt{a+bx}}$

$$K_0 = \frac{2}{(r'^3 \frac{(r-r')^2}{r'^2})} \frac{\delta}{\sqrt{\frac{(r-r')^2}{r'^2} + \frac{r}{r'}\delta^2}}$$

By taking $\frac{r'-r}{r'}$ to be small and $\frac{r}{r'} \approx 1$, $\frac{\delta}{\sqrt{\frac{(r-r')^2}{r'^2} + \frac{r}{r'}\delta^2}}$ approaches 1 and we get

$$K_0 = \frac{2}{r'(r-r')^2} \qquad r \approx r', \delta < 1 \tag{C.31}$$

Now we have to integrate K_0 with respect to the radial coordinate, but we know it diverges at $r = r'$ so the integral will diverge. Encountering this divergence is common when dealing with $\frac{1}{r^2}$ laws and we can side step it by using residue calculus and extending the integral into the complex plane, so to exclude the diverging point from the integral. First, since $r \approx r'$, we can write $h(r)/(r - r') \approx \frac{dh}{dr}$. Second replace the integrated variable with the complex variable z (not the vertical coordinate in this case). Moreover, we take σ to be constant or slowly varying so that we can pull it out of the integral. We also note that $h(r')$ and $\frac{dh}{dr}$ are not defined in the negative real axis as r' is a ray, hence we complement $h(r')$ to be zero when $r' < 0$ and trace the contour seen in figure C.2. Finally, we take $h(r')$ to take a WKBJ form, as it is a wave profile with slowly varying amplitude ($h(r) = A(r)e^{\int(ik)}$) and to ensure the integrand converges at infinity to 0, we close the integral either in the upper or lower half of the imaginary plane depending on the sign of k. The only contributing part of the contour is effectively the section in the real line from $r = 0$ to $r = \infty$, so we can write:

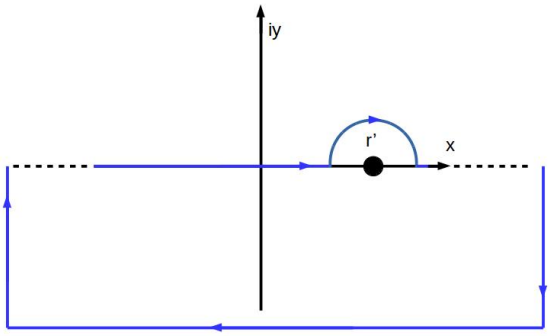

Figure C.2: The integral is taken about the drawn contour, where the semi-circle drawn to avoid the singular point has been exaggerated. In this case the integral is closed in the lower half of the complex plane such that the function $h(r) = A(r)\exp[i\int k(dx + idy)]$ converges to 0 at infinity and remains analytic there.

$$f_R = \int_0^\infty G\sigma(r')dr' K_0 = G\sigma(r) \oint \frac{\frac{dh}{dz}(z)}{z - r} dz$$

where the countour integral transverses the real line and $\pm$ complex infinity depending on the sign of k (see Figure C.2). Then, Cauchy Integral Formula states that for a point a inside a contour C:

$$2\pi i f(a) = \oint \frac{f(z)}{z - a} dz$$

So the integral becomes

$$f_R = i2\pi G\sigma(r) s \frac{dh}{dr} \tag{C.32}$$

where $s = \text{sign}(k)$ and it corresponds to closing the contour in the upper half in a counterclockwise path if k is positive or in the lower half in a clockwise path if k is negative.

C.2.4 List of assumptions made

- The only relevant frequency of the force exerted by Mimas is the one picked out by the particles in the resonant orbit (just the $b^{(4)}_{\frac{3}{2}}$ coefficients survives).
- The particles react to the forcing at the same frequency as the forcing function ($z = h(r)e^{i(\omega t - m\theta)}$)

- The WKBJ form for $h(r)$ ($h(r) = \mathrm{Re}[A(r)e^{i\int k dr}]$) is valid asymptotically (used in the complex integral of equation 31).

- To solve the integrals in K_m C.30 integral we only consider that most of the self-gravitating effects are local (due to nearby ring particles), such that $r \approx r'$ and $\cos(\psi) \approx 1 - \frac{\psi^2}{2}$.

- The second term in Eqn. (C.30) vanishes because $h(r)$ is equal parts positive and negative along r, and it varies much quickly than $N_m\sigma(r)$. Mathematically, this can be express by saying that if we divide the integral $\int_0^\infty N_m h(r')dr'$ into a piece-wise integral made by each of this recurring periods of the function $h(r)$.

$$\int_0^\infty N_m h(r')\sigma(r')dr' = \int_0^{\lambda_1} h(r')N_m\sigma(r')dr' + \int_0^{\lambda_2} h(r')N_m\sigma(r')dr'... \tag{C.33}$$

At each of these integrals, N_m and σ can be taken to be constant, and the integrals $\int_0^{\lambda_i} h(r')dr'$ vanishes. Hence the whole thing vanishes. This may not hold near resonance where $h(r)$ does not vary slowly within one wavelength since the wavelength is relatively big ($\sim 100\,\mathrm{km}$), and a failure in the dispersion relation close to resonance may indicate a change in surface density σ over the first cycles of the wave. N_m, on the other hand can be shown to in fact be slow varying there. We can solve the integral for N_m analytically by making similar approximations as the ones used for K_m to get Eqn. (C.31) (this way of solving the integrals is vaguely hinted at in Shu (1984b)). That is, take ψ to be small and $r \approx r'$.

$$N_m = \int_0^\delta \frac{d\psi 4\sin(m\frac{\psi}{2})}{(r^2 + r'^2 - 2rr'\cos(\psi))^{\frac{3}{2}}}$$

$$N_m = \int_0^\delta \frac{d\psi(m\psi)^2}{r^3(\frac{(r-r')^2}{r^2} - \frac{r'}{r}\psi^2)^{\frac{3}{2}}}$$

$$N_m = \frac{m^2}{r^3}\int_0^\delta \frac{\psi^2 d\psi}{(\frac{(r-r')^2}{r^2} - \psi^2)^{\frac{3}{2}}}$$

We can find a solution in a table of integrals or integrating software.

$$N_m = \frac{m^2}{r^3}[(\ln(\sqrt{\frac{(r-r')^2}{r^2}+\delta^2}) - \frac{\psi}{\sqrt{\frac{(r-r')^2}{r^2}+\delta^2}} - \ln(\sqrt{\frac{(r-r')^2}{r^2}+0}) + \frac{\psi}{\sqrt{\frac{(r-r')^2}{r^2}+0}}$$

We take $\frac{r-r'}{r^2} \approx 0$ and $\mathcal{O}(\delta^2) \approx 0$

$$N_m = -\frac{m^2}{r^3}\ln(\sqrt{\frac{r}{|r-r'|}})$$

While this diverges at resonance, the small value of $\frac{m^2}{r^3}$ and the slowly changing nature of the logarithm assures that this expression can be pulled out of the integrals above.

C.3 The Forced Bending Wave Equation

We return now to the equation of motion (Eqn. C.7) and substitute our expressions for the g's and z by using Eqns. (C.13), (C.23) and (C.27).

$$(\frac{d}{dt}+\Omega\frac{d}{d\theta})^2 z = g_{Sz}(r,\theta,z) + g_{Mz}(r,\theta,z,r_M,\theta_M,z_M) + g_{Rz}(r,\theta,z)$$

$$(\frac{d}{dt}+\Omega\frac{d}{d\theta})^2 \mathrm{Re}[h(r)e^{i(\omega t-m\theta)}] = \mathrm{Re}[-\mu h(r)e^{i(\omega t-m\theta)}]+\mathrm{Re}[f_M e^{i(\omega t-m\theta)}]+\mathrm{Re}[f_R(r)e^{i(\omega t-m\theta)}] \quad \text{(C.34)}$$

$$i^2(\omega-m\Omega)^2 h(r) = -\mu^2 h(r) + f_M + f_R(r)$$

where we have canceled out the $e^{i(\omega t-m\theta)}$ in both sides of the equation. Now we substitute in Eqns. (C.24) and (C.32):

$$-(\omega-m\Omega)^2 h(r) = -\mu^2 h(r) + e^{-i\frac{\pi}{2}}\frac{GM_M\sin(i_M)}{2a_M^2}b_{\frac{3}{2}}^{(4)} + i2\pi G\sigma(r)s\frac{dh}{dr} \quad \text{(C.35)}$$

The term $e^{-i\frac{\pi}{2}}\frac{GM_M\sin(i_M)}{2a_M^2}b_{\frac{3}{2}}^{(4)}$ is a constant and, in its place, I'll just leave it as f_M from now on. We further simplify Eqn. (C.35) by writing $D = -(\omega-m\Omega)^2+\mu^2$

$$-i2\pi G\sigma(r)s\frac{dh}{dr} + D(r)h(r) = f_M \tag{C.36}$$

This equation describes the wave-profile $h(r)$ of a bending wave given that the assumptions above hold. Note that the two terms in the LHS are acting as restoring force. In the wave propagating region $D < 0$, that is, the vertical frequency of the particle as experienced by an orbiting particle is less than the forcing frequency; this allows the particles to better propagate the gravitational perturbance of Mimas and form a wave (we'll see that if $D > 0$ the solution becomes exponentially decaying and the wave doesn't propagate).

Note that both terms act as restoring forces, but one depends on the slope of the wave, instead of just on the displacement from equilibrium. The restoring property of the gravitational acceleration terms is independent of whether we can cancel the exponentials in Eqn. (C.34) or not. That the vertical response of the particle ($\ddot{z}(t)$) is at the frequency of the forcing function is motivated by interpreting this restoring force as the cause of harmonic motion; the forcing and the response do not have to be in phase however, since the amplitude f and h can be complex and will bring phases with them.

Now we are going to non-dimensionalize this equation by making the change of variables $r = r_V(x+1)$. We note that:

$$\frac{dh}{dx} = \frac{dh}{dr}\frac{dr}{dx} = \frac{dh}{dr}r_V$$

.

Moreover, we linearize the factor $D(r)$ by expanding it about resonance r_V. Recall that $D = 0$ at resonance:

$$D \approx \cancelto{0}{D(r_V)} + r_V\frac{dD}{dr}|_{r_V}x = r_V\frac{dD}{dr}|_{r_V}x \tag{C.37}$$

so the equation of motion becomes:

$$-i2\pi G\sigma(r)s\frac{dh}{dx}\frac{1}{r_V} + \frac{dD(r)}{dr}|_{r_V}xr_Vh(x) = f_M(r_V)$$

I write $f_M(r_V)$ to remind the reader that the forcing was derived only at resonance. That is, only at resonance does all the Laplace coefficient vanish except for the $b_{\frac{3}{2}}^{(4)}$ term. This is the assumption that the forcing is only significant close to resonance and that it keeps it's value all throughout the wave propagating region.

We can simplify the above equation by writing

$$\mathcal{D} \equiv r_V \frac{dD}{dr}|_{r_V} \tag{C.38}$$

Then, we divide everything by $\mathcal{D}$ and further defining some simplifying constants (as done in Shu et al. (1983) and Shu (1984a)):

$$\varepsilon \equiv \frac{2\pi G\sigma(r_V)}{\mathcal{D}r_V} \tag{C.39}$$

$$L_V \equiv \frac{f_M(r_V)}{\mathcal{D}} \tag{C.40}$$

where $f_M(r_V)$, given in Eqn. (C.24), is the amplitude of Mimas forcing at the resonance radius r_V, and $\sigma(r_V)$ is the surface density of the ring at resonance. Substituting Eqns. (C.38), (C.39), and (C.40) into Eqn (C.35), and recalling that the Mimas 5:3 wave travels inwards $(s = -1)$, we finally get:

$$i\varepsilon\frac{dh}{dx} + xh = L_V \tag{C.41}$$

This is the most reduced version of the equation of motion for the bending wave. It is solvable by the method of integrating factors, by using the factor in question $I = e^{\int p(x)dx} = e^{\int \frac{x}{i\varepsilon}dx} = e^{\frac{x^2}{2i\varepsilon}}$ and integrating both sides of the equation, we get:

$$he^{\frac{x'^2}{2i\varepsilon}}\Big|_{\infty}^{x} = -\int_{\infty}^{x} \frac{iL_V}{\varepsilon} e^{\frac{x'^2}{i2\varepsilon}} dx'$$

$$h(x) - \cancelto{0}{h(\infty)} = -e^{\frac{ix^2}{2\varepsilon}} \int_{\infty}^{x} \frac{iL_V}{\varepsilon} e^{-\frac{ix'^2}{2\varepsilon}} dx' \tag{C.42}$$

where the lower bound of the integral is given by the boundary condition, which is that $h(x) \to 0$ as $x \to \infty$

This requirement comes from the fact that, away from resonance, $f_M = 0$, which yields the equation:

$$i2\pi G\sigma s\frac{dh}{dr} = [(\omega - m\Omega)^2 - \mu^2]h(r)$$

Sufficiently away from resonance we can safely take $h(r)$ as slowly varying in amplitude and wavelength, and hence it takes its WKBJ form: $h \approx \mathrm{Re}[A(r)e^{i\int kdr}] \approx \mathrm{Re}[Ae^{i\int kdr}]$ and hence:

$$\frac{dh}{dr} = ikh(r)$$

for positive k. Or we can write

$$\frac{dh}{dr} = is|k|h(r)\,; \qquad s = \mathrm{sign}(k)$$

for any k.

So we get for the free bending wave equation:

$$(\omega - m\Omega)^2 = \mu^2 + 2\pi G\sigma|k| \tag{C.43}$$

or

$$-D = 2\pi G\sigma|k|$$

At $r \to \infty$, D will be positive, so the LHS will be negative. In fact, in the case of an inner vertical resonance, like the Mimas 5:3, D is positive radially away from resonance for a free wave. This is because the vertical frequency of a particle becomes greater than the forcing frequency as experienced by the particle in its frame. If one is sufficiently away from resonance such that Eqn. (C.43) holds, and $D < 0$, then k is complex. If we don't impose that $h(x) = 0$ as $x \to \infty$ then it would diverge. Finally, it is customary to write Eqn. (C.42) in terms of the variable $\xi = \frac{-s_\varepsilon x}{\sqrt{2|\varepsilon|}}$ with $s_\varepsilon \equiv \mathrm{sign}(\varepsilon) = 1$ for the Mimas 5:3 bending wave.

$$h(x) = \frac{iL_V}{\sqrt{\frac{|\varepsilon|}{2\pi}}} e^{i\xi(x)^2} \frac{1}{\sqrt{\pi}} \int_{-\infty}^{\xi(x)} e^{-i\xi'^2} d\xi' \tag{C.44}$$

(note that the change of variables brings out a factor of $-\sqrt{2|\varepsilon|}$ from the differential which cancels the minus sign present in the RHS of Eqn. (C.42)). From this expression we can extract the physical amplitude, which is:

$$A_V = \frac{iL_V}{\sqrt{\frac{|\varepsilon|}{2\pi}}}$$

which for the Mimas 5:3 and a surface density $\sigma = 363 \frac{\mathrm{Kg}}{\mathrm{m}^2}$ we get $A_V = 783.4\,\mathrm{m}$ or in terms of the surface mass density:

$$A_V = \frac{14926 \frac{\mathrm{Kg}^{\frac{1}{2}}}{\mathrm{m}}}{\sqrt{\sigma}}$$

The integral in Eqn. C.44 is called a Fresnel integral and can only be solved numerically. In practice, this is usually done via the Fresnel Sin ($S(u)$) and Cosine ($C(u)$) functions and the identity:

$$\sqrt{\frac{\pi}{2}} C\left(\sqrt{\frac{2}{\pi}} u\right) + i\sqrt{\frac{\pi}{2}} S\left(\sqrt{\frac{2}{\pi}} u\right) \equiv \int_0^u e^{i\eta^2} d\eta$$

where

$$C\left(\sqrt{\frac{2}{\pi}} u\right) = \sqrt{\frac{2}{\pi}} \int_0^u \cos\eta^2 d\eta$$
$$S\left(\sqrt{\frac{2}{\pi}} u\right) = \sqrt{\frac{2}{\pi}} \int_0^u \sin\eta^2 d\eta$$

we hence write Eqn. C.44 as:

$$h(\xi) = \frac{A_V}{\sqrt{\pi}} e^{i\xi^2} \left(\int_{-\infty}^{0} e^{-i\xi'^2} d\xi' + \int_0^{\xi} e^{-i\xi'^2} d\xi' \right)$$

$$h(\xi) = \frac{A_V}{\sqrt{2}} e^{i\xi^2} \left[\left(\frac{1}{2} - \frac{i}{2} \right) + C\left(\sqrt{\frac{2}{\pi}} \xi\right) - iS\left(\sqrt{\frac{2}{\pi}} \xi\right) \right] \tag{C.45}$$

Now that we have derived the wave profile for the bending wave, the only thing left to be done is to consider one last interaction between the affecting ring particles: viscosity.

C.3.1 List of Assumptions Made

- Centrifugal equilibrium of a particle in the ring plane. Namely, that the azimuthal mean motion frequency arou s given by $\Omega = \sqrt{-\frac{1}{\varkappa}\left.\frac{\partial \Phi_S}{\partial \varkappa}\right|_{\alpha=0}}$ (if this weren't true we would observe significant radial displacement of the rings so the assumption is well warranted)

- The forcing f_M is only significant close to resonance and that it keeps the same value throughout the wave propagating region.

- Eqn. (C.38) is valid for the wave propagating region. That is, D varies slowly in the wave-propagating region where $r_V x = (r - r_V)$ is also small. is like an index as refraction, which will control the wavelength of the wave as it propagates. This goes back to assuming that the wavelength varies relatively slowly, or rather, that D varies slowly in one wavelength in the wave propagating region. Numerically, D is made of frequencies which go as $\frac{1}{r^3}$ and this fraction becomes smaller with higher order derivatives. Since $r - r_V$ is about 200 km at most, and $r \sim 10^5$ km, this is a good approximation close to resonance. Far from resonance the wave is damped, and hence no issues arise. Note that If D is slow-varying over the extent of one wavelength, then taking the WKBJ form for $h(r)$ may also be justified there.

C.4 Viscosity

C.4.1 Shear Viscosity

The last interaction to be included in Eqn. (C.7) pertains to the contact forces of adjacent particles within the ring. Through collisions, angular momentum is transferred from the wave to individual particles. This occurs due to the shear in the vertical velocities along the radial direction. Fluid mechanics yields, for the force due to this shear:

$$g_\nu = \nu \frac{\partial^2 \dot{z}}{\partial r^2}$$

Adding this to the equation of motion:

$$(\frac{d}{dt} + \Omega \frac{d}{d\theta})^2 z = +g_{S_z}(r,\theta,z) + g_{M_z}(r,\theta,z,r_M,\theta_M,z_M) + g_{R_z}(r,\theta,z) + \nu \frac{\partial^2 \dot{z}}{\partial r^2}$$

We now note that $\nu \frac{\partial^2 \dot{z}}{\partial r^2} = \nu = i\omega' \frac{d^2 h(r)}{dr^2} e^{i(\omega' t - m\theta)}$

We use this to get the new from of Eqn. (C.36).

$$-i2\pi G\sigma(r) s \frac{dh}{dr} + D(r)h(r) = f_M + i\nu\omega' \frac{d^2 h(r)}{d^2 r}$$

Similarly to Shu (1984a), I assume that the WKBJ form holds even close to resonance, but not necessarily at resonance. For this we consider the bending wave to be force-free, and hence f_M only exists near resonance. This is controversial and we do it heuristically, but the slow varying D, and the nature of resonant forcings (which are very important at resonance and quickly become irrelevant for the dynamics as one moves away), suggest this might work. Moreover, to further simplify we write $\omega' = (\omega - m\Omega)$. With this, we have modification to the free wave dispersion relation (Eqn. C.43):

$$D + 2\pi G\sigma s k = -i\nu\omega' k^2 \tag{C.46}$$

Damping is associated with an imaginary part of the wave-number. To solve for this imaginary part we write:

$$k = k_r + ik_i \longrightarrow k^2 = (k_r + ik_Z)^2 = k_r^2 + i2k_r k_i - k_i^2$$

and Eqn. (C.46) becomes:

$$D + 2\pi G\sigma s k_r + i2\pi G\sigma k_i = i\nu\omega' k_r^2 (1 + 2i\frac{k_i}{k_r} - \frac{k_i^2}{k_r^2}) \tag{C.47}$$

Now, if k_i where comparable to k_r, we would have some propagation in the evanescence region (away from Saturn), which we don't observe (Gresh et al., 1986), so $k_i << k_r$. We further assume that ν is small

such that the wave in underdamped (it completes many cycles before dying), which we also observe (Gresh et al., 1986). The wave being underdamped also shows that $k_i << k_r$: the wavelength is much shorter than the damping length. This implies that $\nu\cancelto{0}{\frac{k_i}{k_r}}$ and $\cancelto{0}{\frac{k_i^2}{k_r^2}}$), then we have:

$$D + 2\pi G\sigma s k_r + i2\pi G\sigma k_i = i\nu(\omega - m\Omega)k_r^2 \tag{C.48}$$

Now we group the imaginary and real parts of this equation. First, the real part:

$$D + 2\pi G\sigma s k_r = 0$$

$$k_r = \frac{D}{2\pi G\sigma} \tag{C.49}$$

Inner vertical resonances like the Mimas 5:3 create waves that travel inward, and hence $s = -1$. Plugging this in into the equation obtained from grouping the imaginary terms of Eqn. (C.48):

$$2\pi G\sigma k_i = -\nu(\omega - m\Omega)(\frac{D}{2\pi G\sigma})^2$$

So we finally get for k_i:

$$k_i = -\frac{\nu(\omega - m\Omega)D^2}{(2\pi G\sigma^2)^3} \tag{C.50}$$

How does this result in a damping factor? Recall that we assume the WKBJ form:

$$h(r) = A(r)e^{i\int k_r dr + \int \nu \frac{\omega' D^2}{(2\pi G\sigma)^3} dr}$$

Now we concentrate on the integral:

$$\int \nu \frac{\omega' D^2}{(2\pi G\sigma)^3} dr = \nu \frac{1}{(2\pi G\sigma)^3} \int_{r_V}^{r} \omega' D^2 dr \tag{C.51}$$

where we assume that σ^3 does not vary significantly with r compared to D^2 so that we can pull $\frac{1}{\sigma^3}$ out of the integral. We expand the integrand in a Taylor series about resonance and linearize up to the first non-vanishing term (recall that $\omega'|_{r_V} = (\omega - m\Omega)|_{r_V} = -\mu$ and $D(r_V) = 0$):

$$(-\mu+r_V\frac{\partial}{\partial r}x)(\cancelto{0}{D^2|_{r_V}}+2(\cancelto{0}{\frac{\partial D}{\partial r}D})|_{r_V}(r_V x)+(\cancelto{0}{D\frac{\partial^2 D}{\partial r^2}})|_{r_V}(r_V x)^2+(\frac{\partial D}{\partial r})^2|_{r_V}(xr_V)^2) \approx -\mu(\frac{\partial D}{\partial r})^2|_{r_V}(r_V x)^2$$

After doing the change of variables $x = \frac{r-r_V}{r_V}$; $dr = dxr_V$, and recalling Eqn. (C.38), the integral becomes:

$$-\mu r_V \mathcal{D}^2 \int_0^x x'^2 dx' = -\frac{\mu r_V \mathcal{D}^2}{3}x^3$$

Then, the exponential decaying factor becomes:

$$\exp \int \nu \frac{\omega' D^2}{(2\pi G\sigma)^3} dr = \exp -(\frac{r_V \mathcal{D}^2 \mu\nu}{(2\pi G\sigma)^3 3}x^3) \tag{C.52}$$

This is the damping due to the vertical shear in the radial direction, which has a functional dependency of $e^{-(\frac{x}{x_{\text{vis}}})^3}$, where $x_{\text{vis}} = \sqrt[3]{\frac{(2\pi G\sigma)^3 3}{\mathcal{D}^2 r_V \mu\nu}}$ is the dimensionless damping length. This multiplies Eqn. (C.44) to yield the final expression for the wave profile:

$$h(x) = \frac{iL_V}{\sqrt{\frac{|\varepsilon|}{2\pi}}} \exp -(\frac{r_V \mathcal{D}^2 \mu\nu}{(2\pi G\sigma)^3 3}x^3) e^{i(\frac{-x}{\sqrt{2\varepsilon}})^2} \frac{2}{\sqrt{\pi}} \int_{-\infty}^{\frac{-x}{\sqrt{2\varepsilon}}} e^{-i\xi'^2} d\xi' \tag{C.53}$$

where L_V is defined in Eqn. (C.40), $\mathcal{D}$ is Eqn. (C.38), ε in Eqn. (C.39), r_V is the resonant radius, σ the surface density, μ the vertical frequency at resonance, ν the kinematic viscosity of the rings, x is the radial coordinate centered at resonance normalize by the resonant radius ($x = \frac{r-r_V}{r_V}$), and G the gravitational constant. Multiplying by the propagator $e^{i(\omega' t - m\theta)}$ we get the final liner theory expression for the vertical position, z, of a ring particle as a function of time (t), its azimuthal position (θ) and distance from resonance (x).

$$z(t,\theta,x) = \frac{iL_V}{\sqrt{\frac{|\varepsilon|}{2\pi}}} \exp -(\frac{r_V \mathcal{D}^2 \mu\nu}{(2\pi G\sigma)^3 3}x^3) e^{i(\frac{-x}{\sqrt{2\varepsilon}})^2} e^{i(\omega' t - m\theta)} \frac{2}{\sqrt{\pi}} \int_{-\infty}^{\frac{-x}{\sqrt{2\varepsilon}}} e^{-i\xi'^2} d\xi' \tag{C.54}$$

C.4.2 List of Assumptions Made

- The kinematic viscosity of fluid mechanics (which assumes a smooth ring) is adequate to represent the effects of collisions in the bending wave.
- The WKBJ form of the wave profile holds everywhere in the wave propagating region, including near resonance.
- σ^3 does not vary significantly with r compared to D^2
- The wave in underdamped; the wavelength is significantly shorter than the damping length ($k_i << k_r$).

Appendix D

Self-gravity Wakes as Rigid Bodies and the Equilibrium Pitch-angle

D.1 The Tidal and Keplerian Torques

We begin by assuming the wakes to be rigid and computing the different torques that may change their orientation over time. Self-gravity wakes (SGW) are influenced by a tidal torque due to Saturn—which occurs due to the changes of Saturn's gravitational field along the length of the wake— and the torque due to the Keplerian shear. The tidal torque tends to align the long-axis of satellited towards the radial, pointing at the central body. The Keplerian shear torque occurs due to the collisions of particles with SGW. This is a necessary consequence of assuming the wakes to be rigid. Since all particles in the wake orbit at the frequency of the wake's center of mass (CM), then the particle radially in, and radially out will have a relative speed with respect to the rest of the flow: the radially in particles orbiting faster, and the others slower. Hence, the Keplerian shear torque attempts to point the wake in the azimuthal direction. Both torques will depend on the orientation of the wake θ (the angle between the long axis of the wake and the azimuthal), and hence at θ_{eq} the magnitude of both torques will equilibrate.

We first derive the tidal torque coming from the tidal force on a satellite (Murray & Dermott, 2000):

$$F_{\rm tidal} = 3\frac{GM_S}{a^3}y' * \sin\theta\cos\theta\rho_{\rm Roche}HW\,dy'$$

where a is the distance from Saturn's center, G the gravitational constant, M_S the mass of Saturn, ρ_w is the bulk density of the wake, θ the angle of the long-axis of the SGW with the azimuthal, L is the major-axis of the wake, H is the vertical axis and W the minor-axis. The integration variable y' is the distance along the long-axis taken from the center of mass of the wake. The torque due to self-gravity wakes then becomes:

$$\tau_{\text{tidal}} = 2\frac{GM_S}{a^3}\sin\theta\cos\theta\left(\frac{L}{2}\right)^3 * \rho_w HW \tag{D.1}$$

The Keplerian shear torque requires a more lengthy derivation. The torque arises from the momentum transfer that the disk particles exert on the wakes; to compute the trajectories and impact velocities of these particles however, we have to solve the restricted three-body problem. We use Hill's approximation of the two-body problem (Hill, 1878), in which the secondary body, the self-gravity wake, is significantly more massive than the third body, the incoming ring particle. The incoming velocity given by the Hill equations will govern the momentum transfer into the wakes. We will discuss numerical integration of the Hill equations in detail later, however, since our goal in this chapter is an analytical model for θ_{eq}, we will only use this method as a point of comparison for our approximations.

In order to derive an analytical solution of θ_{eq} that allows us to better understand the system, we resort to a two-body approximation of the three-body problem, leaving the numerical integration of Hill equations as a point of comparison. Specifically, we use a gravitational focusing approximation common in planet formation (Greenberg et al., 1991; Rafikov, 2004; Armitage, 2020), where the incoming speed of the scattering event can be either the dispersion velocity or the Keplerian differential velocity depending on which one dominates in the wave region. Cuzzi et al. (1979) already argued that the dispersion velocity dominates over the extent of a particle. However, we find that both velocities are similar over the extent of the Hill radius of a wake so the safest approach is to include 3-body corrections in our two-body approximation. From Greenberg et al. (1991) and Armitage (2020) we can get an approximate collision rate for this regime:

$$\frac{dM}{dt}(b) = q\Omega * b * \sigma * f * db \tag{D.2}$$

Where f is the fraction of particles that enter the Hill sphere that collide, q is the shear rate $q = -\frac{d\ln\Omega}{dr}$, Ω is the Keplerian frequency of the particle, b is the impact parameter and σ is the surface mass density of the disk. To get a torque we use two-body dynamics to find the speed and angle of incidence for the incoming particles at the moment of impact. In the hyperbolic scattering case, the specific angular momentum j can be written in terms of the impact parameter b.

$$j = q\Omega b^2 \tag{D.3}$$

and the energy we take the energy to be all kinetic energy as the scattered particle approaches from infinity:

$$E = \frac{1}{2}v^2 = \frac{1}{2}q^2\Omega^2 b^2 \tag{D.4}$$

Where v is the incoming speed at infinity. Using Eqn. D.2 the momentum transfer to the wakes as the particles with it is:

$$\frac{dp}{dt} = \frac{dM}{dt} * v_\theta \tag{D.5}$$

where v_θ is the speed at the moment of collision with the wake. Considering that r_{2B} is the position of the particle from the center of mass of the wake, we can write from Eqn. D.5 a torque:

$$\tau_{\mathrm{Kep};z'} = 2(1+\epsilon)\int_{b_{\min}}^{b_{\max}} \frac{dM}{dt} v_\theta(b,\theta) r_{2B}(b,\theta) \tag{D.6}$$

where $v_\theta(b) = b^2 * q\Omega / r_{2B}$ and

$$r_{2B}(b,\theta) = \frac{\frac{(b^2 q\Omega)^2}{G\rho_{\mathrm{Roche}} WLH}}{1 + e\cos(\theta - \varpi)}$$

is the two-body orbit Eqn. were the true anomaly has been set at the angular position of the long-axis of the wake where the collision takes place, and where ϖ is the argument of periapsis taken from the azimuthal direction. Here we are taking the angular momentum to be conserved about the CM of the wake, so that for a given impact parameter b we can determine a collisional speed v_θ at a distance r_{2B} from the CM. Under this approximation the trajectories of the particles are simple hyperbolas and the three-body effects are accounted for by using Hill's equations to determine the limit of the integral $b_{\min}$. This and the length of the long axis L relative to the Hill radius, which guarantees that particles entering the Hill sphere collide with the wake, allow us to do the following simplification of the Greenberg et al. (1991) formulation (Eqn. D.2):

- f, the fraction of particles that collide after entering the Hill Sphere is 1.
- We define $b_{\max}$ as the solution of $r_{2B}(b_{\max}, \theta) = \frac{L}{2}$
- The surface density σ is taken to by ρH

The collisional torque becomes:

$$\tau_{\text{Kep}} = -2(1+\epsilon)\int_{b_{\min}}^{b_{\max}} |v_\theta + \omega_z r_{2B}|\,(v_\theta + \omega_z r_{2B}) r_{2B}\rho H db \tag{D.7}$$

Where we have replaced the incoming speed in Eqn. (D.2) ($q\Omega b$) with $|v_\theta|$, have used ρH for σ, and, by adding $\omega_{z'} r_{2B}$, have included the fact that the rotation of the wake will contribute to the incoming speed of the particles.

For the case of equilibrium between the torques there is no rotation and hence $\omega_z = 0$, and since $v_\theta > 0$ we can write $|v_\theta| v_{theta} = v_\theta^2$. Introducing $\mu = G\rho_{\text{Roche}} HLW$ we are left with the integral:

$$2(1+\epsilon)\rho H \int_{b_{\min}}^{b_{\max}} v_\theta^2 r_{2B} db = 2(1+\epsilon)\rho H \mu \int_{b_{\min}}^{b_{\max}} (1 + \sqrt{\frac{b^6 q^4 \Omega^4}{\mu^2} + 1} * \cos(\theta - \varpi) db \tag{D.8}$$

Where we have used

$$e = \sqrt{2E\frac{j^2}{\mu^2}} = \sqrt{\frac{b^6 q^4 \Omega^4}{\mu^2} + 1}$$

for the eccentricity. The next steps in this approximation requires relations unique to hyperbolic orbits which we will derive briefly in the next subsection before continuing.

D.1.1 Hyperbolic orbit

Hyperbolic orbits have eccentricities greater than one, and if they are $>> 1$, they allow for certain simplifications of above expression in Eqn D.8. In odder to ensure the robustness of this approximation we must see if all colliding trajectories have a high eccentricity. In general the shorter the b, the shorter the eccentricity, the shortest b being $b_{\min}$ which limited by the fact that particles with too small b partake is horseshoe and tadpole orbits. The Hill radius R_{Hill} gives us a length we can used to estimate $b_{\min}$. Numerical simulation and analytical estimates (Greenberg et al., 1991; Murray & Dermott, 2000) place $b_{\min}$ at:

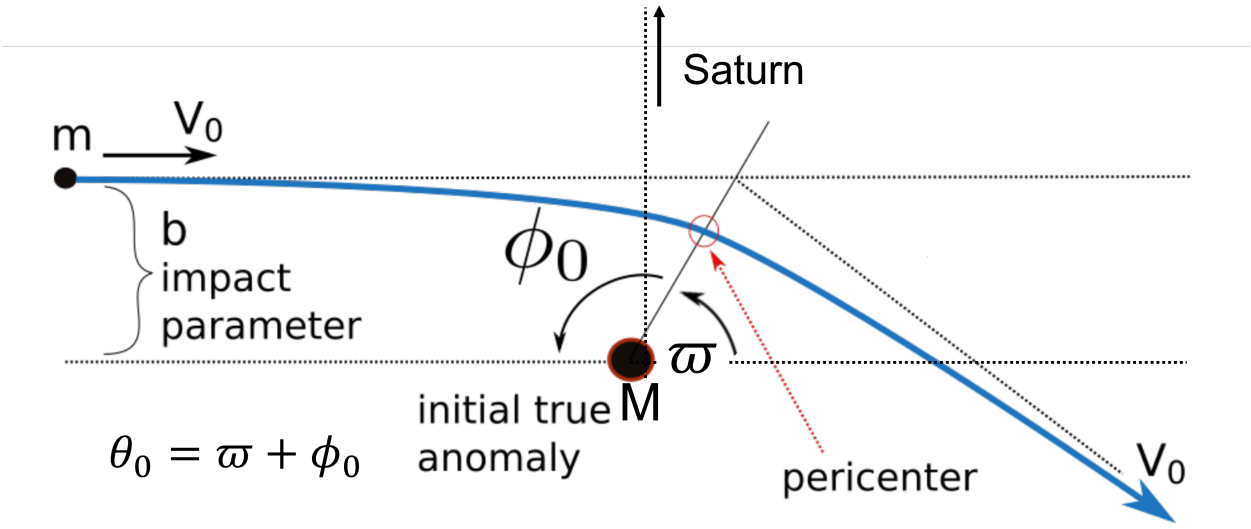

Figure D.1: Schema of an hyperbolic orbit with all the relevant angles denoted.

$b_{\min} \approx 1.75 R_{\text{Hill}} = 1.75\sqrt{\frac{\rho LWH}{3M_S}}a \sim 41\,\text{m}$

Where $a = 128000\,\text{km}$ which corresponds to the middle of the A-ring. Using a value for the Keplerian frequency $\Omega \sim 10^{-4}\,\text{s}^{-1}$, also corresponding to the middle of the A-ring, and a Keplerian shear rate $q = 1.5$, we get:

$$e_{\min} \sim \sqrt{15+1} \sim \sqrt{15}$$

Which is equivalent to the approximation:

$$e \approx \frac{b^3 q^2 \Omega^2}{\mu} \tag{D.9}$$

Now we use figure D.1 to derive an expression for the argument of pericenter for the encounter, $\varpi(b)$. We know that $\theta = \pi$ as $r \to \infty$ and hence

$$1 + e\cos\pi - \varpi = 1 - e\cos\varpi = 0 \tag{D.10}$$

Therefore,

$$\cos\varpi = \frac{1}{e} \approx \frac{\mu}{b^3 q^2 \Omega^2} \tag{D.11}$$

Conversely,

$$\sin\varpi = \frac{\sqrt{e^2-1}}{e} = \sqrt{1-\frac{\mu}{b^6 q^4 \Omega^4}} \approx 1 - \frac{1}{2}\frac{\mu}{b^6 q^4 \Omega^4} \sim 1 - \frac{1}{26} \sim 1$$

We can rewrite the $\cos(\theta - \varpi)$ as:

$$\cos(\theta-\varpi) = \cos\theta\cos\varpi + \sin\theta\sin\varpi \approx \cos\theta\frac{\mu}{b^3 q^2\Omega^2} + \sin\theta \tag{D.12}$$

D.1.2 Balancing the torques

Now we can simplify the integral in Eqn. D.8 as:

$$\tau_{\rm Kep} = 2(1+\epsilon)\rho H\mu \int_{b_{\rm min}}^{b_{\rm max}} (1+\cos\theta + \frac{b^3 q^2\Omega^2}{\mu}\sin\theta) db \tag{D.13}$$

$$\tau_{\rm Kep} = 2(1+\epsilon)\rho H\mu[(1+\cos\theta)(b_{\rm max}-b_{\rm min}) + \frac{q^2\Omega^2}{4\mu}\sin\theta(b_{\rm max}^4 - b_{\rm min}^4)) \tag{D.14}$$

Balancing both torques at the equilibrium angle θ_{eq} we get:

$$2\frac{GM_S}{a^3}\sin\theta_{eq}\cos\theta_{eq}\left(\frac{L}{2}\right)^3 * \rho_w HW = 2(1+\epsilon)\rho H\mu[(1+\cos\theta_{eq})(b_{\rm max}-b_{\rm min}) + \frac{q^2\Omega^2}{4\mu}\sin\theta_{eq}(b_{\rm max}^4 - b_{\rm min}^4)) \tag{D.15}$$

where $b_{\rm min} \approx 1.75 R_{\rm Hill}$. Note the strong dependece on b for the leading term.

To find $b_{\rm max}$ we solve the equation $r(b_{\rm max}, \theta_{eq}) = \frac{L}{2}$. Namely:

$$\frac{L}{2} * (1+\cos\theta_{eq}) + \frac{b_{\rm max}^3 q^2\Omega^2}{\mu}\sin\theta_{eq}) = \frac{b_{\rm max}^4 q^2\Omega^2}{\mu} \tag{D.16}$$

For $\theta_{eq} > 40^\circ$ (the wake's long-axis pointing more towards the radial direction) one can approximate the solution to be $b_{\rm max} = \frac{L}{2} * \sin\theta_{eq}$. Compared to using the exact value for $b_{\rm max}$, at $\theta_{eq} = 40^\circ$ this approximation understimates the Keplerian torque by 20%, and effects an overestimation on the pitch angle by

13%; for bigger angles, the approximations improves. For smaller angles we default to the exact expression for $b_{\max}$ which we write by defining the functions:

$$A = \frac{\left(27L^2q^4\mu\Omega^4(L + L\cos(\theta_{eq}))\,\mathrm{Sin}(\theta_{eq})^2 + \sqrt{55296q^6\mu^3\Omega^6(L + L\cos(\theta_{eq}))^3 + 729L^4q^8\mu^2\Omega^8(L + L\cos(\theta_{eq}))^2\,\mathrm{Sin}(\theta_{eq})^4}\right)^{1/3}}{6 \times 2^{1/3}q^2\Omega^2} \tag{D.17}$$

$$B = \frac{4 \times 2^{1/3}\mu(L + L\cos(\theta_{eq}))}{\left(27L^2q^4\mu\Omega^4(L + L\cos(\theta_{eq}))\,\mathrm{Sin}(\theta_{eq})^2 + \sqrt{55296q^6\mu^3\Omega^6(L + L\cos(\theta_{eq}))^3 + 729L^4q^8\mu^2\Omega^8(L + L\cos(\theta_{eq}))^2\,\mathrm{Sin}(\theta_{eq})^4}\right)^{1/3}} \tag{D.18}$$

$$C = \frac{1}{4}L\sin\theta_{eq} \tag{D.19}$$

So that the solution can be written as:

$$b_{\max} = \frac{1}{2}C + \frac{1}{2}\sqrt{C^2 + B - A} + \frac{1}{2}\sqrt{2C^2 + A - B + \frac{2C^3}{\sqrt{C^2 + B - A}}} \tag{D.20}$$

Substituting this expression is Eqn. D.15 yields a transcendental equation for the angle θ_{eq} which is hard to interpret given the cumbersome nature of $b_{\max}$.

If we instead consider $\theta_{eq} > 40°$, $b_{\max} = \frac{L}{2} * \sin\theta_{eq}$ and we get a simpler equation for the balance:

$$\begin{aligned} 2(1+\epsilon)\rho\mu[(1+\cos\theta_{eq})(\frac{L}{2} * \sin\theta_{eq} - 1.75R_{\mathrm{Hill}}) + \frac{q^2\Omega^2}{4\mu}\sin\theta_{eq}(\frac{L}{2} * \sin\theta_{eq} - (1.75R_{\mathrm{Hill}})^4)] \\ = 2\frac{GM_S}{a^3}\sin\theta_{eq}\cos\theta_{eq}\left(\frac{L}{2}\right)^3 * \rho_w W \end{aligned} \tag{D.21}$$

This expression represents an equation for the pitch-angle θ_{eq} as determined by equilibrating the tidal torque (left-hand side) with the Keplerian shear torque (right-hand side). The equilibrium angle parameterized by the density of the rings ρ_s and the wakes ρ_w, the dimensions of the wake, (H, W, L), the semi-major axis a, the coefficient of restitution ϵ, the total mass of the wake times G, μ, and the mass of Saturn M_s.

D.2 Comparison with n-body shear-box simulations

Besides θ_{eq}, there are three variables in this equation that don't have a set value: the coefficient of restitution (ϵ), the space density of the particles colliding with the wake (ρ) and the shear rate (q). The contributions of ϵ and ρ to the Keplerian torque are degenerate: increasing both will increase the torque, and choosing a low ϵ can be counter-weighted by choosing a higher ρ and vice-versa, although ϵ only goes from 0 to 1 and has a small effect on the torque given that it appears in the factor $(1+\epsilon)$.

D.2.1 The shear rate

We compare our model to the shear-box n-body simulations that have been performed at three different shear-rates, $q = (0, 1, 1.5)$. The value for ϵ will be set to 0.5 and ρ will be set to best fit the pitch-angles given by the n-body simulation. In Figure D.2 we compare three models: 1) where we assume that $e > 10$ and $\theta_{eq} > 40°$, hence $b_{\max} = \frac{L}{2}\sin\theta_{eq}$ (green dashed line), 2) where we use the full expression for $b_{\max}$ but still assume the incoming orbits to be highly hyperbolic (purple dashed line), and 3) where no assumptions about the trajectories of the incoming particles are made, and the Hill equations were numerically integrated for the systems (black dashed line). These three models are plotted in Figure D.2.

Figure D.2 shows that the hyperbolic approximation overestimates the Keplerian shear at low equilibrium angles, and the $b_{\max} = \sin\theta_{eq}L/2$ approximation underestimates them further. This is to be expected because, as mentioned above, the hyperbolic approximation is less accurate at small equilibrium angles. Moreover, this approximation also breaks down at lower shear rate since the incoming particles are closer to parabolic orbits. By taking the orbits to be hyperbolic we are overestimating the Keplerian shear torque and hence decreasing the predicted pitch-angle. The $b_{\max} = \sin\theta_{eq}L/2$ approximation manages to make a better estimate in this regime because including the shorter $b_{\max}$underestimates the Keplerian torque by a similar amount and goes opposite to the error introduced my assuming the orbits to be highly hyperbolic ($e > 10$).

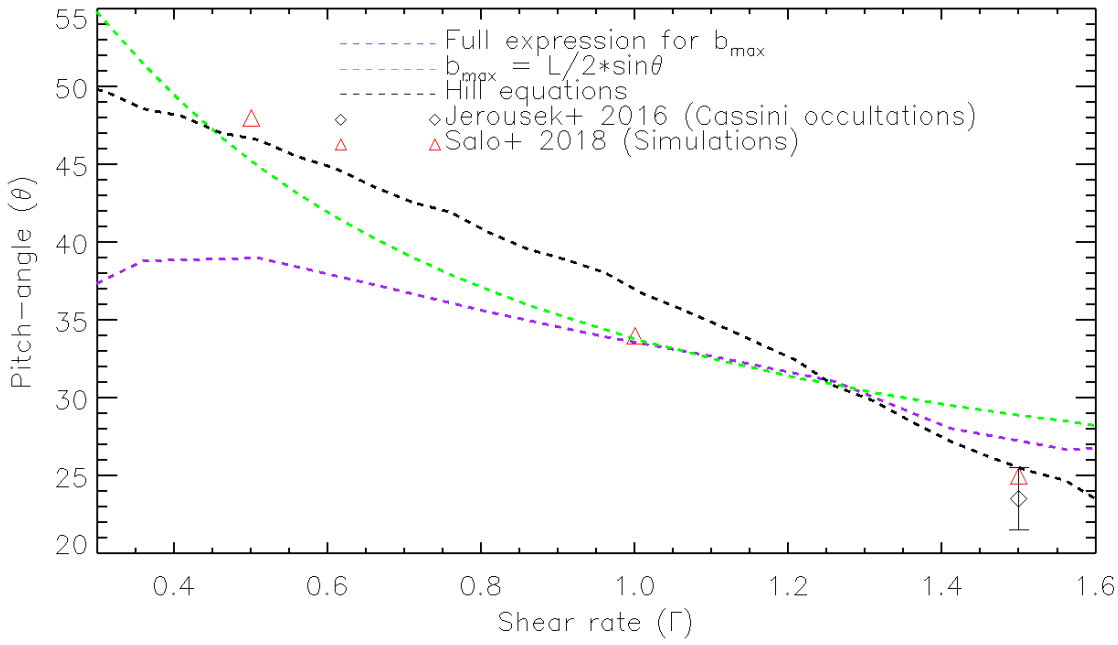

Figure D.2: Shear rate vs equilibrium pitch-angle for the rigid wake model for three levels of simplification.